University of Arkansas, Fayetteville

ScholarWorks@UARK

Graduate Theses and Dissertations

5-2015

Top-down Aluminum Induced Crystallization for Photovoltaics

Seth Daniel Shumate
University of Arkansas, Fayetteville

Follow this and additional works at: https://scholarworks.uark.edu/etd

Part of the Electromagnetics and Photonics Commons, Oil, Gas, and Energy Commons, and the Power and Energy Commons

Citation

Shumate, S. D. (2015). Top-down Aluminum Induced Crystallization for Photovoltaics. *Graduate Theses and Dissertations* Retrieved from https://scholarworks.uark.edu/etd/1111

This Dissertation is brought to you for free and open access by ScholarWorks@UARK. It has been accepted for inclusion in Graduate Theses and Dissertations by an authorized administrator of ScholarWorks@UARK. For more information, please contact scholar@uark.edu.

Top-down Aluminum Induced Crystallization for Photovoltaics

Top-down Aluminum Induced Crystallization for Photovoltaics

A dissertation submitted in partial fulfillment
of the requirements for the degree of
Doctor of Philosophy in Microelectronics-Photonics

by

Seth Daniel Shumate
Hendrix College
Bachelor of Arts in Physics and Spanish Literature, 2002
University of Arkansas
Master of Science in Microelectronics-Photonics, 2008

May 2015
University of Arkansas

This dissertation is approved for recommendation to the Graduate Council.

Dr. Hameed Naseem
Dissertation Director

Dr. Shui-Qing Yu
Committee Member

Dr. William F. Oliver III
Committee Member

Dr. Douglas A. Hutchings
Committee Member

Prof. Ken Vickers
Ex-Officio Committee Member

The following signatories attest that all software used in this dissertation was legally licensed for use by Seth Shumate for research purposes and publication.

___________________________________ ___________________________________

Mr. Seth Shumate, Student Dr. Hameed Naseem, Dissertation Director

This dissertation was submitted to http://www.turnitin.com for plagiarism review by the TurnItIn company's software. The signatories have examined the report on this dissertation that was returned by TurnItIn and attest that, in their opinion, the items highlighted by the software are incidental to common usage and are not plagiarized material.

___________________________________ ___________________________________

Dr. Rick Wise, Program Director Dr. Hameed Naseem, Dissertation Director

Abstract

Passivating silicon solar cell surfaces is critical to fabricating very high efficiency and low cost photovoltaic devices. The sun-facing surface of the solar cell, known as the emitter, is particularly important when designing a solar cell. This work focused first on an alternative method of forming the emitter of silicon solar cells, and secondly on a method for improving the surface passivation of both these non-traditional and standard n-type solar cells.

Top-down aluminum induced crystallization (TAIC) was used for forming a polycrystalline silicon layer from amorphous silicon using aluminum to catalyze the crystallization at much lower temperatures than otherwise possible. Inherent to TAIC is the doping of the resultant crystalline silicon by the aluminum, an acceptor impurity. Thus, n-type solar cells with p-type polycrystalline emitters were fabricated. It was found that several variations of this crystallization process occurred and their effect on solar cell performance was analyzed. An inherent disadvantage to this method was the presence of defects at the junction of the highest efficiency solar cells fabricated. These defects were passivated by an atomic hydrogen treatment.

Another method of improving solar cells was invented, theoretically modeled, and experimentally explored. The process improves silicon solar cells by hydrogen inactivation of acceptor impurities in the emitter (shown for both aluminum and boron in silicon). Low surface doping has been linked to lower measured surface recombination velocities for solar cell emitters with high quality dielectric passivation layers. By lowering emitter doping levels, n-type solar cell efficiencies were increased.

Acknowledgements

"Champagne for my real friends and real pain for my sham friends" – Edward Norton, the 25th Hour (Spike Lee, Director)

I thank Dr. Douglas Hutchings, Dr. Hameed Naseem, Dr. Terry Tremwel, M.K. Hafeezuddin, M.G. Young, Mirna Khairallah (Shumate), Richard Monroe Shumate Sr., Sherry Norrell, and Tom Norrell.

This work was funded in part by NSF award #EPS-1003970, NSF award #1047269, NSF award #1248962, DOE SunShot Incubator 8 award #EE-0006461 and Silicon Solar Solutions, LLC. Research possible through the use of the High Density Electronics Center at the University of Arkansas, Fayetteville campus.

Chapters 2 and 3 are each largely reproduced from publications in the IEEE Photovoltaics Specialists Conference. Use of the edited articles are specifically allowed under the copyright agreement for personal use of the articles reproduced here:

Part of Chapter 2 was originally published as:

S. D. Shumate, M. K. Hafeezuddin, H. A. Naseem, D. A. Hutchings, "Microstructural Influence of Hydrogenated Amorphous Silicon on Polycrystalline Emitter Solar Cells Prepared by Top-down Aluminum Induced Crystallization," Proc. of the 2011 IEEE PVSC, Seattle, Washington, June 19-24, 2011.

Part of Chapter 3 was originally published as:

S.D. Shumate, M.K. Hafeezuddin, D.A. Hutchings, and H.A. Naseem, "Large-Grain Polysilicon Seed Layers on Glass for Epitaxial Silicon Solar Cells," IEEE 38th PVSC, 2012.

Table of Contents

CHAPTER 1: INTRODUCTION ... 1

1.1 Motivation ... 1

1.2 Solar Industry ... 1

CHAPTER 2: TAIC EMITTER SOLAR CELLS ... 8

2.1: Mostly crystallized TAIC Solar Cells ... 20

2.2: Partially Crystallized TAIC Solar Cells ... 28

2.3: Layer Exchange TAIC Solar Cells ... 30

2.5: Effect of Rapid Thermal Annealing ... 34

2.6: Effects of Hydrogenation on TAIC Solar Cells ... 34

2.8: Effects of amorphous silicon quality on TAIC emitter solar cells ... 36

2.7: a-SiC:H Crystallization-Stop Layer ... 43

2.8 Notable Anomalous Interactions ... 44

CHAPTER 3: TAIC SEED LAYERS ON GLASS FOR EPITAXIAL SOLAR CELLS ... 46

CHAPTER 4: HYDROGENATED SELECTIVE EMITTER ... 58

4.1 Hydrogen Inactivation of Acceptor Impurities in Silicon ... 60

4.2 Boron-Hydrogen complex profile in silicon ... 63

4.3 Hydrogenation Apparatus and Efficacy Experiments ... 65

4.4 Effect of Substrate Temperature ... 67

4.5 Thermal Restoration of Original Resistivity ... 68

4.5 Hydrogenation with varying H_2 Pressure ... 69

4.7 Theoretical Simulations of the Hydrogenated Selective Emitter ... 74

CHAPTER 5: EXPERIMENTAL PROOF OF CONCEPT FOR THE HYDROGEN SELECTIVE EMITTER ... 82

5.1 Fabrication of Diffused Junction Solar Cells ... 82

CHAPTER 6: CONCLUSIONS AND FUTURE WORK ... 94

References ... 96

Appendix A: Description of Research for Popular Publication ... 104

Appendix B: Executive Summary of Newly Created Intellectual Property ... 106

Appendix C: Potential Patent and Commercialization Aspects of Newly Created IP ... 107

Appendix D: Broader Impact ... 108

Appendix E: Microsoft Project Printout 109
Appendix F: Identification of All Software Used in Research and Dissertation 110
Appendix G: All Publications Published, Submitted and Planned 111

List of Figures

Figure 1.1 Installed photovoltaic capacity by segment per year. 2
Figure 1.2 Process flows of Top-down Aluminum Induced Crystallization. 4
Figure 2.1 Schematic illustrations of the aluminum-induced layer exchange process (ALILE). 8
Figure 2.2 TAIC solar cell characteristics determining efficiencies: 12
Figure 2.3 Remaining 532 nm laser power versus depth for amorphous and crystalline silicon. 14
Figure 2.4 Absorption coefficients for a-Si:H and crystalline silicon vs. wavelength. 15
Figure 2.5 Simulated HIT solar cells.. 16
Figure 2.6 Jsc results from simulation of varying thickness of a-Si:H 17
Figure 2.7 Light J-V curve of the device structure shown. 18
Figure 2.8 Raman spectrum for the emitter of a mostly crystallized TAIC solar cell 19
Figure 2.9 Raman spectrum of intrinsic silicon. 20
Figure 2.10 Reflection of silicon and AM1.5 photon flux vs. wavelength. 21
Figure 2.11 Raman scattering spectrum for the highest efficiency TAIC solar cell. 23
Figure 2.12 External Quantum Efficiency curve for fully crystallized TAIC solar cell. 24
Figure 2.13 Cross-sectional SEM Image of highest efficiency TAIC emitter solar cell. 26
Figure 2.14 HRSEM image of an almost fully crystallized TAIC solar cell surface. 27
Figure 2.15 Cross-sectional TEM image and SAED patterns of TAIC emitter solar cell. 28
Figure 2.16 Raman spectrum of the emitter of a partially crystallized TAIC solar cell. 29
Figure 2.17 External quantum efficiency of a partially crystallized TAIC solar cell. 30
Figure 2.18 Raman spectrum from a layer-exchanged TAIC emitter solar cell. 31
Figure 2.19 Quantum efficiency for a layer-exchanged TAIC emitter solar cell. 32
Figure 2.20 Surface view of mostly layer exchanged TAIC emitter. 33
Figure 2.21 Dark J-V curves and Light J-V characteristics before and after hydrogenation. 35
Figure 2.22 640cm^{-1} wavenumber gaussian peaks. 39
Figure 2.23 Example J-V curve under AM1.5 all film types. 40
Figure 2.24 Surface view of TAIC emitters with distinct amorphous silicon. 41
Figure 2.25 FTIR spectra of before and after annealing a-SiC:H 43
Figure 2.26 Raman spectrum of the TAIC sample with the highest Voc. 45
Figure 3.1 Cell architecture used by NREL. 48
Figure 3.2 EBSD and SEM of TAIC large-grain polysilicon films on glass. 49
Figure 3.3 J-V curve for TAIC seed layers with grain gaps. 50
Figure 3.4 TAIC seed layer on glass with grain gaps present along edges. 52
Figure 3.5 Cross sectional TEM of TAIC thin-film silicon on glass. 53
Figure 3.6 Cross sectional TEM image of epitaxial silicon on TAIC seed layer. 54
Figure 3.7 EDS scan of TAIC seed layer. 55
Figure 3.8 Plan-view TEM image and SAED patterns of a TAIC seed layer. 56
Figure 4.1 Process flows for solar cells and industrially relevant selective emitters. 58
Figure 4.2 Surface recombination velocity vs. surface dopant concentration 59
Figure 4.3 Anti-bonding location of the boron-hydrogen complex in crystalline silicon. 60

Figure 4.4 Trap-limited diffusion coefficients of hydrogen in boron-doped silicon 62
Figure 4.5 Percentage of electrically inactivated boron vs. depth 63
Figure 4.6 Modified boron profile extracted from experimental data 64
Figure 4.7 Atomic hydrogen annealing system. 66
Figure 4.8 % Increase in resistivity... 68
Figure 4.9 Resistivity change with annealing cycles. 69
Figure 4.10 Atomic hydrogen inactivation vs. H_2 gas pressure.. 70
Figure 4.11 Sample placement for uniformity study 72
Figure 4.12 Sample placement for uniformity study after MPZ 5 relocation............................. 73
Figure \4.13 Boron-hydrogen complex concentration versus depth... 76
Figure 4.14 [B-H] profiles from applied to a boron profile.. 77
Figure 4.15 Surface SRH recombination versus SRV 79
Figure 4.16 Auger recombination in the emitter versus SRV.. 80
Figure 5.1 Boron profile before and after HSE.. 84
Figure 5.2 Reflection of solar cell surface vs. wavelength 85
Figure 5.3 EQE of Wafer A solar cells before and after HSE 86
Figure 5.4 Profile changes versus HSE time. 89
Figure 5.5 EQE curves for four solar cells before and after the HSE process............................ 93

List of Tables

Table 2.1 Mobility of ALILE layers on glass or quartz substrates 9
Table 2.2 High efficiency and simulated TAIC cell compared to the highest efficiency cell 21
Table 2.3 Si-H bonding properties of a-Si:H with varying deposition conditions. 37
Table 3.1 Comparison table of TAIC thin-film solar cell and NREL solar cells. 51
Table 4.1 Data from uniformity study of the hydrogen annealing chamber............................... 72
Table 4.2 Data for uniformity study after the chamber moved from MPZ5............................... 73
Table 4.3 Simulated emitter characteristics for experimental and estimated HSE emitters. 77
Table 5.1 Modeled emitter characteristics of the profiles from varying HSE time. 90
Table 5.2 Modeled SRV values based on experimental QE data and EDNA simulations. 92

CHAPTER 1: INTRODUCTION

1.1 Motivation

Great strides have been made in silicon photovoltaics. The record-holding 25.0% efficient silicon cell was created over a dozen years ago [1.1]. Due to its complexity, however, it is not currently manufacturable for a competitive cost and simply serves as a target of device design. While efficiency is important, the real goal of solar photovoltaics (PV) is to achieve the lowest manufacturable cost per peak-watt ($/Wp) while maintaining efficiencies just high enough to keep installation costs minimized. In order for research to have a near-term impact on this industry, any efficiency gains must outweigh the monetary penalty of implementation. This research involves two industrially feasible approaches to substantially reduce cost and/or increase efficiency of crystalline silicon photovoltaics.

1.2 Solar Industry

Every hour, the sun delivers enough energy to the Earth's surface to provide for all the energy needs of the entire human population on an annual basis. However, until recently, solar energy has not been cost-competitive with traditional fossil fuel resources. The past 10 years in the solar industry have seen innovation coupled with reaching economies of scale. The industry used to rely on polysilicon supply from the integrated circuits (IC) industry. Once demand for solar outstripped supply for polysilicon around 2008, the cost for polysilicon reached a maximum of $450/kg to projections of below $20/kg in 2013 [1.2]. The reason for such a steep decline was vertical integration. Too many major manufacturers, mostly Chinese-based companies, began producing their own polysilicon, and now the solar polysilicon market is in oversupply.

In the years leading up to this climax of polysilicon prices in 2008, a lot of progress, investment, and innovation around non-silicon technologies and thin-film silicon approaches to PV gained momentum. The main competitors to silicon's domination of the PV industry have been based on the material systems of cadmium telluride (CdTe), copper-indium-gallium-selenide (CIGS), and amorphous/microcrystalline silicon (micromorph tandem junction solar cells). Other technologies perhaps a little further behind than these three, at least in terms of commercial sales, are organic-based, multi-junction III-V based, perovskite, and dye-sensitized solar cells. Despite this competition, silicon still retains about 90% PV market share with the most cost-effective $/Wp. Figure 1.1 shows the recent and projected market share for thin-film (CdTe, CIGS, and a-Si:H-based technologies), p-type, and n-type silicon [1.3], [1.4].

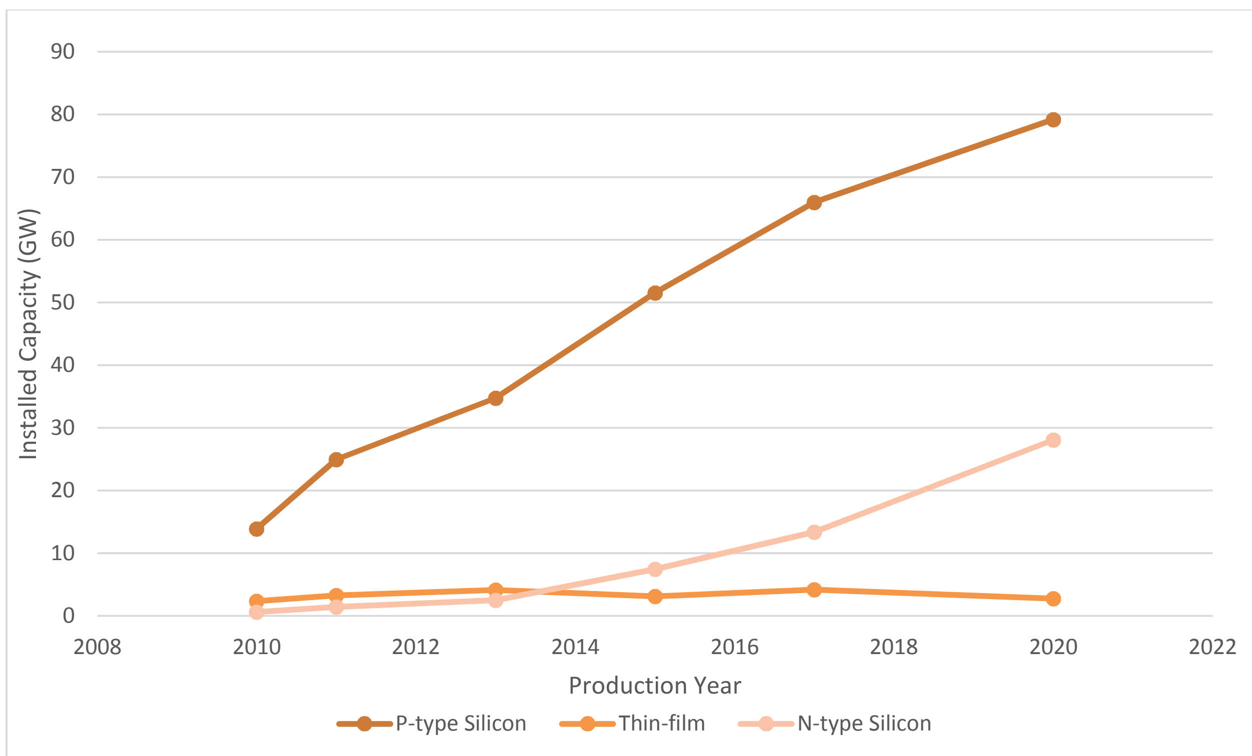

Figure 1.1 Installed photovoltaic capacity by segment per year.

P-type silicon was historically used due to its proven radiation hardness for space applications. Since most high-energy radiation is absorbed in the atmosphere, this design

requirement does not hold for terrestrial PV applications. N-type silicon is seen as the superior material for silicon-based terrestrial photovoltaics due to a resistance to metallic impurities and a lack of boron-oxygen complexes which also reduce minority carrier lifetime. Although the resistivity range for n-type silicon is harder to control due to the lower segregation coefficient of phosphorus in silicon, this issue may have been overcome by continuous Czochralski processes [1.4]. Since p-type silicon solar cells may degrade by up to a few absolute percent efficiency under illumination and generally have lower minority carrier lifetime, there is a focus in the industry to move to n-type. Three major manufacturers use n-type material with many others having the switch to n-type on their technology roadmaps [1.4]: Panasonic, SunPower, and Yingli. This market shift has commercial implications for the top-down aluminum induced crystallization (TAIC) emitter solar cells as well as the hydrogen selective emitter (HSE) process explored in this work.

Another major technological trend in academic research and industrial manufacturing has been the use of thin crystalline silicon technologies to replace wafer-based PV and amorphous silicon display technology. While much of the impetus for this type of work as well as thin-film approaches based on other materials systems has disappeared since the polysilicon price plunge, wafers still account for about 40% of a finished module cost [1.5]. However, hundreds of millions of dollars have been invested in these approaches on the promise of PV modules with crystalline silicon efficiencies at thin-film prices. The research in this work falls under the category of a seed-layer/epitaxy approach. The goal of this approach is to epitaxially grow a solar cell absorber either homo- or hetero-epitaxially onto a seed layer which resides on an inexpensive substrate such as glass or stainless steel. This approach has very low silicon usage. Industry standard solar cells today use about 5-6 g Si/W_p. Cells with the seed-layer/epitaxy

approach could use as little as 0.05 g Si/W_p while reaching efficiencies comparable to those achieved by wafer-based silicon solar cells.

The approach for creating seed layers as well as emitters for wafer-based solar cells was the TAIC process. This is a variation of metal induced crystallization wherein the interaction between silicon and a metal results in crystallization well below the temperatures required for solid phase crystallization of hydrogenated amorphous silicon (a-Si:H). These emitters and seed layers were assessed for their potential in high efficiency photovoltaics through theoretical considerations coupled with experimental validation. Figure 1.2 shows a very basic flow-chart

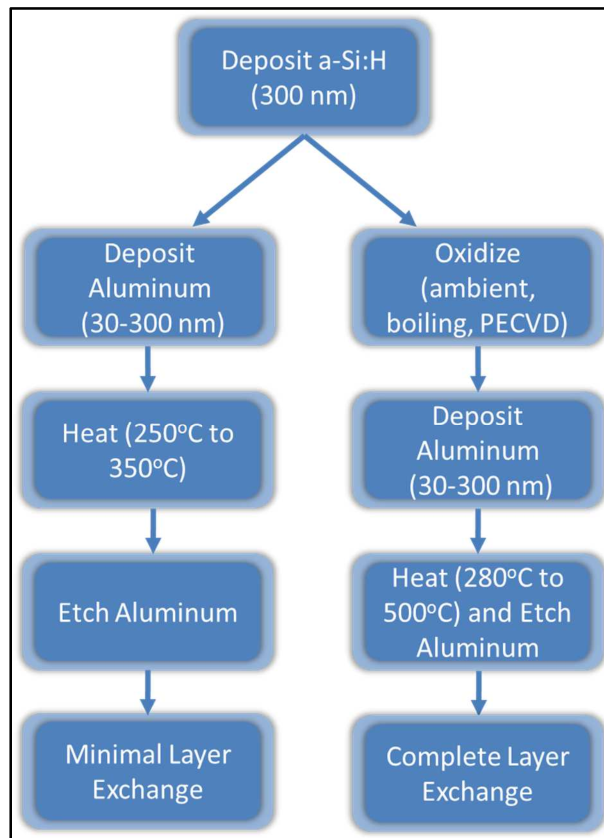

Figure 1.2 Process flows of Top-down Aluminum Induced Crystallization.

of generic parameters used throughout the research in this dissertation. The variation on the left was used for p-type emitters of wafer-based solar cells and the variation on the right was used to

create seed layers on glass for epitaxial thickened solar cells. Other variations and combinations of these two modes of crystallization or lack of crystallization were observed and are discussed in more detail in Chapter 2 in addition to implications for photovoltaic device fabrication.

Understanding of the TAIC emitter solar cells, the TAIC seed layer thin-film silicon solar cells, and the HSE solar cells required device modeling. Three different programs were used to obtain quantifiable insights into experimental observations for each of the aforementioned technologies: PC1D, AMPS-1D, and EDNA [1.6]-[1.8]. Each software package has its own advantages. PC1D is the most commonly used PV simulation tool in both research and industry. AMPS-1D has the advantage of modeling interface defect states which PC1D does not offer. This was a very important choice for TAIC emitter solar cells because the p-n junction of these devices lies at the interface between the crystallizing amorphous silicon (p-type) and crystalline silicon (n-type). EDNA was important for modeling the HSE solar cells because it is the only software package which allows for a custom dopant profile. Experimental and analytical work was performed at the High-Density Electronics Center (HiDEC), the Arkansas Advanced Photovoltaics Research Center, University of Arkansas-Fayetteville Nanoscience and Engineering, the National Renewable Energy Labs, and Solecon Labs, Inc.

The TAIC process has several relevant applications for the creation of both wafer-based and thin-film solar cells. Chapter 2 focuses on the work done for TAIC emitter solar cells. Major results include the highest efficiencies reported for this type of solar cell. Spectra of aluminum-silicon interactions were observed ranging from aluminum doping of amorphous silicon with very minimal crystallization, partial crystallization, minimal layer exchange with extensive crystallization, and full layer exchange with extensive crystallization. Most of these

possibilities were observed, analyzed, and fabricated into solar cells. Solar cell output parameters, theoretical modeling, and future work are discussed.

Seed layer development to date is the subject of Chapter 3. Collaboration between Silicon Solar Solutions, LLC and the National Renewable Energy Laboratories was developed based on this work. Contributions of others will be distinguished from the contribution from the author, however both sets of results will be presented with original analysis to provide a complete understanding of TAIC seed layers. Material requirements for thin-silicon solar cells will also be discussed at the end of Chapter 3.

Thin-silicon solar cells are achievable with epitaxial growth of silicon on TAIC seed layers. One method for relatively low temperature, high-growth rate epitaxy developed recently is hot-wire chemical vapor deposition (HWCVD). The distinction between HWCVD and CVD is essentially that a hot, current-carrying filament rather than the substrate surface dissociates the precursor gas. This allows the substrate to be at lower temperatures, opening the possibility for using cheap substrates such as display glass. A system in the Arkansas Advanced Photovoltaics Research Center (AAPRC) was modified for HWCVD.

Efficiency of thin silicon solar cells is dominated by surface recombination. Hydrogenation was investigated to control the electrically active acceptor impurity concentration of aluminum in silicon. Since the aluminum dopant concentration of TAIC thin films is inherently p+, the ability to control the doping of TAIC thin films could be important for several device applications. Through researching hydrogen's capability to electrically inactivate acceptor impurities in silicon, a novel use of this phenomenon was invented.

The hydrogen selective emitter (HSE) technology for creating selective emitters or selective back-surface fields for solar cells is discussed in Chapter 4 and Chapter 5. Theoretical, experimental, and device work is presented. The vacuum chamber modified for hot-wire hydrogenation was used for atomic hydrogen treatment of both TAIC solar cells to reduce junction recombination and TAIC thin-films on glass. TAIC thin-films on glass were used to optimize the hydrogenation chamber. In turn, the hydrogenated selective emitter invention is applicable to both TAIC solar cells and thin TAIC cells on glass, creating a suite of crystallized materials. The invention of an enabling hydrogenation technology also has stand-alone research and commercial potential. Chapter 6 includes overall conclusions and future work for each of these topics.

CHAPTER 2: TAIC EMITTER SOLAR CELLS

Amorphous silicon is a highly defective, direct band gap semiconductor material. Its electrical quality can be increased by the introduction of hydrogen. Plasma-enhanced chemical vapor deposition (PECVD) using a silane gas (SiH_4) is a method of choice for depositing high-quality, hydrogenated amorphous silicon (a-Si:H). Metal induced crystallization is a phenomenon in which amorphous silicon crystallization is catalyzed at temperatures lower than those required by solid phase crystallization. Several metals have been identified to have this property [2.1]. Of all the metals, however, aluminum is the most promising as it contributes as a high level acceptor impurity [2.2]. Aluminum is also the third most abundant element in the Earth's crust.

Aluminum induced crystallization of a-Si:H has been performed with several different aluminum/a-Si:H layered configurations. Most of the work has been focused on aluminum induced layer exchange (ALILE) [2.3]-[2.40]. The initial and final ALILE configurations are shown in Fig. 2.1. On both silicon and non-silicon substrates, large-grained, randomly oriented

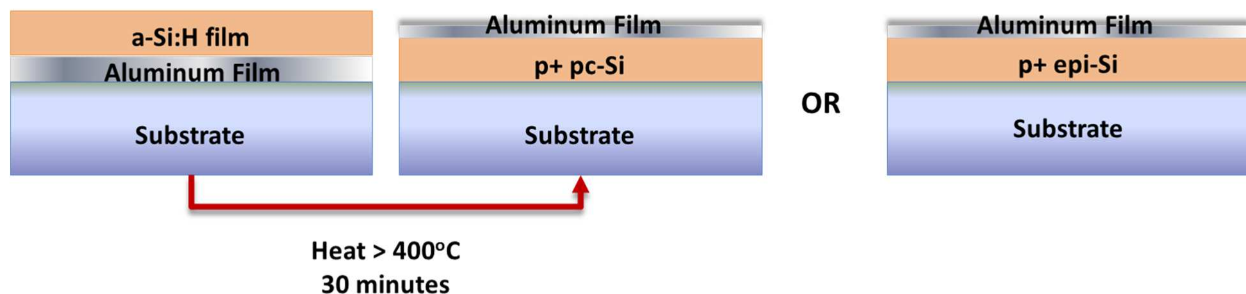

Figure 2.1 Schematic illustrations of the aluminum-induced layer exchange process (ALILE).

silicon occurs. In 1981, Tsaur, *et al.*, reported the possibility of a solid-phase epitaxy by this method and its application for solar cells. Equal thicknesses of 200 nm e-beam evaporated aluminum and a-Si were deposited on (100) and multicrystalline n-type wafers and annealed

between 400°C (4 hours) and 500°C (30 minutes) [2.3]. Excess interstitial aluminum was detected in the samples, which when annealed at 900°C increased carrier concentration and decreased hall mobility from 2×10^{18} cm^{-3} to 2×10^{19} cm^{-3} and 70 cm^2/Vs to 26 cm^2/Vs, respectively [2.3]. Solar cells made with this method achieved open-circuit voltages (Voc) of up to 540 mV on float-zone wafers [2.3]. This was the only report of using ALILE for the emitter of n-type wafer based cells found in literature. Table 2.1 lists reported mobilities for ALILE films from the literature. Compared to carrier mobility for single crystal silicon, the best material quality reported for this method was the polycrystalline sample from Jeong and Boo [2.40] with grain size around 15 μm. Interestingly, the mobility is slightly higher for the polycrystalline value than the solid-phase epitaxy film's mobility value reported by Tsaur, *et al.* [2.3].

Table 2.1 Mobility of ALILE layers on glass or quartz substrates

Al:a-Si Ratio	Important Details	Carrier Concentration (cm^{-3})	Mobility (cm^2/Vs)	Mobility of C-Si at same carrier concentration (cm^2/Vs)	Reference
1:1	8 nm Al_2O_3 at interface between aluminum and a-Si	1.1x10^{18}	90.91 (61.7% of maximum)	147.45	[2.40]
450-550 nm : 500 nm	No interfacial oxide mentioned	2.6x10^{18}	56.3	107.06	[2.5]
400 nm : 400 nm	No interfacial oxide mentioned	1x10^{19}	10	70.85	[2.14]
1 : 1.7	1 hour ambient oxidation	Up to 7.5x10^{19} for 34 nm film	21 (field-effect mobility)	51.3	[2.25]
200 nm : 200 nm	No oxide, Epitaxial	2x10^{18}	70 (59.4 % of maximum)	117.8	[2.3]

The most important characteristic when considering solar cells with deposited emitters rather than those formed by diffusion or ion implantation is open-circuit voltage (Voc); those recombination currents at the interface being especially detrimental. This is because the junction is now at the interface as opposed to traditional cells where the junction is hundreds of nanometers below the cell's surface. Any source of recombination within a diffusion length of the junction will decrease Voc. A good real-world example of the effect of interface defects on Voc for solar cells with deposited emitters is the heterojunction-with-intrinsic-thin (HIT) cell.

According to simulations, the Voc of a HIT cell can decrease by 20% if the number of interface defects such as unsatisfied silicon bonds increases from 10^{10} cm^{-2} to 10^{12} cm^{-2} [2.41]. This is approximately only 1 defect every 10 nm. Reduction in Voc has been found to be even more detrimental if the minority carrier barrier provided by the band offset of the i-a-Si:H is removed: cells with Voc approaching 600 mV had 300 mV without this layer when using doped microcrystalline silicon as the emitter [2.42]. Although not in commercial production, other types of solar cells with deposited or grown emitters have been reported as well.

Polycrystalline emitters for solar cells have the potential to dramatically increase the control with which solar cells are produced. Performance benefits have been both experimentally and theoretically explored [2.43]-[2.45] due to both reduced back injection current, decreased emitter thickness, and the absence of a dead layer. Previous work was plagued by high carrier losses from defective grain boundaries which override LPCVD films. Also, high deposition temperatures eliminate useful defect-passivating hydrogen. To mitigate these problems, thinner emitters were employed which resulted in relatively high sheet resistances [2.43]. However, open circuit voltages in excess of 650 mV were obtained on 0.1 Ωcm float zone wafers due to a minimized back injection current.

In order for high-efficiency polysilicon emitter solar cells to be viable, high throughput, low temperature processes must be utilized which result in well passivated films. One such method is Top-down Aluminum Induced Crystallization (TAIC) of hydrogenated amorphous silicon (a-Si:H). TAIC is a variant of metal induced crystallization in which little to no layer exchange occurs. Most research involving aluminum induced crystallization has focused on layer exchange in which the starting layer configuration is substrate/aluminum/a-Si:H and the final structure after annealing is substrate/polycrystalline-Si/aluminum. This structure has been used extensively as a seed layer for epitaxial growth of absorber layers for thin film polysilicon solar cells. However, such high temperature processes (>400°C) may act to eliminate hydrogen mediated defect passivation due to hydrogen effusion.

Work has been done with the TAIC configuration, substrate/a-Si:H/aluminum, involving the roles of stress, hydrogen content, and native interfacial oxide layers on crystallization. Only two works have implemented the process for the use as an emitter layer in wafer-based solar cells [2.46], [2.47]. Efficiencies up to 7.35% [2.47] have been reported without the incorporation of a back surface field or antireflection coatings and almost no reported optimization on the films themselves with respect to resulting solar cell performance. Section 2.8 of this chapter was previously published [2.48].

A more thorough investigation of these solar cells as well as guidelines for efficiency optimization is presented in this chapter. Higher values for each solar cell characteristic, new observations, and direct transmission-electron microscopy evidence of a-Si:H crystallization without layer exchange will be shown for the first time.

During the course of experimentation a spectrum of results were found. Observed phenomenon ranged from doping amorphous silicon to partial crystallization to full crystallization with minimal layer exchange to full layer exchange. The interesting thing is that each of these interactions may occur with the same processing parameters and different interactions were sometimes observed on a single sample. Specific causes for such a wide variation were not identified, but material quality implications for photovoltaic devices fabricated from these different emitters were characterized. Figure 2.2 is a graph of some of the solar cells fabricated and measured during the course of this research.

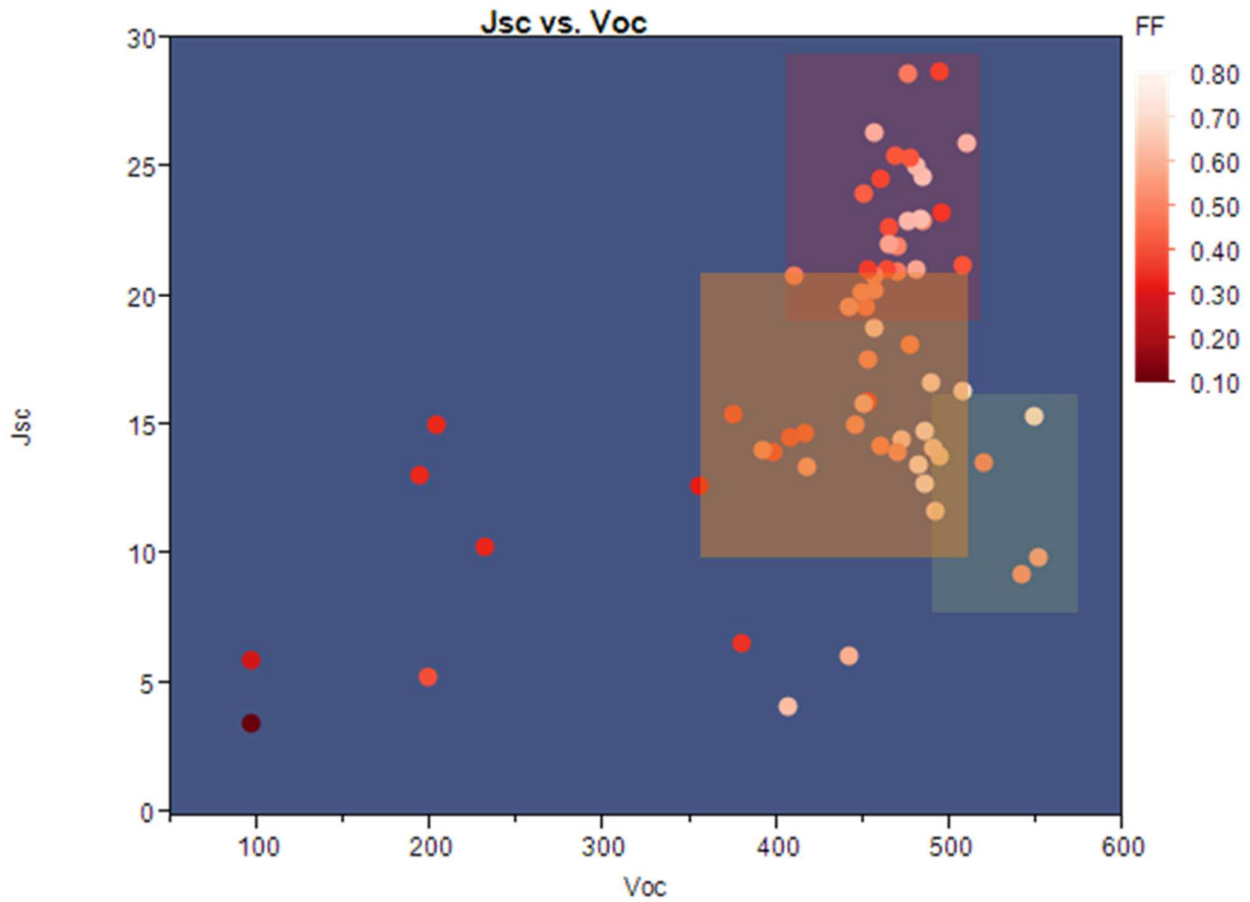

Figure 2.2 TAIC solar cell characteristics determining efficiencies: Jsc, Voc, and FF.

Most of the TAIC cells fabricated shown in Fig. 2.2 were processed under similar conditions: amorphous silicon deposited on n-type silicon capped with aluminum of less

thickness and annealed at temperatures of 350°C or less. The highest efficiency samples appear to have a Voc limit of just above 500 mV in the absence of BSF structures and surface passivation (light red box). These samples were found to be mostly crystallized by analysis of their Raman curves. The light orange box represents samples with low similar Voc and low Jsc. These were found to be samples with layer exchange. The samples with partial crystallization (light green box) were partially crystallized, benefitting from the passivation quality of intrinsic amorphous silicon. In order to understand how these emitters affect device performance, it was necessary to determine how much of the original amorphous silicon had crystallized and how much remained amorphous, as the two materials have distinct optical and electronic qualities.

Crystallization fraction was determined using Raman spectroscopy. Crystalline silicon has a characteristic, sharp peak at 520 cm^{-1} and a-Si:H has various peaks at 315 cm^{-1}, 400 cm^{-1}, and 480 cm^{-1} [2.49]. Once the Raman spectra were fitted to Gaussian curves for each of these peaks, the curves were integrated and a crystalline fraction X_c was found according to Eq. 2.1.

$$X_c = \frac{I_{Crystal}}{I_{Crystal} + I_{a-Si:H}} \qquad \text{Eq. 2.1}$$

$I_{crystal}$ and $I_{a\text{-}Si:H}$ are the areas under the Gaussian peaks mentioned. The wavelength of laser light used was 532 nm. The attenuation coefficient for green light is approximately an order of magnitude higher for amorphous silicon than crystalline silicon. Raman scattered light is shifted up in wavelength at room temperature to 545.9 nm and 547.15 nm for amorphous and crystalline silicon, respectively. So not only the laser light, but the scattered light is also much more attenuated for amorphous as opposed to crystalline silicon. These factors contribute to the qualitative nature of determining the crystalline fraction.

The crystalline fraction is an important predictor for a maximum possible short circuit current, J_{sc}. Amorphous silicon is a highly defective material with poor carrier transport properties compared to crystalline silicon. Additionally, as seen in Fig. 2.3, a-Si:H has much higher light absorption than crystalline silicon up to about 680 nm. Excellent silicon solar cells will have quantum efficiencies close to 100% in this very important wavelength range. 41% of the photons from 350 nm to 1200 nm are from the 350 nm to 680 nm range. For efficient TAIC solar cells, it is necessary to minimize the amount of parasitic amorphous silicon left. To put this into perspective, the HIT cell which uses less than 20 nm of doped and intrinsic a-Si:H as the emitter of its solar has been reported to lose 3.5 mA/cm^2 in J_{sc} compared to diffused junction silicon solar cells [2.42].

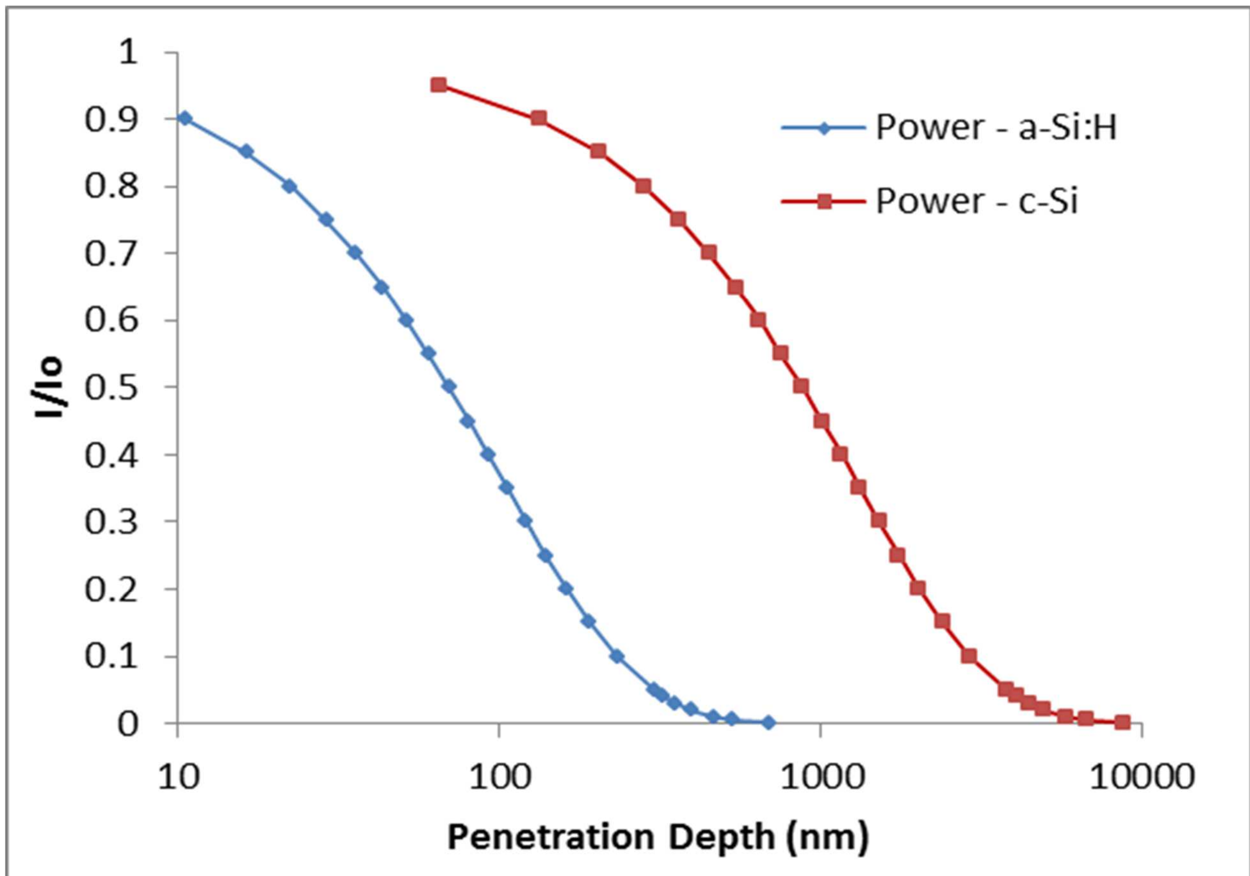

Figure 2.3 Remaining 532 nm laser power versus depth for amorphous and crystalline silicon.

Amorphous silicon thickness typically used in this study was 300 nm. Since the spectrum of observed TAIC interactions ranged from no crystallization to nearly full crystallization, a simple simulation based study of varying a-Si:H thickness was done to understand what Jsc values could be expected depending on crystallization fraction. AMPS-1D was used to model heterojunction solar cells with amorphous emitters of varying thicknesses. Parameters used follow the model published by Hernandez-Como and Morales-Acevedo [2.41] with the exception of front amorphous silicon thicknesses. Figure 2.4 shows the cross section of the modeled devices. Both intrinsic and doped amorphous layers were modeled with changing thickness alternatively.

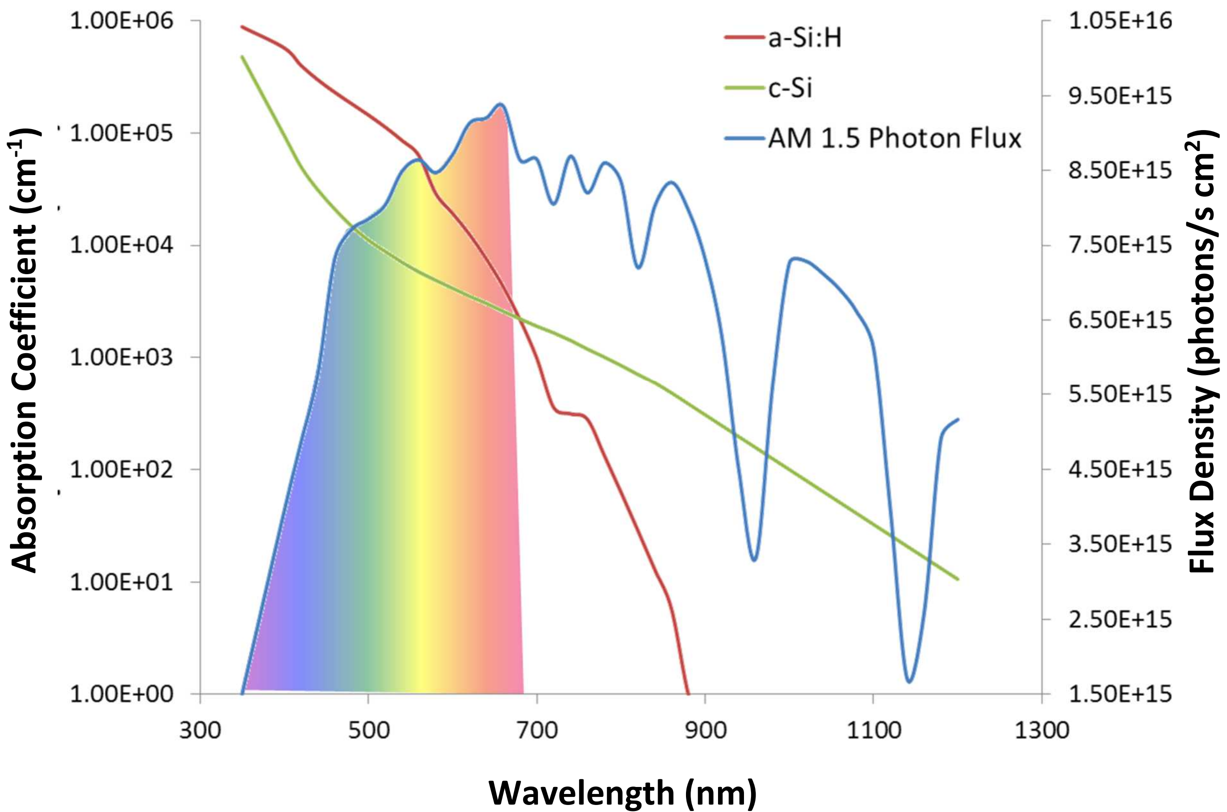

Figure 2.4 Absorption coefficients for a-Si:H (red) and crystalline silicon (green) vs. wavelength. Photon flux density is also shown versus wavelength (blue line) with the color range superimposed.

Figure 2.5 shows the results of these simulations; carrier collection was reduced with increasing doped or intrinsic a-Si:H thicknesses. However the reduction in Jsc was much more pronounced when the front surface intrinsic a-Si:H thickness was increased than when the p+ a-Si:H thickness was increased. In order to relate these results to the TAIC cells fabricated which had no intentional surface texturing or antireflection coatings, a front surface reflection of 25% was chosen.

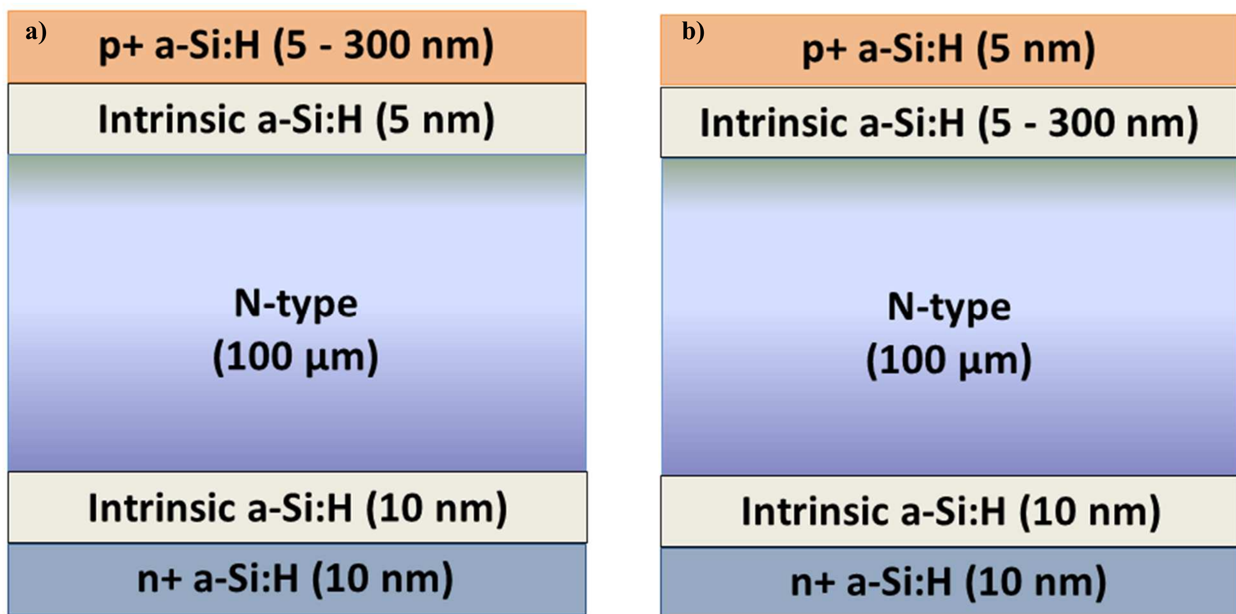

Figure 2.5 Simulated HIT solar cells. a) p+ a-Si:H front surface layer thickness was changed from 5 to 300 nm while i-a-Si:H layer was held constant at 5 nm. b) i-a-Si:H front surface layer thickness was changed from 5 to 300 nm.

Despite the differences in cell structure, this simple simulation study indicates two things: the highest efficiency cells reported in the previous thesis on this type of solar cell were most likely only partially crystallized and that at least some of the intrinsic a-Si:H remained undoped by aluminum during the crystallization process. In 1999, H.A.. El-Jammal reported a TAIC solar cell efficiency of 4.9% with Jsc = 14.6 mA/cm^2, Voc = 0.48, and FF = 0.7 [2.46]. As can be seen in Fig. 2.2, the Jsc values recorded from the solar cells made with the TAIC process have slightly higher Jsc than the simulated values in Fig. 2.6. This may be because on those samples, full

crystallization was achieved and little to no parasitic loss from excess a-Si:H was present. Further experimental evidence for this will be discussed in section 2.1.

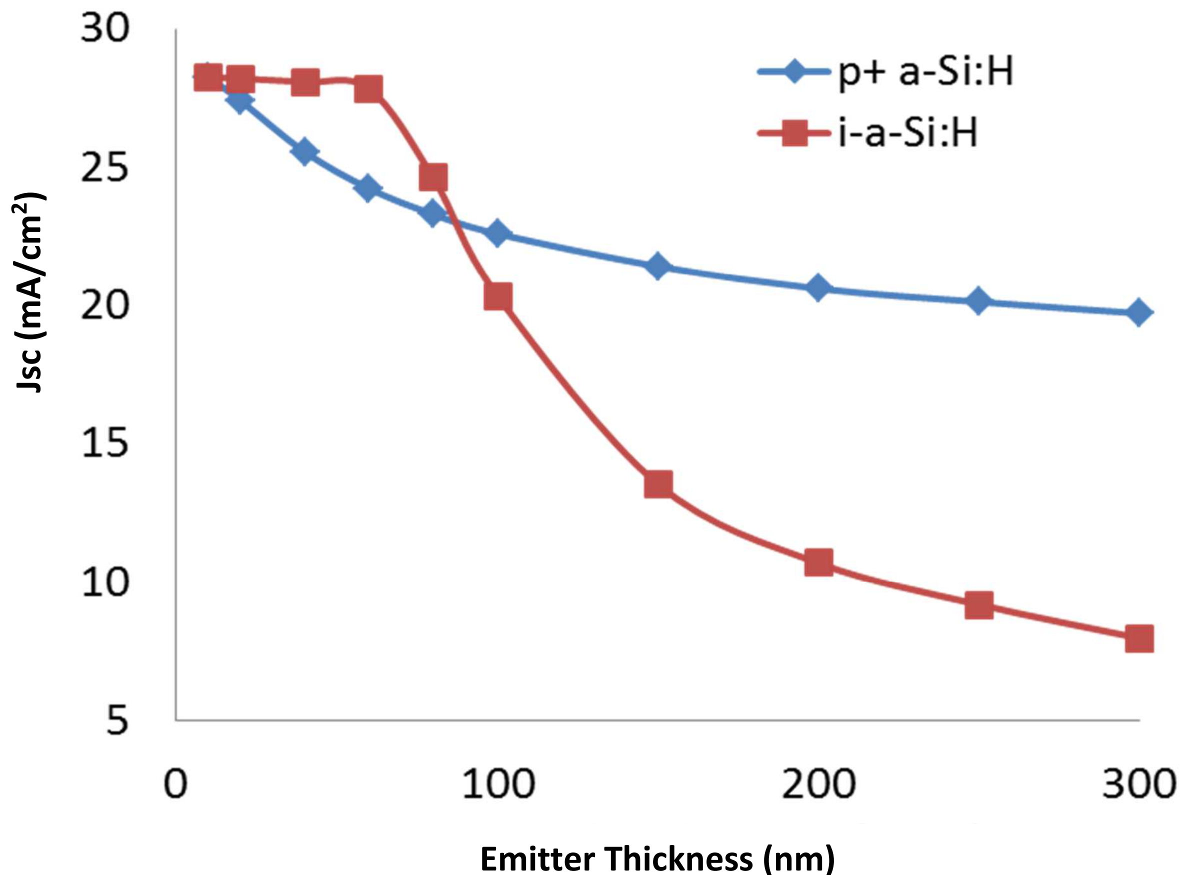

Figure 2.6 Jsc results from simulation of varying doped and undoped front surface a-Si:H layers in the HIT structures shown in Fig. 2.5.

The crystallization fraction was determined from the Raman spectra of an example TAIC cell. The structure of this cell is shown in Fig. 2.7 with its J-V curve. 300 nm of intrinsic a-Si:H was deposited onto an n-type substrate. The sample was quickly transferred to an evaporator and a 50 nm aluminum film was evaporated onto the amorphous silicon and the sample was annealed for 30 minutes under vacuum. Aluminum contacts were evaporated on the front and back of the cell and front grid was photolithographically defined. The cell was 5.85% efficient under one-sun conditions at room temperature.

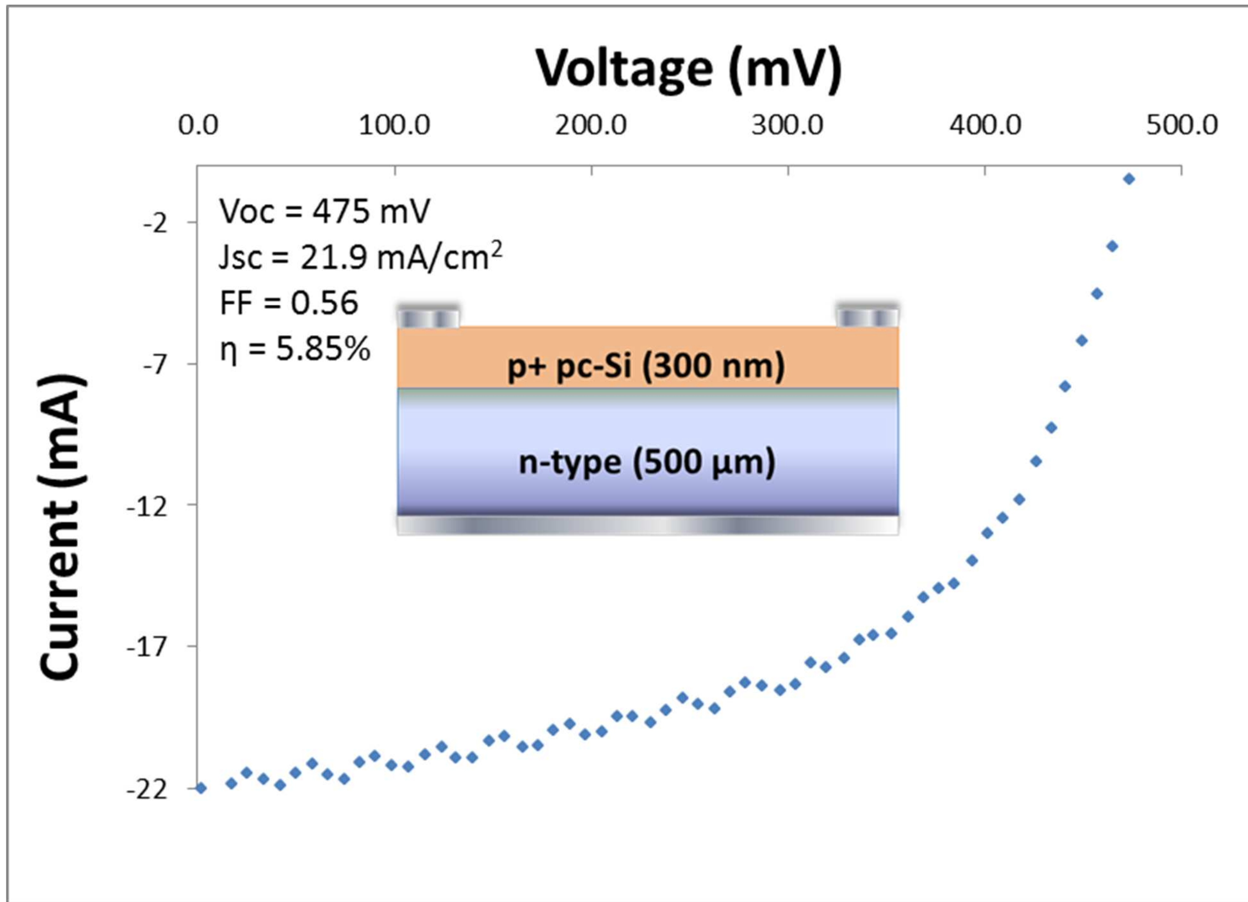

Figure 2.7 Light J-V curve of the device structure shown. Waviness near Jsc is due to varying power for the lamp array.

This solar cell has an emitter crystallization fraction of 87.6% following the fitting method and crystallization fraction calculation procedure in [2.49]. The crystalline fractions used in Eq. 2.1 were found by integrating the areas of the peaks at 515 cm^{-2} and 520 cm^{-2} for defective and crystalline silicon, respectively. The amorphous contribution was found by integrating the 480 cm^{-1} peak. The 400 cm^{-1} represents another phonon mode of the same amorphous volume and was not included in the calculation, consistent with [2.49] and [2.50]. Figure 2.8 shows the original data, four Gaussian fitting curves, and the cumulative curve (dotted line) closely matching the experimental data.

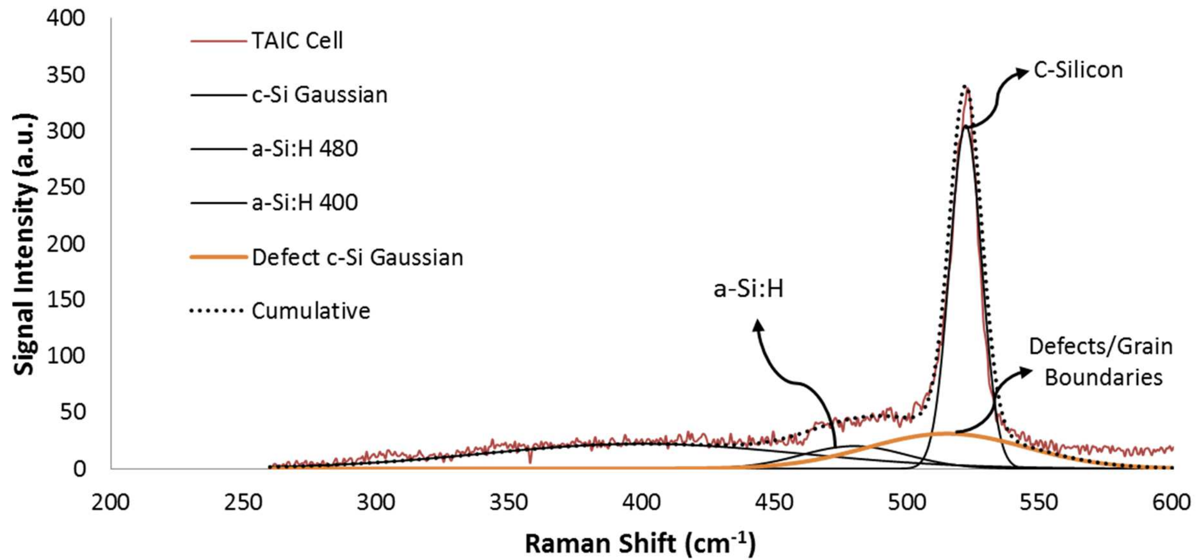

Figure 2.8 Fitted measured Raman spectrum for the mostly crystallized TAIC solar cell.

The broad peak at 515 cm^{-1} indicates that the TAIC material, contrary to layer exchanged material (see Chapter 3), at least for this sample, is highly defective, fine-grained polycrystalline silicon with a substantial fraction of a-Si:H remaining. Unfortunately, Raman spectroscopy yields no extractable information about the location of the mixed-phase material. This would be very useful information since carrier transport in an emitter with pockets of a-Si:H would behave differently than transport would in an emitter with an intact layer of a-Si:H. Although this is a quantitative assessment of the layer, it lends itself to only qualitative insights into the performance of TAIC emitter solar cells.

The defect peak is most likely exaggerated. Figure 2.9 shows the Raman signal from the same system from the intrinsic silicon calibration sample where no grain boundaries and very few defects should have been present.

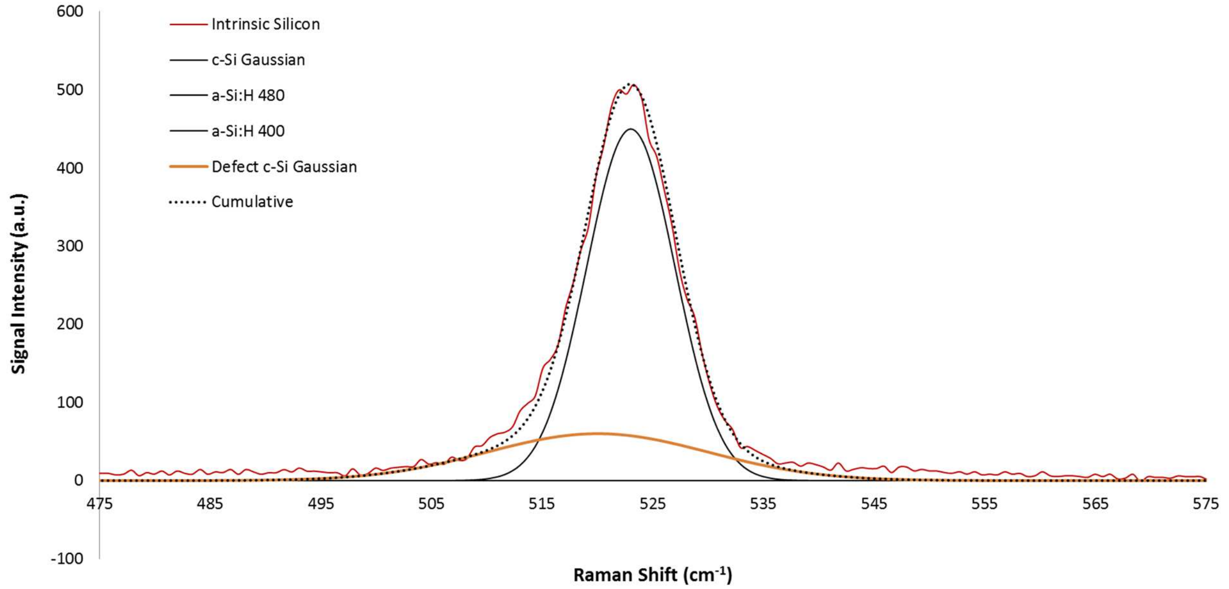

Figure 2.9 Raman spectrum of intrinsic silicon. No amorphous peaks present and an artificial defect peak was used to fit the measured data.

2.1: Mostly crystallized TAIC Solar Cells

The highest efficiency 1 cm^2 device produced was 7.26% at room temperature under 1-sun illumination. This is the highest efficiency ever reported for this type of solar cell. Obvious losses come from a lack of texturing, front and rear-side passivation, and a lack of antireflection coatings. The world's highest efficiency silicon solar cell had a short-circuit current of 42.7 mA/cm^2 [1]. Calculating the loss from the reflectivity of silicon (Fig. 2.10), this cell would have had a maximum of 28 mA/cm^2 without texturing or an anti-reflection coating.

A lack of front surface passivation would also decrease this current, but has a much more drastic effect on open-circuit voltage, which in turn lowers the maximum achievable fill factor. PC-1D was used to model a 23.8% efficient solar cell with a 300 nm emitter with a uniform doping of $1x10^{18}$ cm^{-3}, near the doping expected for full crystallized TAIC emitters. Changes made to further account for the physical and electrical structure of the fabricated cells were adapted from this model. A list of the important modeling parameters is given in Table 2.2. The

PC-1D simulation indicates a maximum efficiency of 10.8% for the devices fabricated in this chapter. PC-1D does not account for fill factor losses due to power loss in high sheet resistance emitters or losses due to grid coverage. This loss and other discrepancies are addressed below.

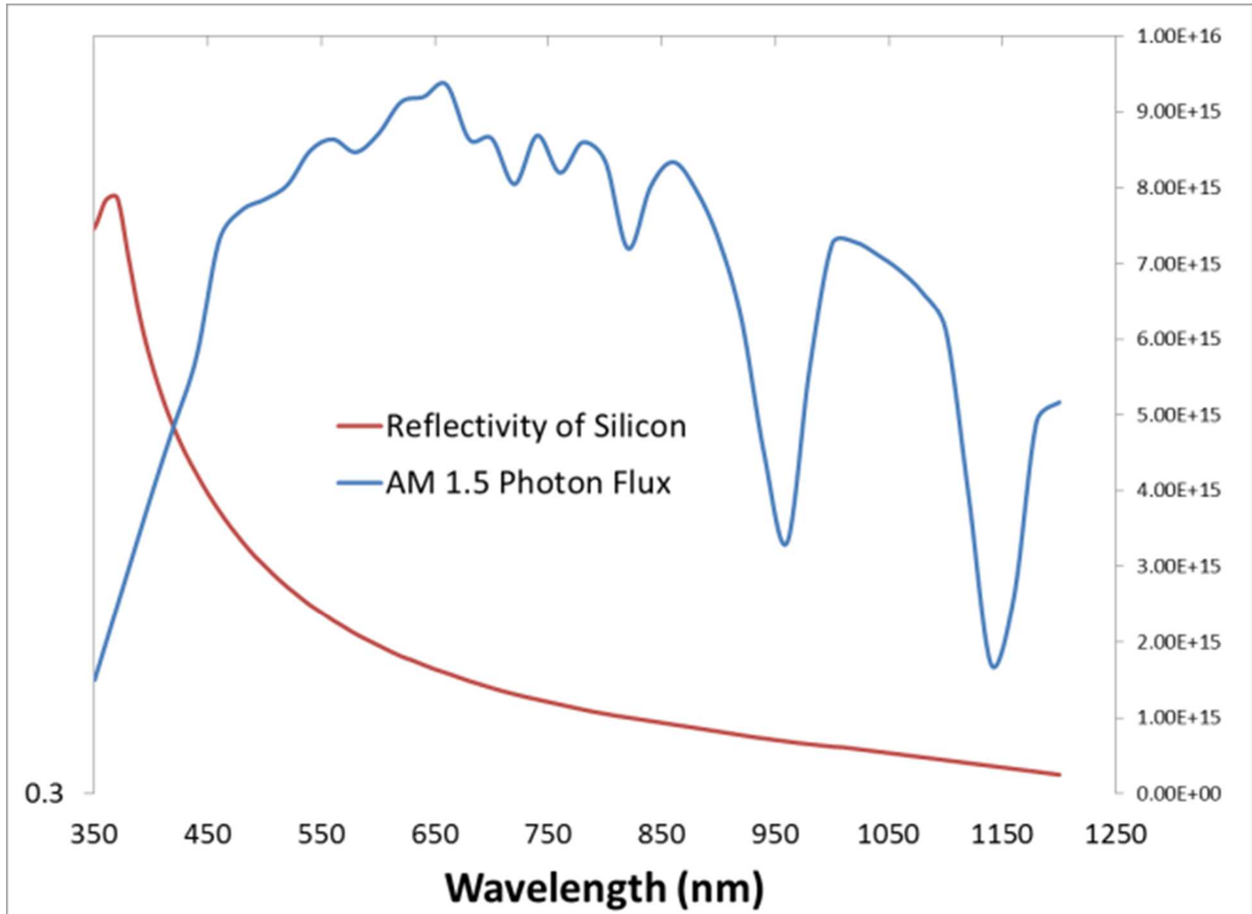

Figure 2.10 Reflection of silicon and AM1.5 photon flux vs. wavelength.

Table 2.2 High efficiency and simulated TAIC Cell structures compared to the actual highest efficiency cell fabricated.

Parameter	High Efficiency Cell	TAIC Cell	Best Actual Cell
Front Reflectance	2%	34.5%	No Texture/ARC
Bulk Lifetime (µs)	1000	150	Prime Grade/n-type
Front SRV (cm/s)	0	$1x10^6$	No Passivation
Rear SRV (cm/s)	0	$1x10^6$	No BSF
Voc (mV)	707.8	557.4	510
Jsc (mA/cm^2)	> 40	23.8	20.7
Fill Factor (%)	> 80	81.4	0.688
Efficiency (%)	23.8	10.8	7.26

The metal grid of the solar cells used in this work covers approximately 5% of the active area of the devices. This reduces the simulated Jsc for the TAIC Cell in Table 1 to 22.61 mA/cm^2 from a maximum of 23.8 mA/cm^2. Losses in Voc are most likely due to non-ideal junction recombination. Using the pseudo-fill factor equation with an ideality factor of 2 (the lowest observed for untreated TAIC cells), and the voltage of 510 mV obtained for this cell, the pseudo-fill factor assuming no losses due to poor grid design was found to be 0.69. This was very close to the measured value. Although the sheet resistance of these 300 nm emitters is relatively high at 1100 Ω/□, the power loss due to series resistance with such tightly packed grid lines (0.255 mm between lines) is negligible. This grid design was meant for concentrator solar cells which would have much higher I^2R power loss.

Raman scattering data for this solar cell indicated 97.92% crystallization fraction (Fig. 2.11). This would mean a remaining current loss due to parasitic absorption from amorphous silicon of 2.08%, reducing the simulated current even further to 22.14 mA/cm^2. The remaining 1.44 mA/cm^2 were likely lost due to the highly defective nature of non-layer exchange TAIC films. Using PC-1D with a minority carrier lifetime in the emitter of zero, the short circuit current density dropped by 1.8 mA/cm^2. Including all of these factors, the maximum theoretical efficiency for a TAIC solar cell following the fabrication scheme used here would be 8.73% assuming an ideality factor of 2, no front or rear surface passivation, material with a bulk lifetime of 150 μs, and the same crystallization fraction as that obtained by the highest real solar cell. However, similar unpassivated samples with well over 600 mV were obtained, albeit partially crystallized, the implications of which will be discussed in section 2.2.

The external quantum efficiency (EQE) for this cell is shown in Fig. 2.12. Also listed is the calculated short circuit current density for this cell of 23.89 mA/cm^2. This Jsc does not

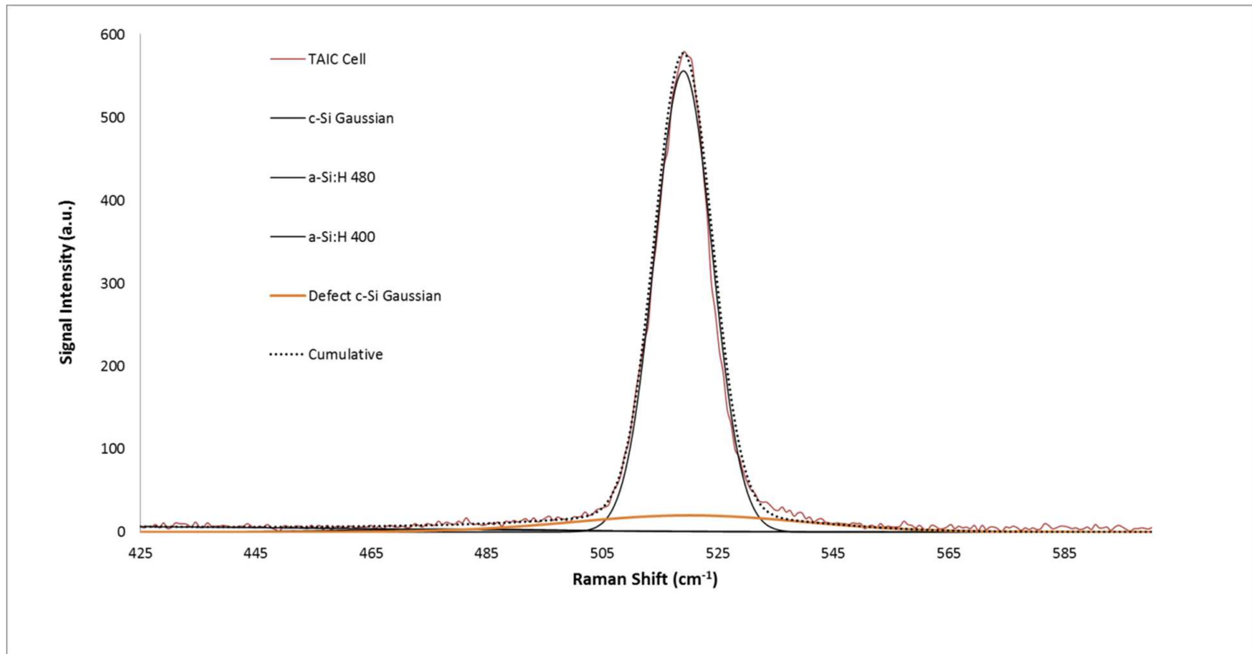

Figure 2.11 Raman scattering spectrum for the highest efficiency TAIC solar cell.

include grid contacts. The reflection of crystalline silicon as well as the ideal EQE based on this curve is shown. Several conclusions are immediately obvious from this curve. First, the short wavelength response is very poor. The main reason for this is because there is not an effective passivation layer on the surface of this cell. However, in comparison with a homojunction, which does not have as many defects in the emitter, it is also likely that the defective material quality in this TAIC emitter is causing additional losses. Auger recombination can be ruled out because the typical doping density of TAIC layers has been found not to typically exceed $1x10^{19}$. Another discrepancy, which is simply an artifact of non-ideal semiconductor physics is that the spectral response of real devices does not cut off at silicon's band gap (about 1100 nm or 1.124 eV). Despite that, it is also the case that this device has poor long-wavelength response, likely due to the absence of a back surface field and low quality base material. An effective back surface field will fill out the longer wavelength EQE curve to be more square to between 900-

1000 nm. Also, TAIC films, unless very low crystallization is observed, are typically textured.

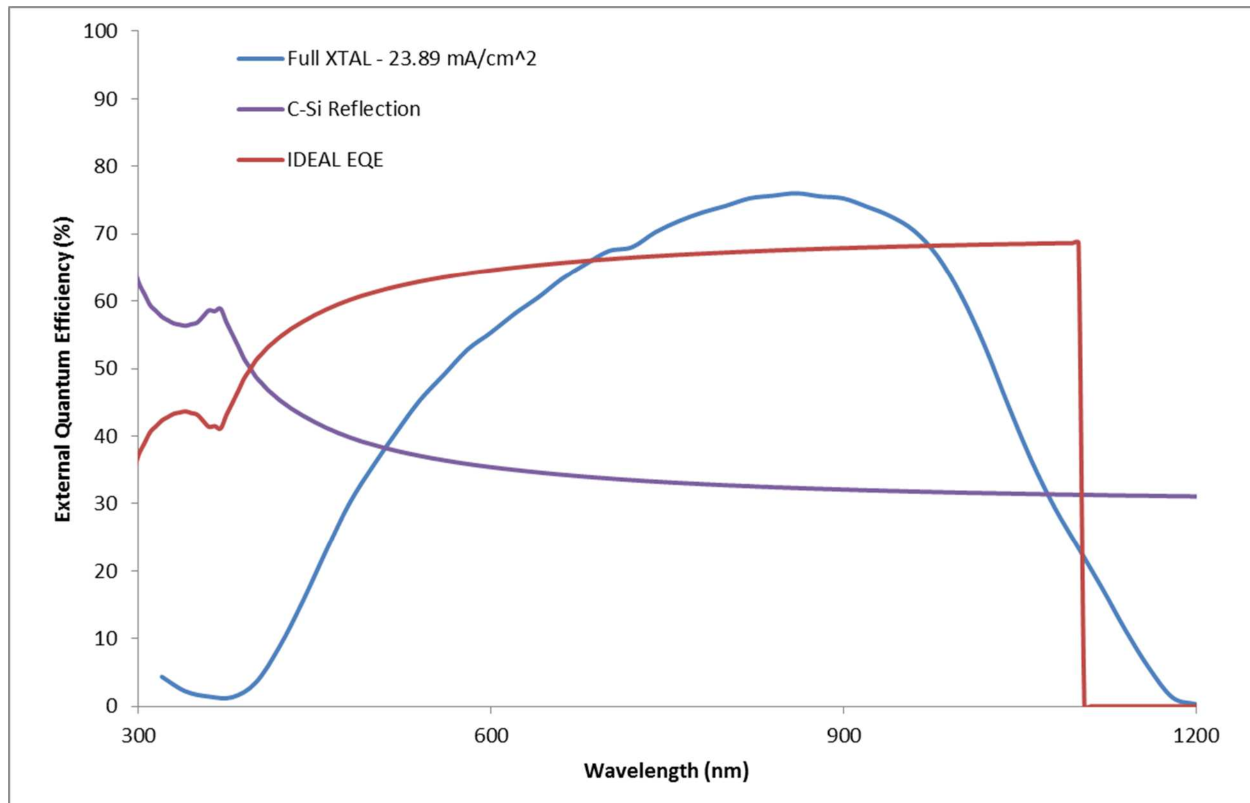

Figure 2.12 External Quantum Efficiency curve for fully crystallized TAIC solar cell (blue curve)

The surfaces scatter light, and according to this EQE curve, also help trap light. This is the only possibility for having a measured EQE higher than that of crystalline silicon if the assumption is that TAIC material is mostly crystalline silicon, an assertion supported by the crystallization fraction calculated from the Raman spectrum. The texturing of TAIC emitters is a very interesting feature of the process. The EQE peaks at 860 nm with a conversion of 76% of the incident photons into electrons. However, pyramidal texturing reduces reflection at these wavelengths to around 10%, yielding EQE of 90% assuming the bulk material is a high enough quality. While the reflection of TAIC emitters is superior to planar silicon, it does not match the performance of KOH preferential etching which creates (111) faced pyramids across the surface.

It would be interesting to create TAIC films on top of pyramidal textured silicon to see if the 90% EQE limit could be exceeded.

2.1.1 Microscopic characteristics of the highest efficiency solar cell

Cross-sectional SEM and TEM analysis was done on the highest efficiency TAIC solar cell. In order to enhance the fill factor, the crystallizing layer of aluminum was left. 350 nm aluminum was evaporated for the front contact. Areas were opened up via photolithography and 10 μm gridlines were left. The TEM sample was taken from a grid line in order to see the extent of layer exchange in the original 50 nm layer of aluminum. The TEM sample was prepared by digging out trenches with a Focused-Ion Beam capability of the FEI Nova HR-SEM. The sample was then lifted out and attached with platinum to the post of a TEM grid. SEM images reveal stark contrast between silicon and aluminum and insights into the crystallization process.

Figure 2.13 shows the cross-sectional HR-SEM image of the TEM sample. Dashed lines are meant to guide the eye. The top-most layer is platinum used to protect the sample from ion-beam damage during the focused-ion beam (FIB) cutting. The second layer down is the grid-line applied after the crystallization process. The third layer was the original aluminum layer. Since there is high contrast in the SEM image between aluminum and silicon, it is evident that some layer exchange for this sample has occurred. In the process of layer exchange, silicon dissolves into the aluminum layer and nucleates at grain boundaries. This nucleation leads to lateral solid-phase epitaxy within the aluminum layer (see Chapter 3). The layer-exchanged crystalline silicon is limited in thickness to the thickness of the original aluminum layer. However, as can be seen with the lighter shaded aluminum regions in the "polycrystalline layer" of Fig. 2.13, the aluminum mostly does not directly change places with the silicon. In this picture, roughly 3% of

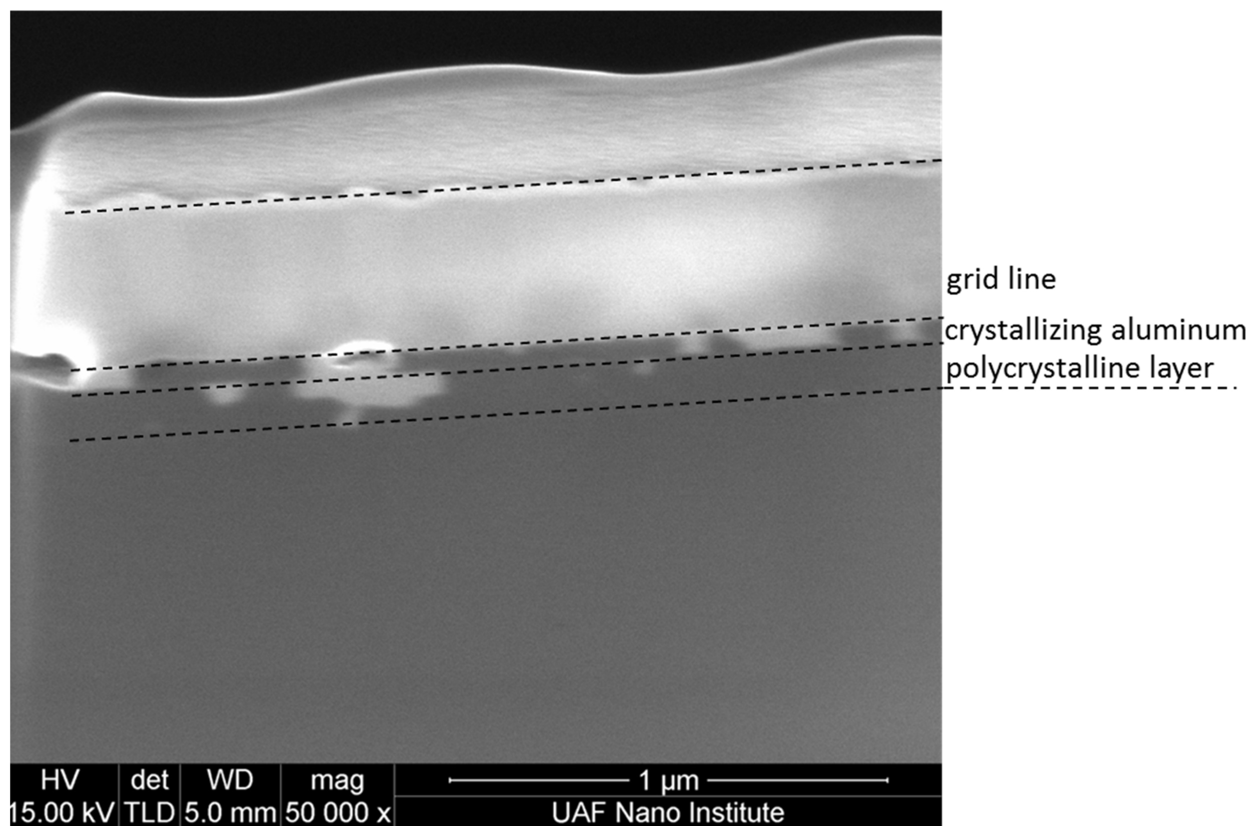

Figure 2.13 Cross-sectional SEM Image of highest efficiency TAIC emitter solar cell.

the junction has aluminum in direct contact with it. These shunt paths did not seem to decrease the shunt resistance of this sample as it was in the MΩ range. However, other solar cells with abundant layer exchange have displayed very severe shunt resistance degradation.

Figure 2.14 shows the top-view SEM of a similar high efficiency, mostly crystallized solar cell. The raised, flat portions are regions where silicon has crystallized within the aluminum layer. Figure 2.15 shows the TEM cross-sectional image of the FIB sample from Fig. 2.13. Selected area electron diffraction shows the polycrystalline aluminum grid (top), a single grain with twin defects in the polycrystalline emitter layer, and the single crystalline silicon substrate. This shows that the majority of the amorphous silicon did not exchange places with the aluminum layer and that most of it crystallized (97.92% crystallization fraction).

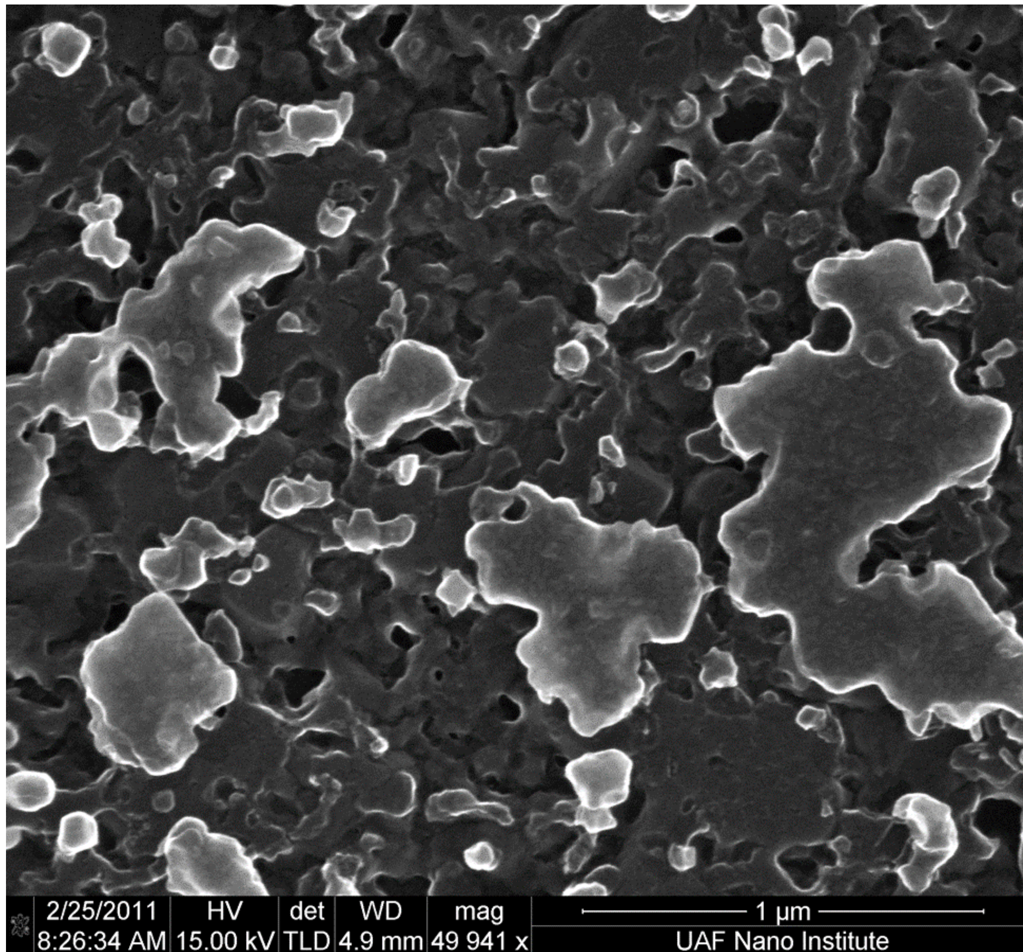

Figure 2.14 HRSEM image of the surface of an almost fully crystallized TAIC solar cell surface.

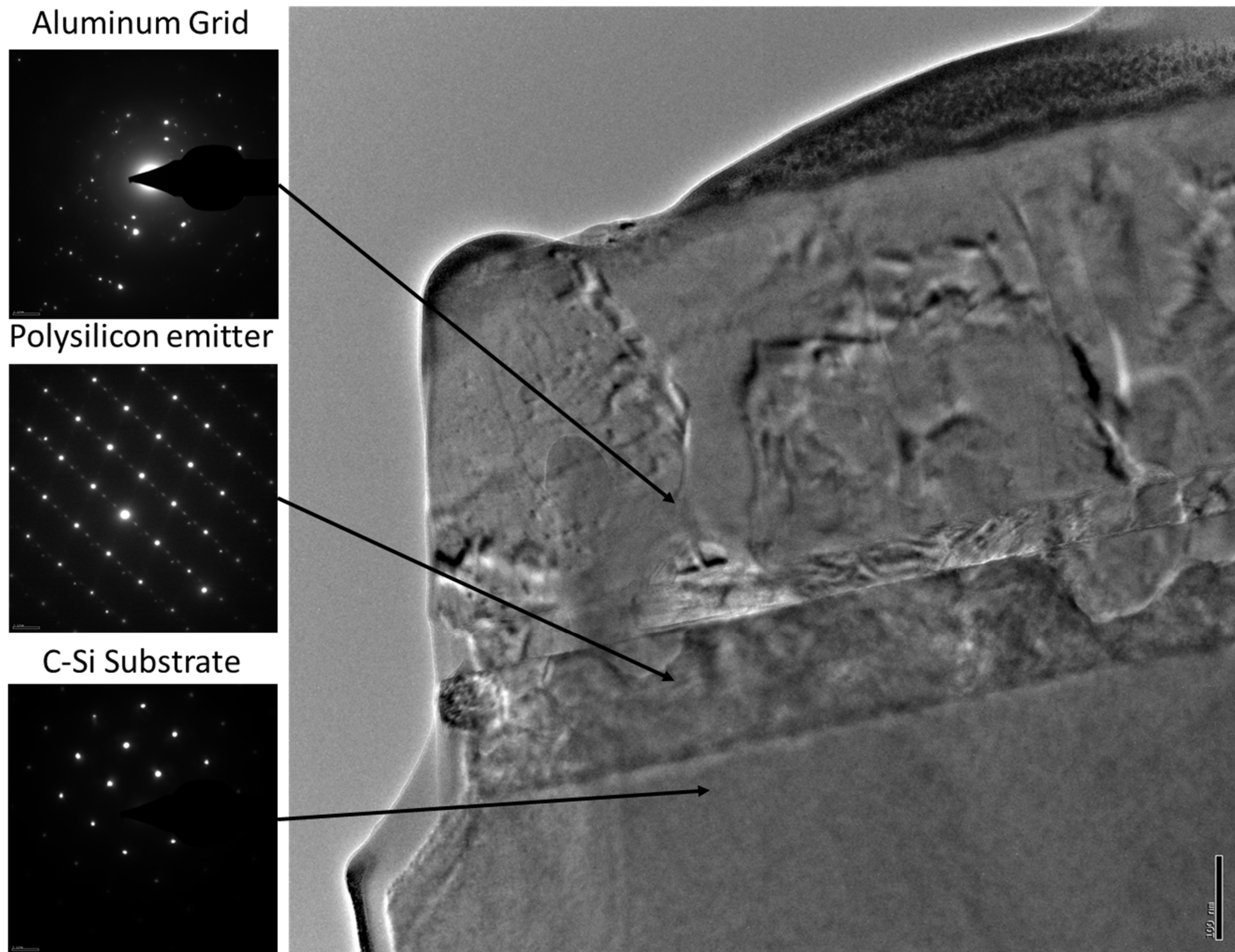

Figure 2.15 Cross-sectional TEM image and SAED patterns of TAIC emitter solar cell.

2.2: Partially Crystallized TAIC Solar Cells

Several causes exist which produce partially crystallized TAIC films. Limiting aluminum, minimizing time, and limiting temperature were determined. Other instances of minimal crystallization were observed without any obvious cause. All of these resulted in partial crystallization, higher Voc, lower Jsc, and lower fill factors compared to the most efficient cell. The increased Voc can be explained by excellent junction passivation by the uncrystallized hydrogenated amorphous silicon. The decrease in Jsc for these samples was due to increased absorption by hydrogenated amorphous silicon which is a parasitic absorber, because very few minority carriers generated here will be collected as useable electricity. Despite being forgiving

to the high sheet resistances of some crystalline silicon homojunctions that have been fabricated in this work, the concentrator grid design does have its limits, and fill factors may have been decreased because of the extremely high resistivity of these samples. Another possibility is that evaporated aluminum may have also had high contact resistivity to the partially crystallized, and almost certainly lightly doped, silicon material. Figure 2.16 shows the Raman spectrum of interest for a partially crystallized solar cell. This TAIC cell was heated for only 5 minutes, limiting the amount of crystallization.

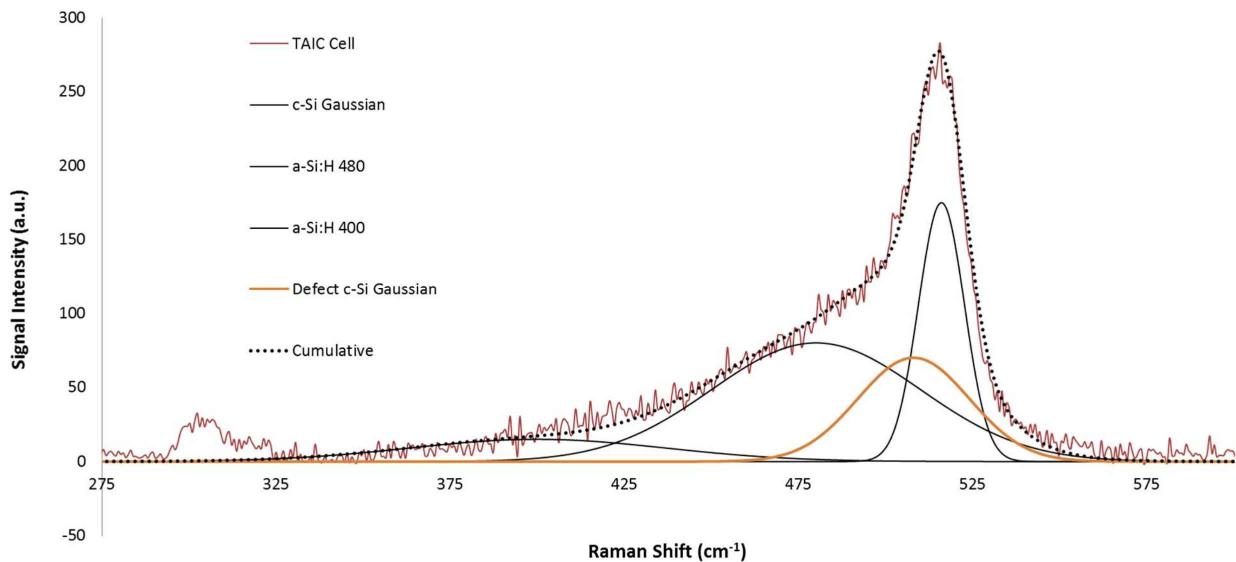

Figure 2.16 Raman spectrum of the emitter of a partially crystallized TAIC solar cell.

The crystallization fraction, as calculated from the methods described before, was 49.2%. As compared to the best solar cell's Raman spectrum, it can also be seen that there is a greater defect peak relative to the crystalline peak. This indicates that the amorphous silicon that is crystallizing first in the TAIC process may be more defective than from the sample that was fully crystallized. Figure 2.17 shows the quantum efficiency curves of this cell, along with the ideal curve and crystalline silicon reflection peak. The short wavelength response for these cells is

extremely poor. This is due to parasitic light absorption in the mixed-phase material which is only about 49.2% crystallized. Even when carriers are generated within the emitter, they quickly recombine in the low mobility material. The loss of short circuit current for these cells is not enough for the marginal Voc boost of partially crystallized samples like these. The Voc for these samples was around 550 mV initially and had dropped by 200 mV two years later, indicating an instability in the passivation quality of the emitter at the junction over time.

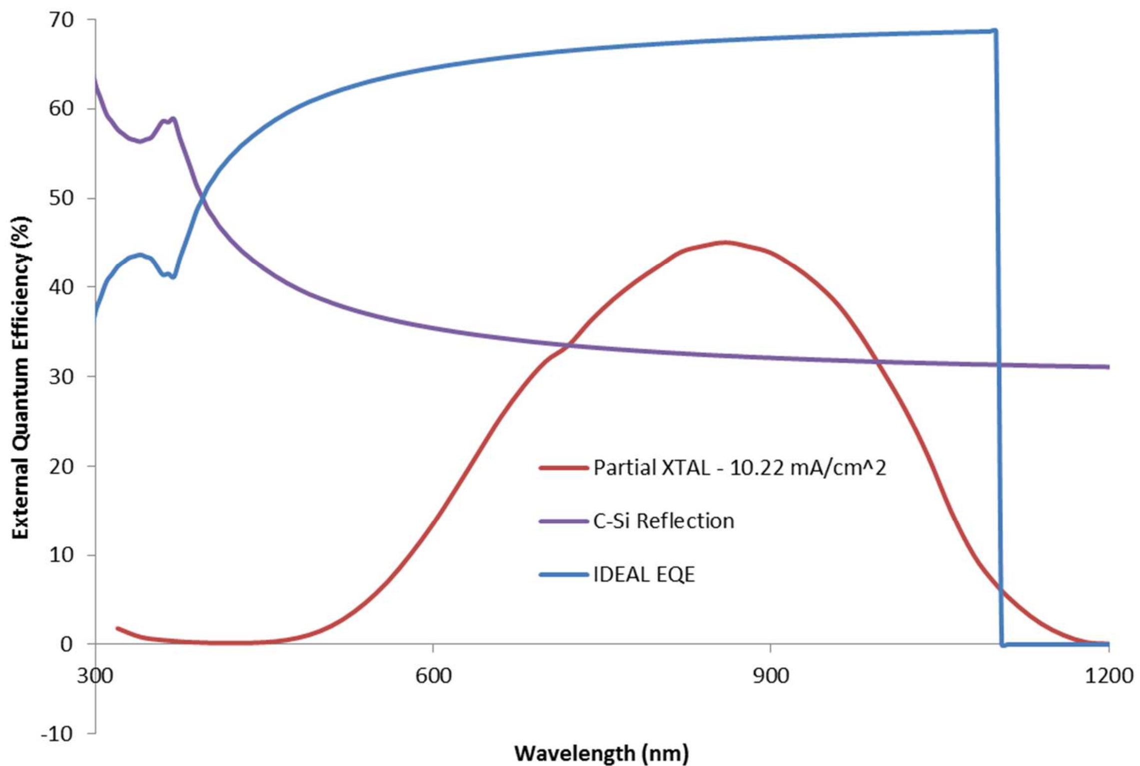

Figure 2.17 External quantum efficiency of a partially crystallized TAIC solar cell.

2.3: Layer Exchange TAIC Solar Cells

Anomalous cells with similar Voc compared to the highest efficiency cell and high detected crystallization fractions were observed. Upon further investigation these cells were found to have surfaces which were consistent with extensive layer exchange occurring over most of the surface. For these cells, amorphous silicon moved into the aluminum and crystallized in

plateau like shapes, limited in thickness to the thickness of aluminum. After etching aluminum, large voids were left, replaced by air. The low short circuit current densities for these types of cells can be understood from the problems of typical solar cells: surface recombination and light trapping. These cells are even worse than planar cells since there are multiple reflecting surfaces.

Figure 2.18 shows the Raman spectrum for these cells. The crystallization fraction of this particular sample was calculated as 95.6%. In addition to having slightly more amorphous material detected, this sample also shows a greater defect peak compared to the Raman spectrum from the best solar cell.

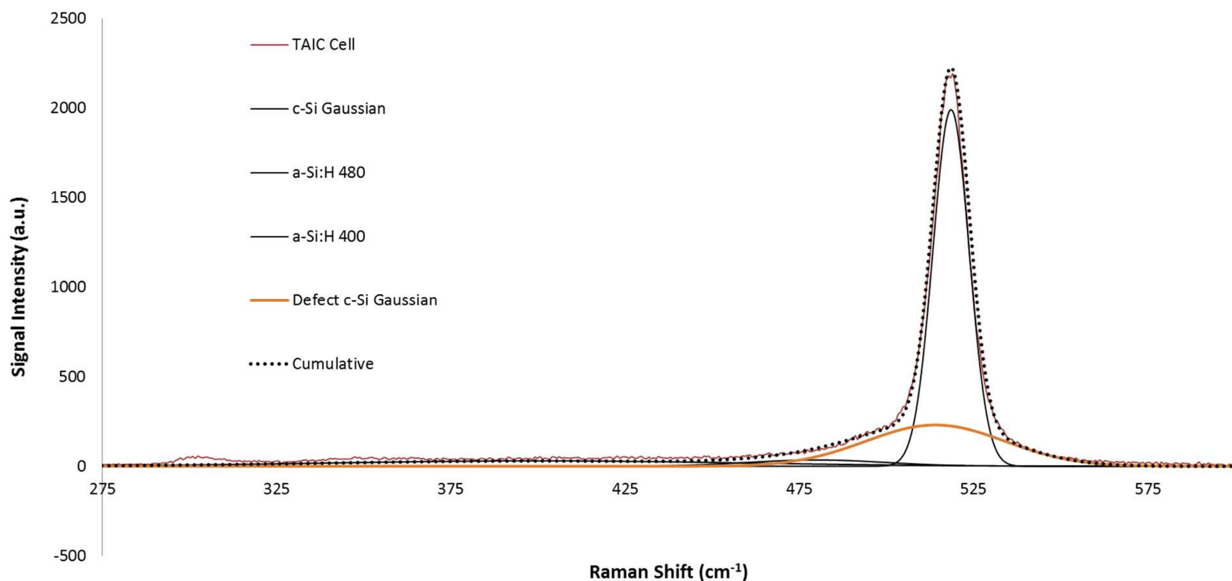

Figure 2.18 Raman spectrum from a layer-exchanged TAIC emitter solar cell.

Figure 2.19 shows the quantum efficiency curve for this cell as well as the reflection of crystalline silicon and the ideal quantum efficiency curve based on reflection of planar, single crystalline silicon. Like the partially crystallized samples, these layer exchanged cells have extremely poor short wavelength response. However, this characteristic cannot be explained by

excessive parasitic absorption due to amorphous material because this emitter is almost completely crystallized. However, the total short circuit current density of this cell was calculated as 10 mA/cm^2, which was even lower than that for the partially crystallized cell. Large portions of these emitters are effectively air/silicon/air/silicon interfaces. Additional detrimental characteristics is that these additional surfaces are unpassivated. It is well known that surface texturing, or increasing surface area, also increases surface recombination velocity. The combination of these two features eliminates quite a bit of the useable light entering the cell. These air/silicon/air/silicon interfaces are relatively planar as the top layer is dictated by the aluminum surface.

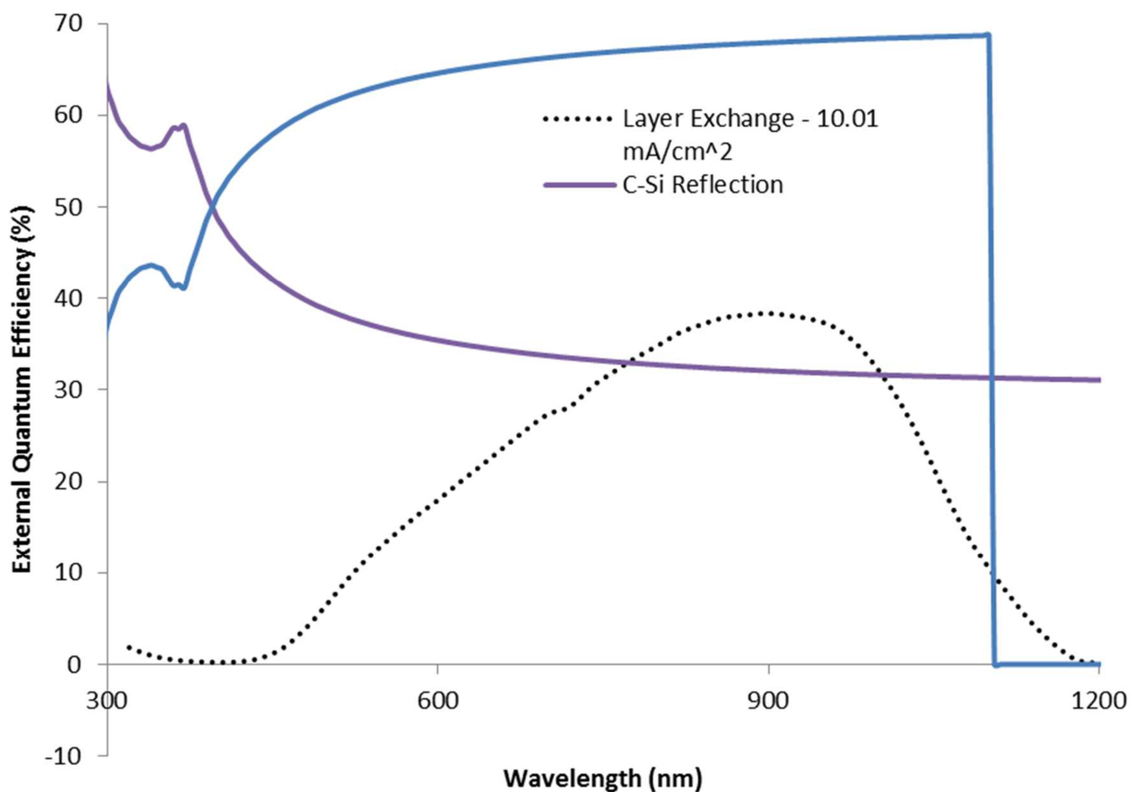

Figure 2.19 Quantum efficiency for a layer-exchanged TAIC emitter solar cell.

This additionally minimizes light scattering. For light that does enter the cell, the path length in this case is mostly limited to the thickness of the cell. Contrarily, textured surfaces

scatter light into the cell, increasing the path length of many photons, increasing the likelihood the photons will create charge carriers, and increasing the chances they will be converted to useable electricity.

The visual appearance of these cells is strikingly colorful. Typically neon green or pink will be seen which is likely determined by selective reflection based on the original thickness of the aluminum determining the thickness of both the top layer of silicon as well as the thickness of the air interfaces below the top "plateau" of crystalline silicon. This is a very similar process to crystallizing large grain polysilicon layers on glass, as described in Chapter 3. Like large grain polycrystalline films on glass, layer exchange on these emitters may have been promoted by excess formation of a native oxide layer.

Figure 2.20 shows an HR-SEM image of an emitter that was almost exclusively layer exchanged. The left image shows that the majority of the film does indeed have a relatively

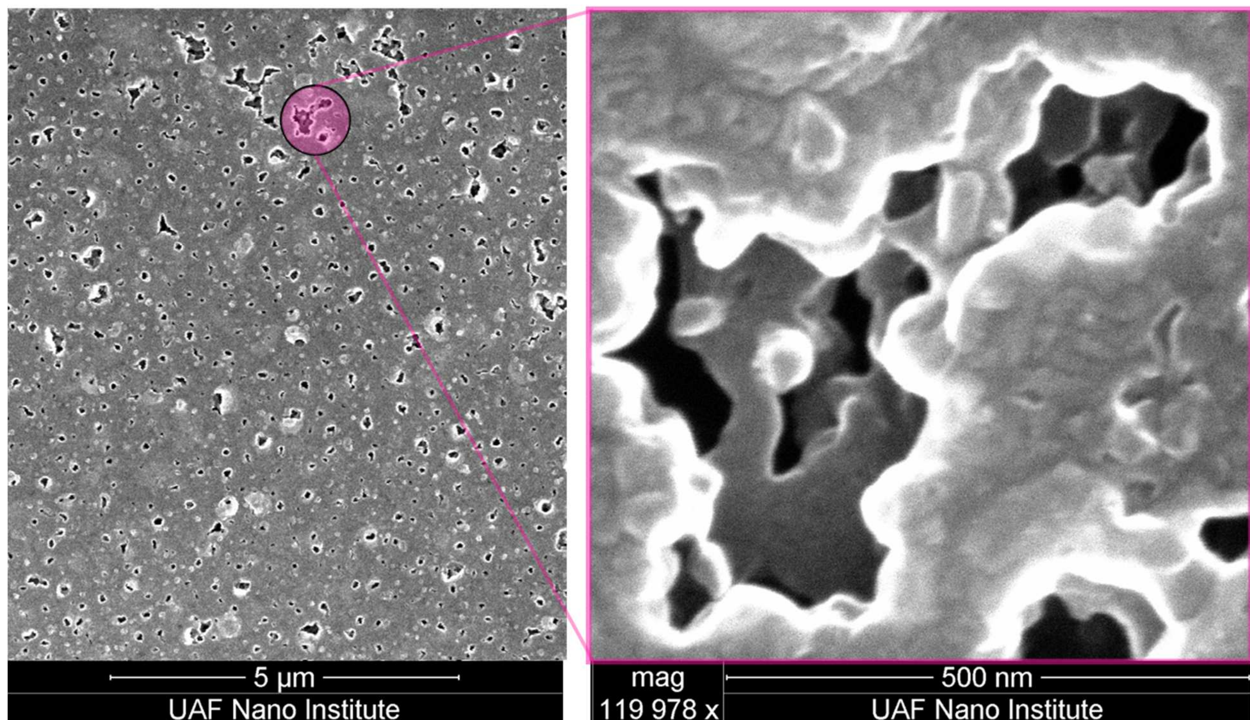

Figure 2.20 Surface view of mostly layer exchanged TAIC emitter.

planar surface with what appear to be 100-500 nm irregularly shaped holes spread evenly across the picture. Optically, these films are highly reflective and reflection is relatively non-diffuse. The highlighted area was magnified for a better view of the multi-layered structures that result from this type of crystallization. While the amorphous silicon moves into and crystallizes laterally in a planar fashion, resembling the original aluminum layer, how the rest of the crystallization occurs remains for speculation. One possibility is that the remaining amorphous silicon also enters the newly layer exchanged aluminum and crystallizes within it until most of the amorphous material has crystallized. Another possibility is that the aluminum diffuses into the amorphous silicon and crystallizes it without much movement from the amorphous silicon itself.

2.5: Effect of Rapid Thermal Annealing

A method of improving the open circuit voltage was developed for TAIC cells. High Voc samples showed less improvement, but samples with Voc below 400 mV could show improvements in excess of 100 mV when heated for five seconds at 475 ^oC. One possible cause for this improvement was the realease of hydrogen near the silicon/polycrystalline or amorphous silicon interface, passivating defects. Another possible reason is the activation of more aluminum acceptor impurities, thus increasing the potential for Voc. One partially crystallized sampling having undergone this treatment showed an increase from 550 mV to 600 mV.

2.6: Effects of Hydrogenation on TAIC Solar Cells

In an attempt to heal interfacial defects which likely are the dominant factor limiting Voc through increased reverse saturation current densities for these solar cells, a device with one of the lowest initial Jo values underwent catalytic hydrogenation (see Chapter 5 for chamber details). An interesting and seemingly contradictory result was observed. The reverse saturation

current decreased, signaling lower junction recombination. At the same time, the open-circuit voltage decreased and the ideality factor also decreased. Figure 2.21 shows the Dark J-V curves before and after hydrogenation and Light J-V characteristics are given in the table in the figure.

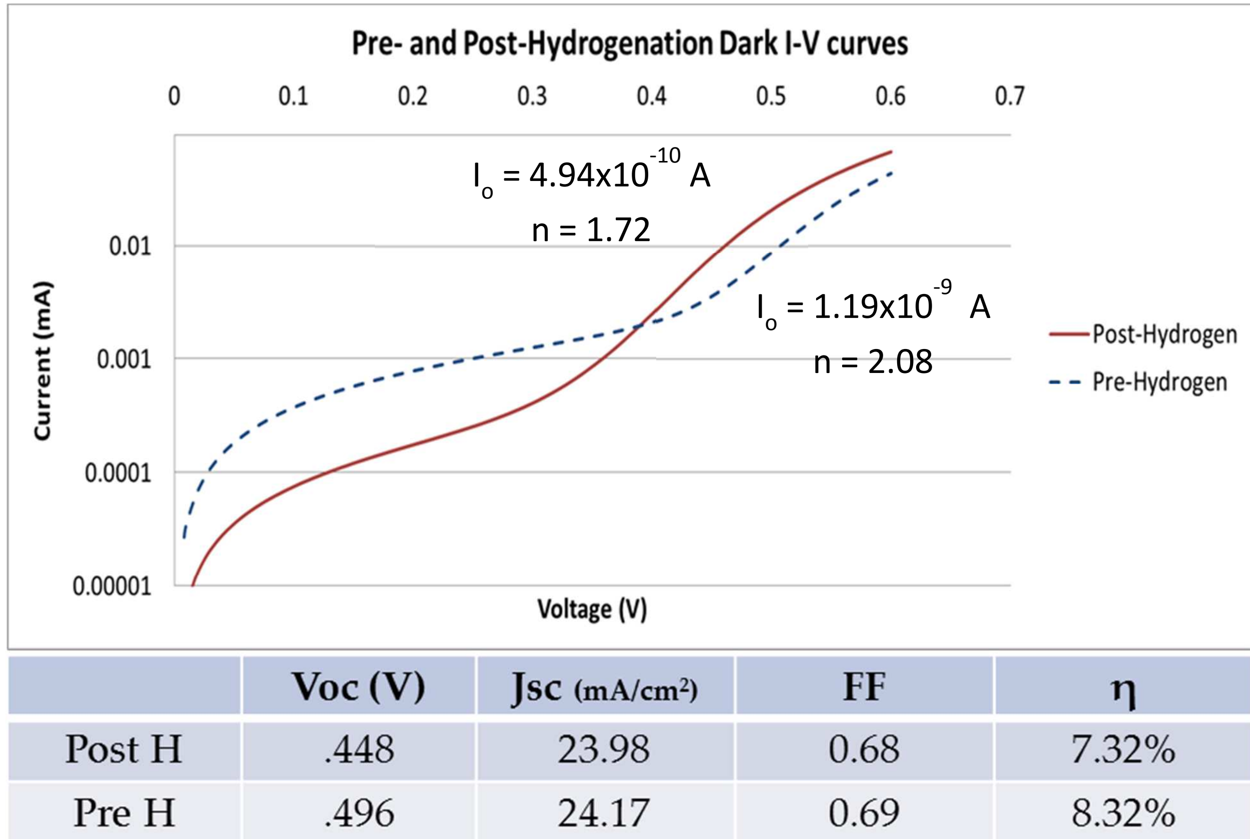

	Voc (V)	Jsc (mA/cm²)	FF	η
Post H	.448	23.98	0.68	7.32%
Pre H	.496	24.17	0.69	8.32%

Figure 2.21 Dark J-V curves and Light J-V characteristics before and after hydrogenation.

Several interactions are likely happening. 1) The TAIC emitters are lightly doped compared to standard solar cell emitters: $< 1 \times 10^{18}$ cm^{-3} versus $> 5 \times 10^{19}$ cm^{-3}. Ideally, Voc increases with decreasing reverse saturation current density. After hydrogenation, the reverse saturation current of this cell decreased, which would ideally result in a boost of efficiency. 2) The reverse saturation current is a recombination current. Hydrogen passivates dangling bond defects in silicon, and this is the likely cause for decreasing the reverse saturation current in this device. 3) Lightly doped emitters suffer from increased SRH recombination in the absence of

surface passivation. This has the effect of decreasing Voc and Jsc, both of which can be observed after the hydrogenation treatment. 4) Decreases in Voc lower the maximum possible fill factor, however these fill factors are within the measurement error.

The aluminum-hydrogen complex which inactivates the shallow acceptor energy level in silicon has weaker bond energy than that of hydrogen bonded to a dangling silicon bond. It is likely that hydrogen passivation of defects at the interface could be accomplished by hydrogenation followed by a low-temperature anneal below 350 ^{o}C. The solar cell was annealed at 350°C which reactivated the aluminum dopants. The Dark I-V curve did not fully recover to its initial state. The reverse saturation current and ideality factors were slightly lower than the pre-hydrogenation values. The Voc was 3 mV higher at 499 mV. Since the hydrogen inactivation of the aluminum acceptor impurity reactivates at around 150 ^{o}C, it might be possible to heal many of the dangling bond defects throughout the material, then restore the electrical activity of the dopants while avoiding losing the hydrogen passivation.

2.8: Effects of amorphous silicon quality on TAIC emitter solar cells

The influence of hydrogen content of PECVD a-Si:H on TAIC solar cell performance was also investigated. Fourier-Transform Infrared Spectroscopy (FTIR) has been used to determine the total bonded hydrogen content as well as relative amounts of Si-H and Si-H_2/clustered Si-H bonding; the latter is typically indicative of voids in the material and device quality a-Si:H has a minimum of this. It has not been experimentally determined whether device-quality a-Si:H is the ideal precursor to device-quality polycrystalline films for TAIC processing.

1”x1” SSP [100] 1-3 Ωcm n-type wafer die were cleaned with 1:1 H_2SO_4:(30%)H_2O_2 followed by a 10 second submersion into a 10% HF solution. The samples were dried with N_2 gas. 200 nm a-Si:H was deposited at 1.85 Å/s in an RF parallel plate reactor on 8 of the 1”x1” samples with 25% silane in helium at 30 mW/cm^2, a substrate temperature of 155 ^{o}C, a chamber pressure of 0.5 Torr, and a silane flow rate of 20 sccm. 200nm a-Si:H was deposited at 2.2 Å/s with the same processing conditions except that the precursor gas was 100% silane. Batches with 100% silane with substrate temperatures of 113°C and 250°C were also deposited at 3.47 Å/s and 2.36 Å/s, respectively. FTIR analysis was done following [2.50] on one double sided polished 1”x1” wafer from each deposition in order to determine atomic percentages of hydrogen as well as to calculate the microstructural parameter R for each deposition. A Nicolet 8700 FTIR was used for hydrogen measurement at a resolution of 6 cm^{-1} in air. Within 10 minutes after a-Si:H deposition, samples were transferred to an Edwards Auto 306 vacuum thermal evaporator. 1x10^{-5} mBar was reached before 50nm of high purity aluminum was evaporated at a rate of approximately 1nm/s. Samples were then annealed for 35 minutes each, including a 2 minute ramp time from room temperature to 350°C under 2x10^{-2} Torr vacuum for crystallization. After etching the aluminum, approximately 600 nm of aluminum was thermally evaporated on the front and back. Two metallization patterns were used, one with a shadow mask with and one photolithographically defined, one with approximately 16% grid coverage and the other with approximately 5% coverage. None of the reported cells incorporate surface passivation, BSF, or antireflection coatings.

Table 2.3 Si-H bonding properties of a-Si:H with varying deposition conditions.

	TOTAL H	SI-H	SI-H_2	R
Helium	8.81%	6.63%	1.01%	0.132
113C	14.56%	4.40%	10.66%	0.708
155C	8.92%	6.44%	2.35%	0.267
250C	6.26%	4.24%	0.51%	0.107

In agreement with reports in the literature for PECVD a-Si:H, increasing the substrate temperature was found to decrease total hydrogen content as well as the microstructure parameter, R (Table 2.3). The microstructure parameter is defined as [Si-H_2]/([Si-H_2]+[Si-H]). Atomic percentages of the total and different bonding configurations were calculated following [2.50]. The introduction of helium gas in a flow ratio of 3:1 to SiH_4 decreased R by a factor of 2 as compared to films prepared with pure silane at the same temperature and pressure.

Figure 2.22 shows the Gaussian fits for the 640cm^{-1} peak used to calculate the total hydrogen concentration in each of the sample sets. The integral of the Gaussian can be calculated and multiplied by a proportionality constant ($A = 2.1x10^{19}cm^{-2}$) to find the concentration of Si-H bonds regardless of bonding configuration. The Si-H and Si-H_2/clustered Si-H peaks are counfounded around 2000 cm^{-1} ($A = 9x10^{19}$ cm^{-2}) and 2090 cm^{-1} ($A = 2.21x10^{20}$ cm^{-2}), respectively, and required the superposition of Gaussian functions in order to separate their contributions from one another. Typically an R value of 0.1 is representative of device-quality a-Si:H. Only the helium and 250°C samples approach this microstructure. The 155°C pure SiH_4 sample has a significantly greater R value, indicating an increase in voids throughout the film. As expected, the 113°C sample, while having the highest total hydrogen content, also had the highest R value, indicating the worst quality film. However, it should not be assumed *a priori* that the best quality amorphous silicon leads to the best crystallization quality. In this paper, crystallization quality means that the emitter region formed through TAIC should be judged based on typical solar cell outputs: Voc, Jsc, and FF as determined by series and shunt resistances.

Figure 2.23 shows J-V curves for representative cells from each sample set. The results are so drastically different that some samples from each of the poor quality sets were processed

twice to ensure these problems were not caused by a processing error. The 113°C samples displayed extremely low shunt resistance, with the substrate acting almost as a simple resistor between the front and back contacts.

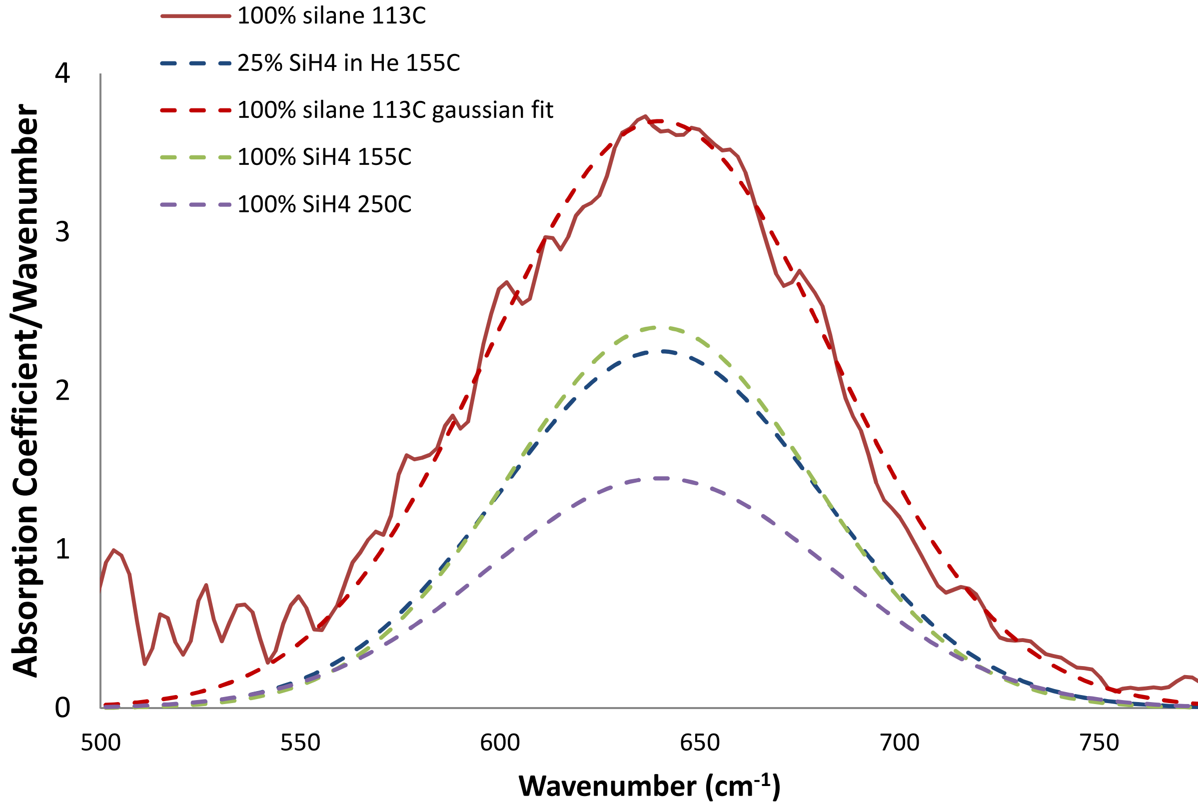

Figure 2.22 640cm^{-1} wavenumber Gaussian peaks.

To illustrate this, the resistance between the front and back of one of the cells from this set was 15Ω. In order for this to be possible with 1 Ohm-cm n-type silicon of 380µm thickness, the front and back contacts would only need an area of 2.5x10^{-3}cm^2. Since the grid coverage for this cell was 16% of a 4cm^2 total area, the resistive equivalent of 1.2% of the grid should be in direct contact with the substrate. The HRSEM image (see Fig. 2.24) for this sample reveals

structures covering approximately 16% of the film. It is possible that these structures are the surface feature of the shunting paths.

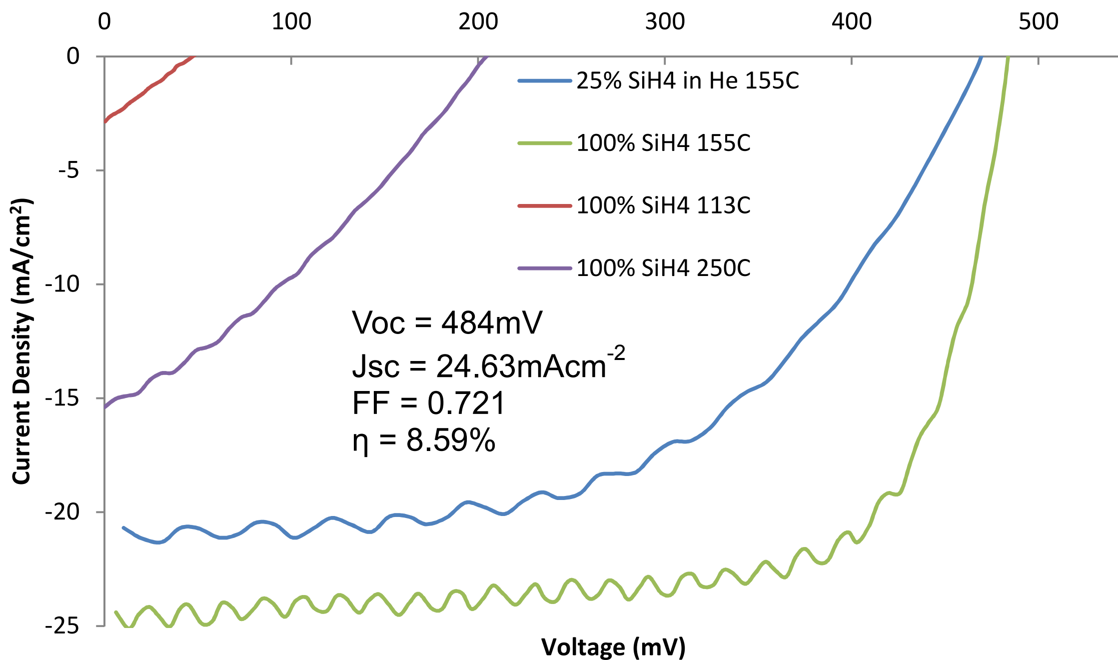

Figure 2.23 Example J-V curve under AM1.5 all film types.

Both the helium and 250°C samples, which have hydrogen content most closely matching device-quality amorphous silicon, did not give the best emitter properties. The shunt resistance measured for the helium sample was, like the 155°C pure SiH_4 sample, greater than 1MOhm. The series resistance as well as the lower Jsc value can be explained by the film only being partially crystallized. A significant amount of uncrystallized a-Si:H would lead to current loss as well as increased sheet resistance. However, the 250°C samples had major shunting like the 113°C samples. The best case from this experiment, by far, was the pure SiH_4 deposited film with a substrate temperature of 155°C even though the hydrogen bonding distribution of this film is not characteristic of device quality a-Si:H. Papadopoulos, *et al.*, reported an improvement of

29.9% in short circuit current density with the addition of a simple SiO_2 ARC [2.44]. The same consideration would give the 155°C sample from this experiment a Jsc of 32mA/cm^2 without additional texturing.

It is important to note that the RTA step only benefitted the 250°C samples by changing pre-metallization Voc from 0mV to between 100-280mV. The Helium and 155°C samples remained unchanged with 500-505mV before metallization, and the 113°C samples actually degraded due to the RTA from 400-482mV to 355-424mV. The RTA step was also performed on the helium FTIR sample with no loss of hydrogen. This is consistent with reports in the literature of the relative immobility of hydrogen in these films even at processing temperatures much higher than those used here.

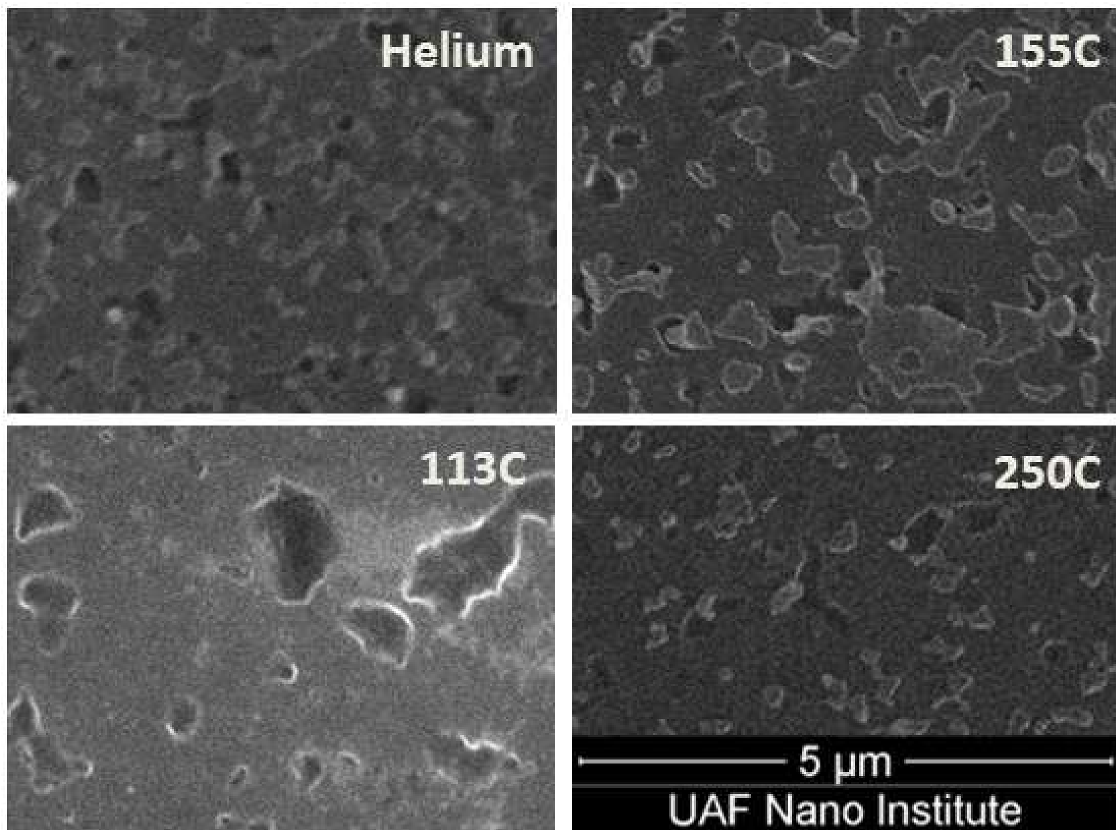

Figure 2.24 Surface view of TAIC emitters with distinct amorphous silicon.

Hossain, et al., found that increasing total bonded hydrogen concentration in sputtered a-Si:H decreased the crystallization initiation temperature [2.52]. These films were not demonstrated in a device and the majority of hydrogen bonded was in Si-H_2 and clustered monohydride groups, the opposite of hydrogen in device-quality amorphous silicon. At least some of these films were most likely layer inverted [2.38]. The samples most like sputtered films from this experiment were from the 113°C set. Partial layer inversion, in which silicon exchanges places in some areas with aluminum, would explain the low shunt resistance. Despite the relatively low values for the best of samples, low Voc is not inherent to the TAIC process and values exceeding 600mV have been obtained with different experimental procedures than described here.

TAIC has been performed with varying SiH_4 dilution as well as substrate temperature. Initial bonded hydrogen concentrations were measured with FTIR. The results indicate that hydrogen characteristic of device-quality a-Si:H is not necessarily optimal for crystallization with the TAIC process for the purpose of the emitter layer of silicon solar cells. Further work will be necessary to control the a-Si:H microstructure and its influence on the TAIC process.

The diffusion of aluminum into, the effusion of hydrogen from, as well as the crystallization of a-Si:H are the three causes for hydrogen loss during the TAIC process. The breaking of bonded hydrogen and its release changes the local and global microstructure of the amorphous network [2.51], either inhibiting or promoting TAIC or layer exchange mechanisms of crystallization. These factors also influence film stress which has been found to influence crystallization. To develop a full understanding of TAIC, the interplay between hydrogen and film stress and the resulting crystallization kinetics must be explored.

2.7: a-SiC:H Crystallization-Stop Layer

Another way to optimize these solar cells would be to have an interfacial layer with low light absorption and excellent surface passivation. This layer should also be resistant to crystallization at temperatures at which the TAIC process takes place. One such candidate material is hydrogenated amorphous silicon carbide. Carbon doping in amorphous silicon increases the material's band gap, thereby decreasing parasitic absorption characteristic of HIT cells. a-SiC:H has also been found to be capable of providing excellent surface passivation on silicon [2.53]. Aluminum induced crystallization of a-SiC:H has been reported in the literature at 600ºC [2.54], [2.55].

It has been reported that during the fabrication of HIT cells, even small pockets of interfacial epitaxy will drastically reduce Voc [2.56]. Were a-SiC:H incorporated into TAIC solar cells, it would be very important to be sure that no crystallization takes place at temperatures used for crystallization of a-Si:H. To do this, a-SiC:H was deposited in MPZ 2 with the following parameters: 5 sccm SiH_4, 25 sccm CH_4, 0.5 Torr, 3W, 155ºC substrate

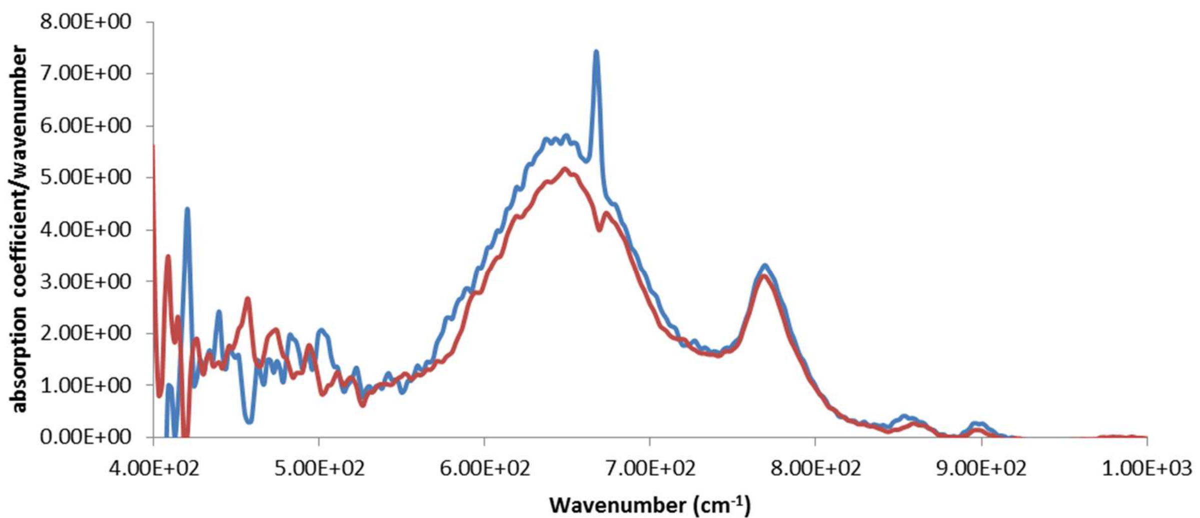

Figure 2.25 FTIR spectra of before and after annealing a-SiC:H

temperature. Figure 2.25 shows FTIR data of a-Si:C before and after a 400°C anneal with 50 nm aluminum. Figure 2.25 shows that a small amount of hydrogen has left the sample which is indicated by a decrease in the signal strength around 640 cm^{-1}. 400°C is 50°C higher than the temperature needed to begin driving out hydrogen from Si-H bonds. The decrease here is most likely indicative of that process, and not crystallization.

This temperature is above any used for creating any of the solar cells in this chapter. No visible change was observed in the film. After this, a solar cell was attempted with 30 nm a-SiC:H and 200 nm a-Si:H crystallized with 50 nm aluminum. The voltage was below 300 mV, indicating a poor interfacial quality between the a-SiC:H and the crystalline silicon. In order to prove this method, future work needs to include ensuring the passivation quality of the deposited a-SiC:H layer through lifetime testing.

2.8 Notable Anomalous Interactions

Some partially crystallized samples were not intentionally limited to partial crystallization through means of limited aluminum or limited crystallization time. One possibility is that the aluminum evaporation process for these samples was somehow the culprit. Reusing the tungsten boats with alloyed aluminum and tungsten is perhaps a cause. If, for some reason at least partial layer exchange is needed to initiate full crystallization, then the aluminum deposited on such samples may have inhibited layer exchange from taking place. Another possibility along these lines is that the rate of aluminum evaporation was high enough to cause sample heating and crystallization at the interface between aluminum and amorphous silicon. This may have inhibited further crystallization as well. Regardless, these incidents proved to be very interesting. Voltages in excess of 620 mV was achieved on such samples, indicating that some sort of p-i-n heterojunction was established. The temperatures at which this sample was

processed would be enough to release some hydrogen near the interface between amorphous and crystalline silicon, possibly healing defects that existed there from the plasma deposition of amorphous silicon while at the same time crystallizing a very small fraction of the amorphous silicon near the surface: calculated as 2.58% crystallization.

The Raman spectrum for this sample is shown in Fig. 2.26. While this sample may appear mostly amorphous, there is a slight hump on the 480 cm^{-1} peak centered around 518 cm^{-1}, which should be attributed to crystallized silicon in a strained, defective, or contaminated area.

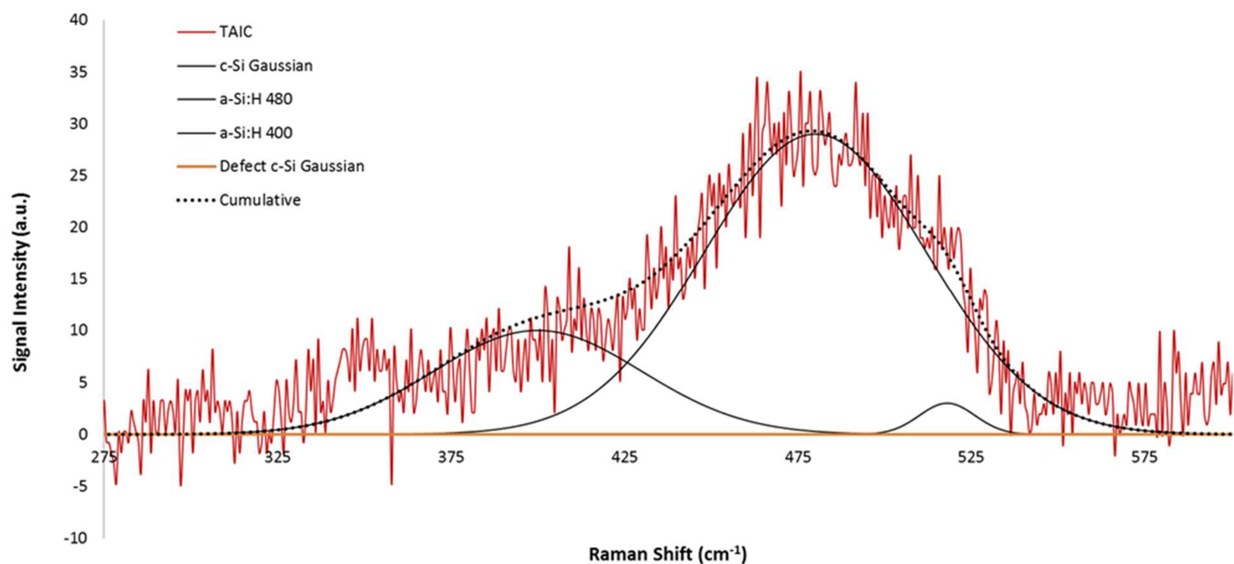

Figure 2.26 Raman spectrum of the TAIC sample with the highest Voc.

Unfortunately this sample was not large enough to process into a solar cell, but it certainly would have suffered from large parasitic absorption and low fill factors limiting its efficiency.

Quite a wide variety of partially crystallized samples were observed with various levels of crystallinity, microscopic, and macroscopic appearance. Macroscopically, the high voltage sample appeared unchanged compared to freshly deposited amorphous silicon. Samples could also appear milky to purple in color with layer exchanged texturing as well.

CHAPTER 3: TAIC SEED LAYERS ON GLASS FOR EPITAXIAL SOLAR CELLS

Thin-film silicon solar cells remain a promising technology to approach wafer-based efficiencies at thin-film costs. Epitaxial growth of silicon cells on seed layers has been a prominent approach with demonstrated efficiencies. However, cost-effective seed layers on glass or other low-cost substrates still remain one of the biggest road blocks to the success of this technology. Top-down aluminum induced crystallization (TAIC) has been developed to produce large-grain silicon seed layers on glass. Initial cells have been fabricated by Hot-Wire CVD at the National Renewable Energy Laboratory (NREL). The seed layers with grain-gaps show poor electrical characteristics comparable to reported cells grown on wafer templates with defect densities around $2x10^6$ cm^{-3}. New seed layers without grain gaps have been developed and are described here.

There are three main factors yet to come together to enable thin-film silicon solar cells: material quality, light trapping, and cheap substrates. The first two have been proven [3.1]-[3.2] and the third requires high-quality silicon seed layers. Researchers at NREL have achieved 630mV for epitaxial cells grown on "dead" wafers, in part due to high material quality and in part due to the incorporation of the HIT architecture [3.1]. A high fill factor of 78% was also reported [3.1]. CSG solar has achieved 29.5mA/cm^2 with solid-phase crystallized silicon of only 1.4µm [3.2]. This excellent value was achieved with textured glass, a white-resin back reflector, and back-contact to both base and emitter of the cell [3.2]. Were both technologies effectively combined, an efficiency of 14.5% would be feasible with a good seed layer. However, more work on seed layers will be necessary to achieve such a goal. This paper highlights initial work on large grain polysilicon seed layers created by top-down aluminum induced crystallization (TAIC) of amorphous silicon (a-Si:H) on glass.

Extensive research has been carried out on traditional aluminum induced layer exchange (ALILE). ALILE seed layers are prepared with a substrate/aluminum/a-Si configuration resulting in substrate/pc-Si/aluminum. The aluminum is etched away before epitaxial growth on the remaining polycrystalline grains. Solar cells with up to 8% efficiency with light trapping have been prepared at IMEC with CVD epitaxial growth on ALILE seed layers [3.3]. An independence of grain size on cell quality was later found to be inherent to the ALILE grains because of defect densities, $N_d \approx 10^9$ cm^{-3} [3.4].

Top-down aluminum induced crystallization begins with the opposite configuration; substrate/a-Si:H/aluminum and heat results in substrate/aluminum/pc-Si. This method has been used with low-temperature PECVD grown “microcrystalline” silicon to achieve cells of up to 5.2% efficiency [3.5]. The aluminum in this case is left to serve as a contact. In order to reach efficiencies well above this, defect density requirements warrant high quality epitaxy with seed layers that have low defect densities [3.6]. NREL has developed a relatively low-temperature (~760°C), high rate epitaxial deposition method using Hot-Wire CVD (1.8 μm/min) [3.7]. These temperatures being above the eutectic of aluminum and silicon (577°C) require that the aluminum in TAIC films be etched.

TAIC seed layers were prepared on Corning Eagle XG® glass. A-Si:H films of thickness 300 nm were deposited at 1.85 Å/s in an RF parallel plate reactor with 100% silane at 30mW/cm^2, a substrate temperature of 155°C, a chamber pressure of 0.5Torr, and a silane flow rate of 20sccm. The films were allowed to oxidize before sputtering aluminum. Samples were then annealed in vacuum for layer exchange to occur at temperatures above 450°C. These seed layers failed to fully grow together, leaving gaps between grains. However, they were sent to NREL for cell fabrication. Figure 1 shows the cell structure fabricated at NREL. Electrical

contacts were made by mesa etching the structure and contacting the n+ epi layer. N-type epitaxial layer was followed by a HIT architecture and an ITO transparent conducting oxide layer.

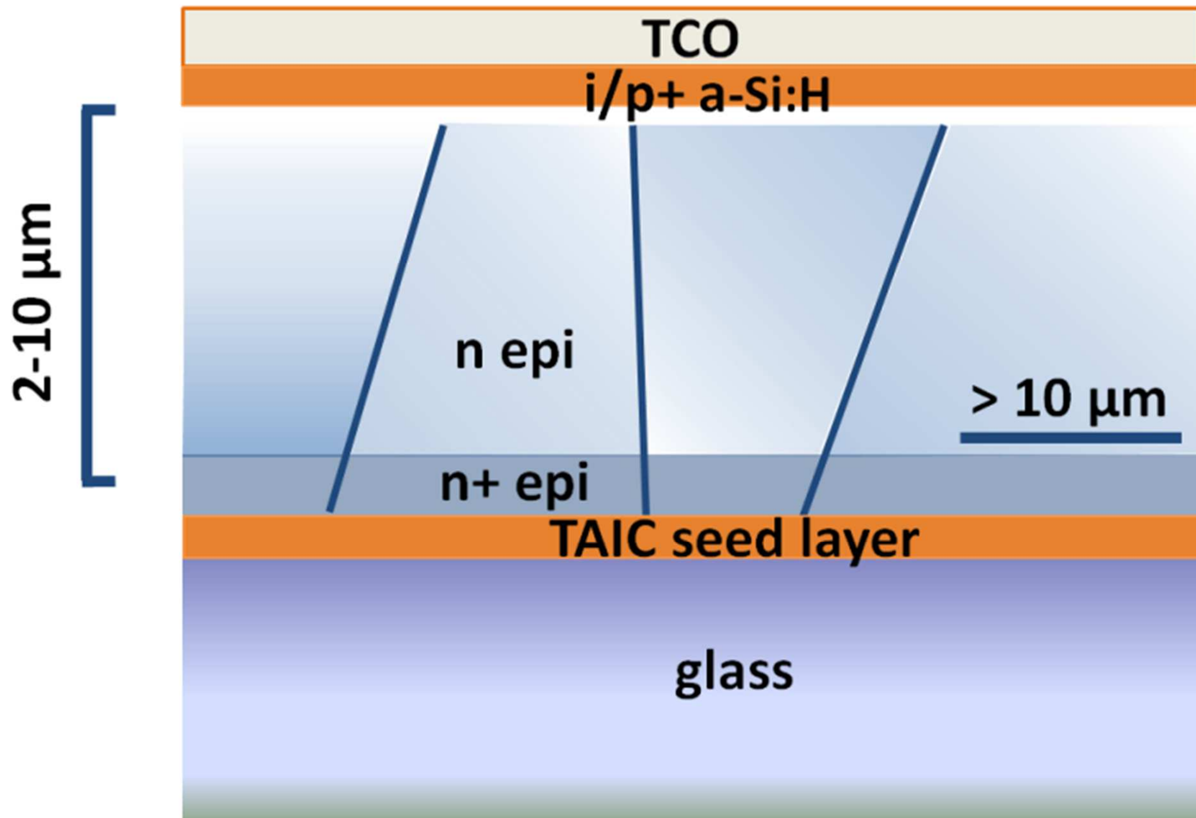

Figure 3.1 Cell architecture used by NREL.

Figure 3.2 shows grain structure of the preliminary TAIC seed layers. Electron Backscatter Diffraction shows grain boundaries and SEM revealed these boundaries to be gaps. The two grains outlined in red demonstrate that these grains can grow together.

Figure 3.3 shows the JV curve for the first device made on a TAIC seed layer. The device quality was poor, comparable to epitaxial cells grown on perfect wafer templates at temperatures of 660°C [3.8]. At these temperatures, oxygen was found to be the cause of increased threading dislocations which severely limit device quality [3.8].

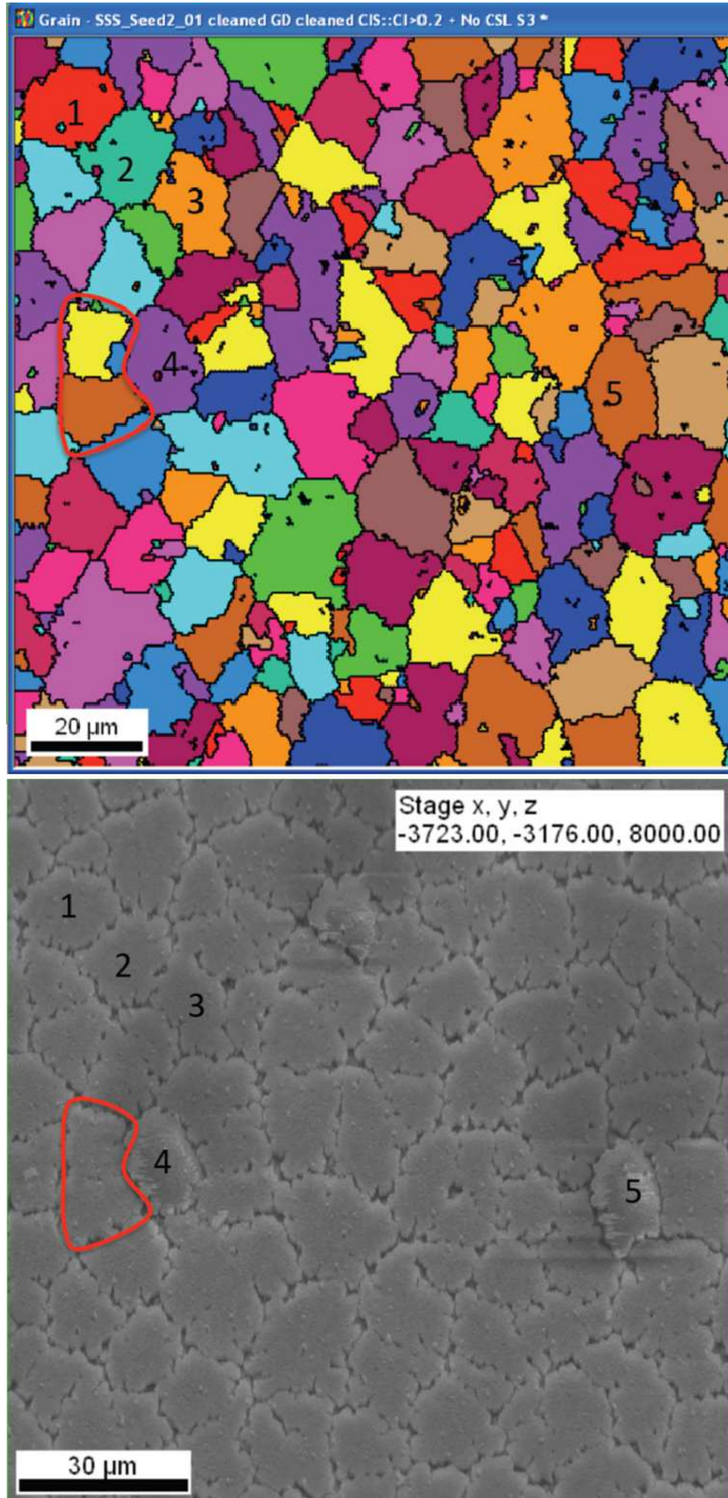

Figure 3.2 EBSD and SEM of TAIC large-grain polysilicon films on glass.

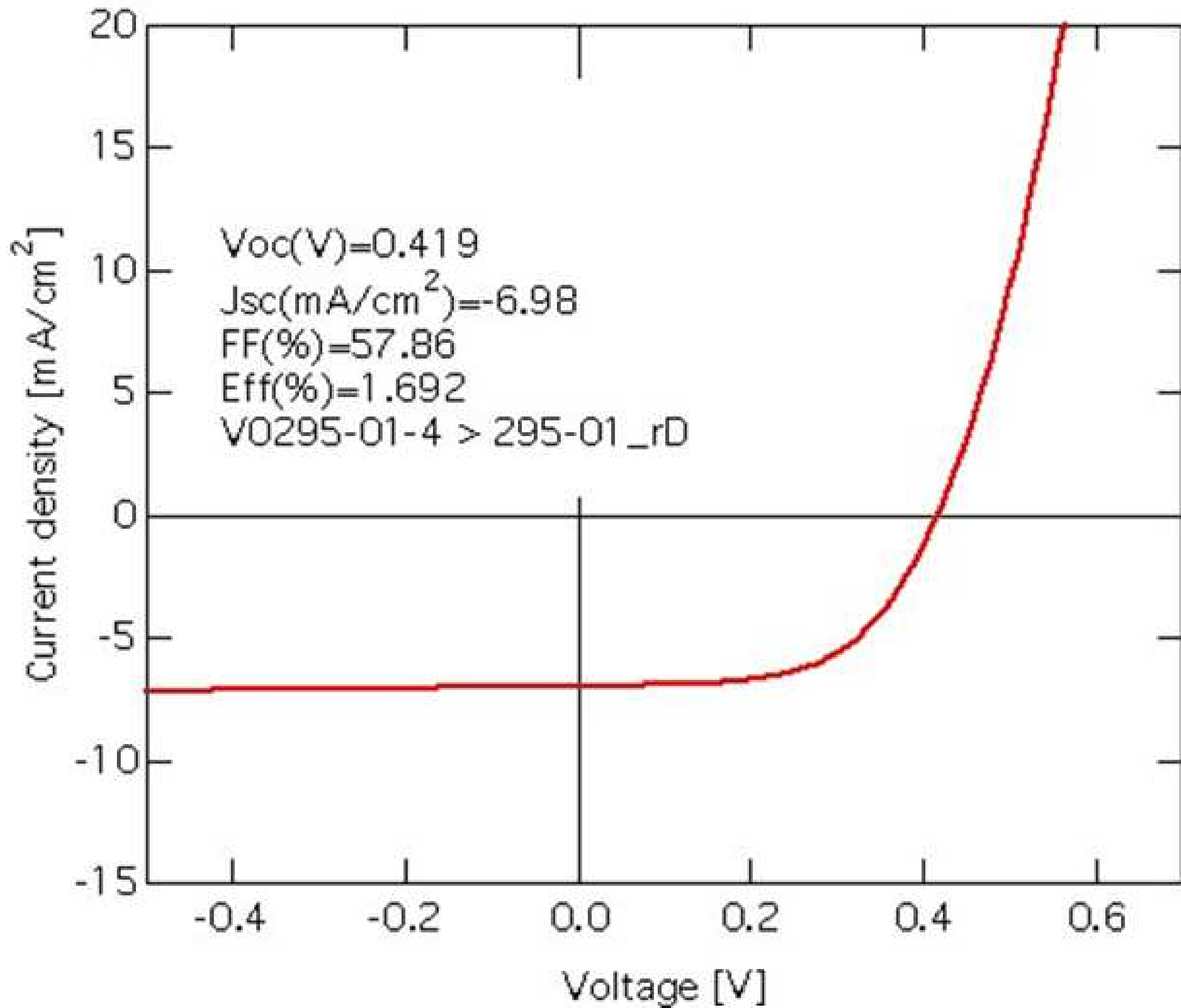

Figure 3.3 J-V curve for TAIC seed layers with grain gaps.

Table 3.1 compares this cell with similar cells grown on "dead" wafers with varying temperatures and consequently varying defect densities [3.8]. It can be seen that device characteristics were very similar to those cells grown at 660°C. Assuming that the grain gaps did not enhance the device, which should not be the case since epitaxy over these regions would be highly defective, then it is probable that the defect density of the TAIC grains was at most $2x10^6 cm^{-2}$. This is only four times higher than that required for high efficiency devices of this

thickness, and orders of magnitude lower than those inherent to seed layers produced by ALILE [3.6], [3.4].

Table 3.1 Comparison table of TAIC thin-film solar cell and NREL epitaxial solar cells on "dead" wafers.

Sample	TAIC	660°C	710°C	760°C
Voc (V)	0.42	0.43	0.51	0.57
Jsc (mA/cm^2)	6.98	6.9	14.6	15.37
FF (%)	57.9	63	68.3	72.5
Efficiency (%)	1.7	1.9	5.1	6.3
N_d (cm^{-2})	?	$2x10^6$	$5x10^5$	$1x10^5$

Since the first cell was made, TAIC seed layers with grains almost completely grown together have been produced. Small holes are left at grain boundaries where aluminum may be etched away. Hall mobility for films with grain gaps were found to be 13 cm^2/V-s while seed layers with fully grown grains were measured to be 42 cm^2/V-s. Aluminum was fully etched away, albeit more slowly due to the limited penetration beneath the grains. Aluminum was still be etched in less than fifteen minutes with even 0.2% grain gap density. As shown in Fig. 3.4, the edges have separate grains which, moving toward the center, change to fully grown films with sparse holes along grain boundaries. The non-uniformities are only related to lower deposition rates near the substrate holder edges and are a system limitation, not a process limitation. However, the edge grain size gives a good indication that, on average, the grains in the center will greatly surpass the 10 µm required for efficient devices [3.9]. This particular seed layer had an average grain diameter of 21.7 µm, however 200 µm grains have been achieved recently. The discolorations seen within the grains in Fig. 3.4 are sub-surface crystals. The structure has been verified by Transmission Electron Microscopy (TEM).

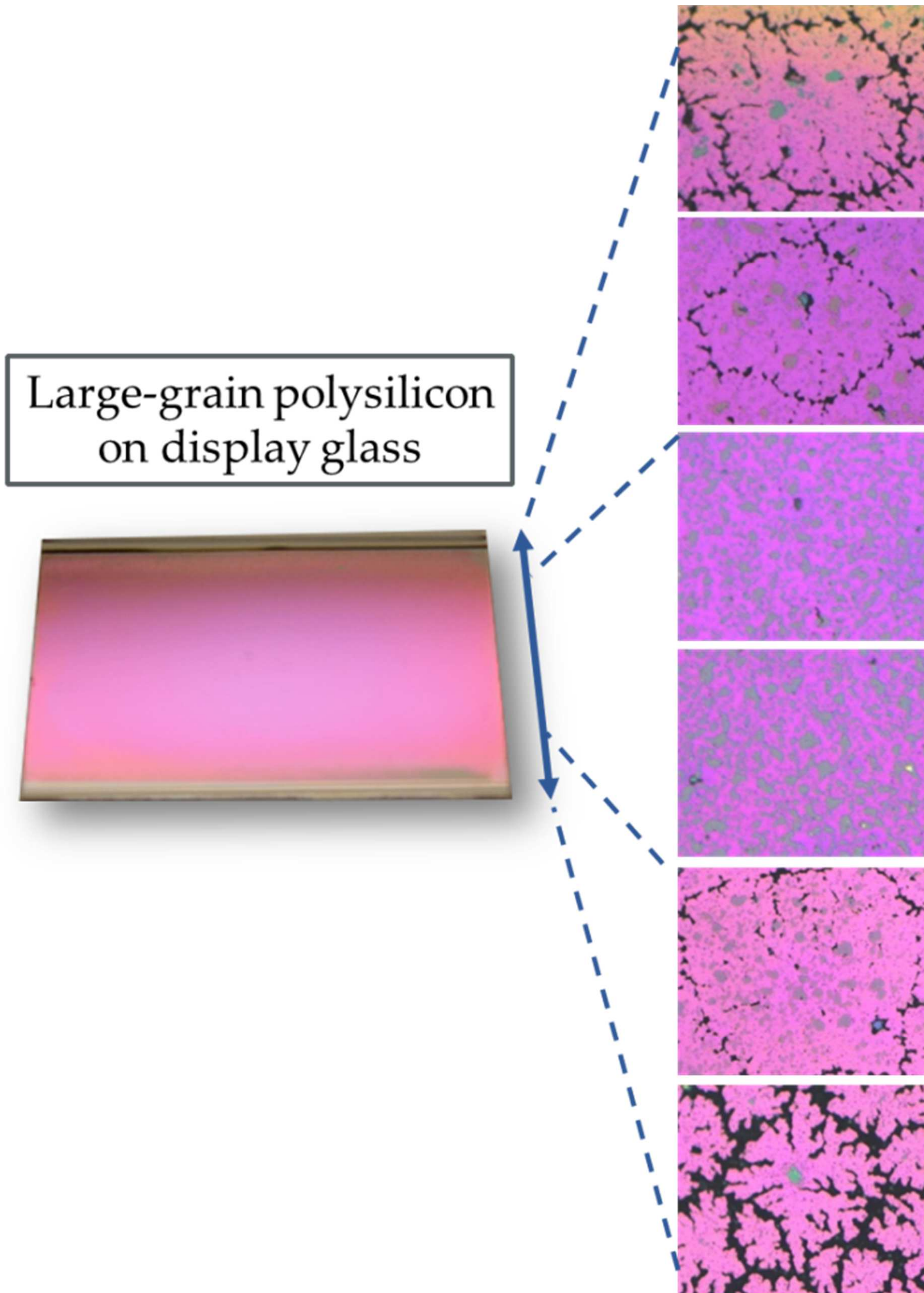

Figure 3.4 TAIC seed layer on glass with grain gaps present along edges.

Figure 3.5 shows a cross-sectional TEM image of the surface TAIC crystal attached to the display glass by a sub-surface crystal. The density of the sub-surface crystals depends on the ratio of aluminum to a-Si:H and also controls the adhesion of the film to the glass.

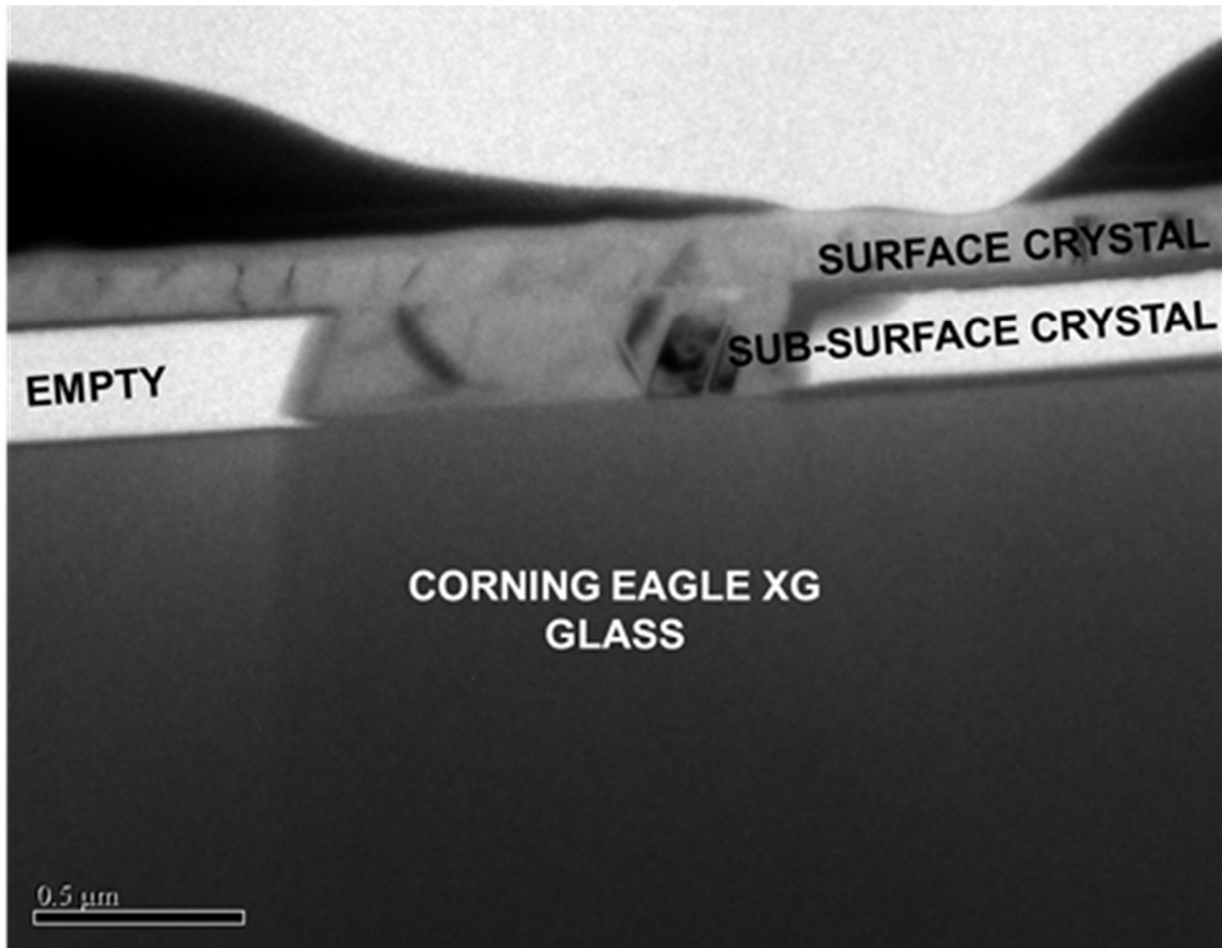

Figure 3.5 Cross sectional TEM of TAIC thin-film silicon on glass.

Figure 3.6 shows another TEM image upside-down with epitaxial silicon grown on top (below in image) the surface TAIC crystal. This image shows two things; First, the sub-surface crystal is not necessarily attached to the surface crystal at all places and second, the epitaxial silicon on TAIC seed layer has been achieved. A device was not made from this sample and future work will include device fabrication on these seed layers. Another technical consideration is whether or not these crystals may have bulk aluminum within them. Figure 3.7 shows EDS

done in an SEM from the back side of a TAIC film. The film was etched with 49% HF acid and then lifted off with carbon tape. Figure 3.7a shows a spot EDS going through both the sub-surface and surface crystals while the beam in Fig. 3.7b is only through the surface crystal.

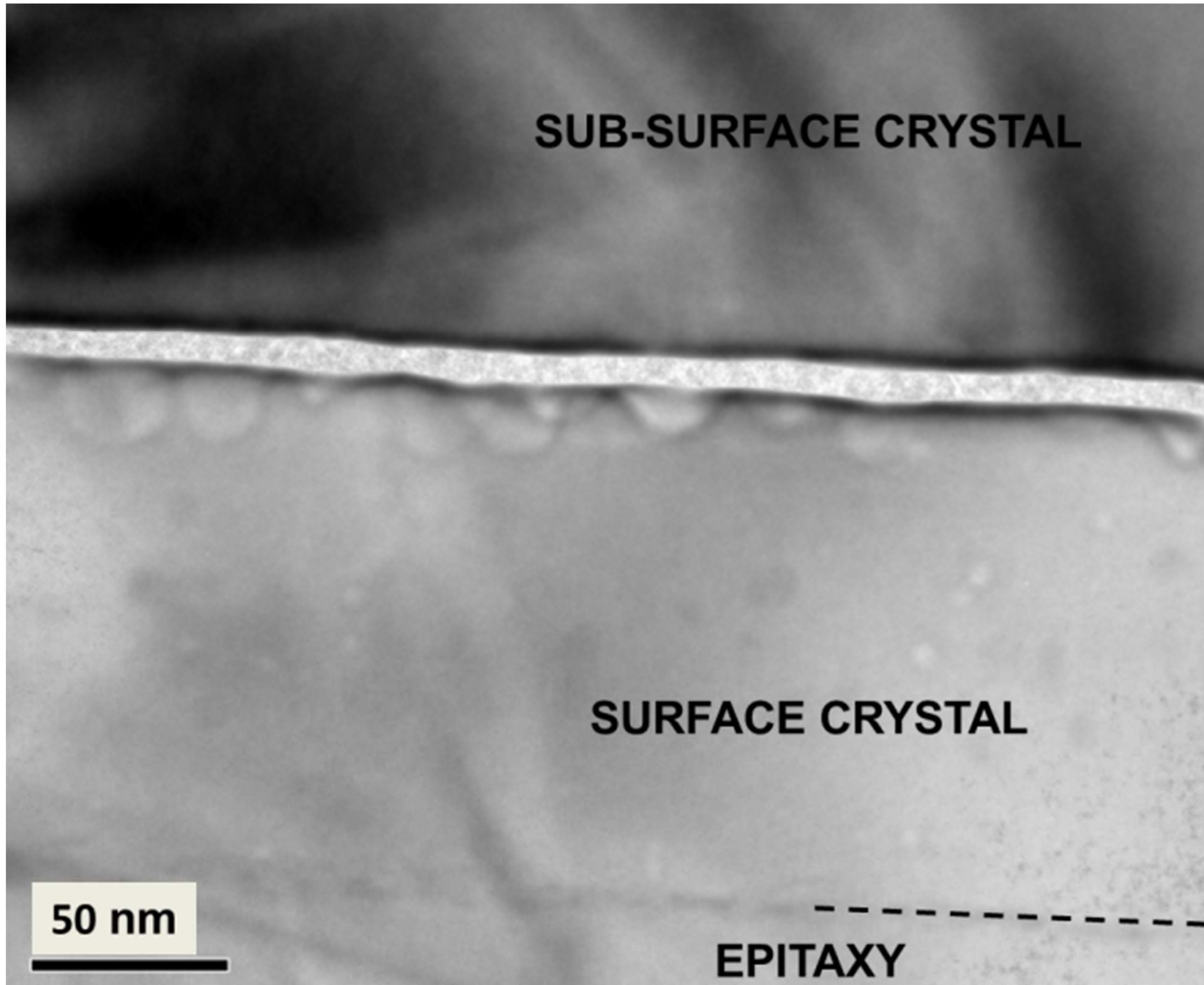

Figure 3.6 Cross sectional TEM image of epitaxial silicon on TAIC seed layer.

The measurement time was held constant for both. The EDS spectra in 3.7a has a higher peak count than 3.7b, and aluminum was not detected in appreciable quantities. The doping density typically measured for these films by the Hall measurement technique was found to be between 10^{18} cm^{-3} and $10^{19}cm^{-3}$.

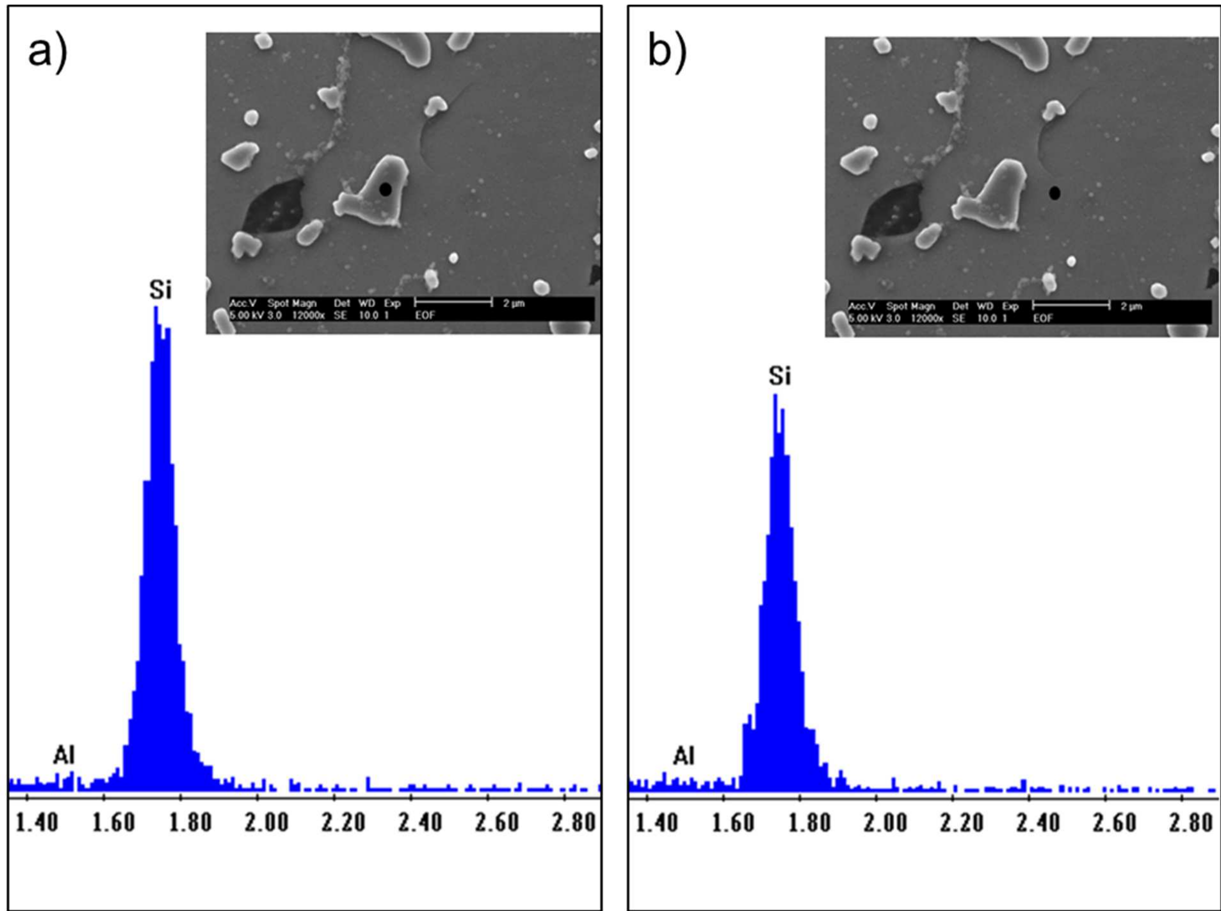

Figure 3.7 EDS scan of TAIC seed layer. a) Black dot in the SEM inset image shows the EDS spot on the subsurface crystal. b) The EDS spot is on the surface crystal only. The silicon peak is smaller in b), and the aluminum is not heavily present in either, indicating a simple thickness variation of primarily silicon.

In order to investigate the crystal quality of the seed layers without making a device, films were lifted off of the glass by exposure to 49% HF acid. The HF acid penetrated the surface of the film through the intergranular gaps and etched the glass beneath the sub-surface crystals. Entire films can be lifted off with this method and samples were prepared for plan-view TEM. Figure 3.8 shows an inter-grain gap. This was a section of film where two grains had not fully grown together. The SAED pattern on the bottom left shows multiple crystal orientations and this area includes a sub-surface and a surface crystal. The SAED pattern of the top-right

section indicates a single, twin-free crystalline region.

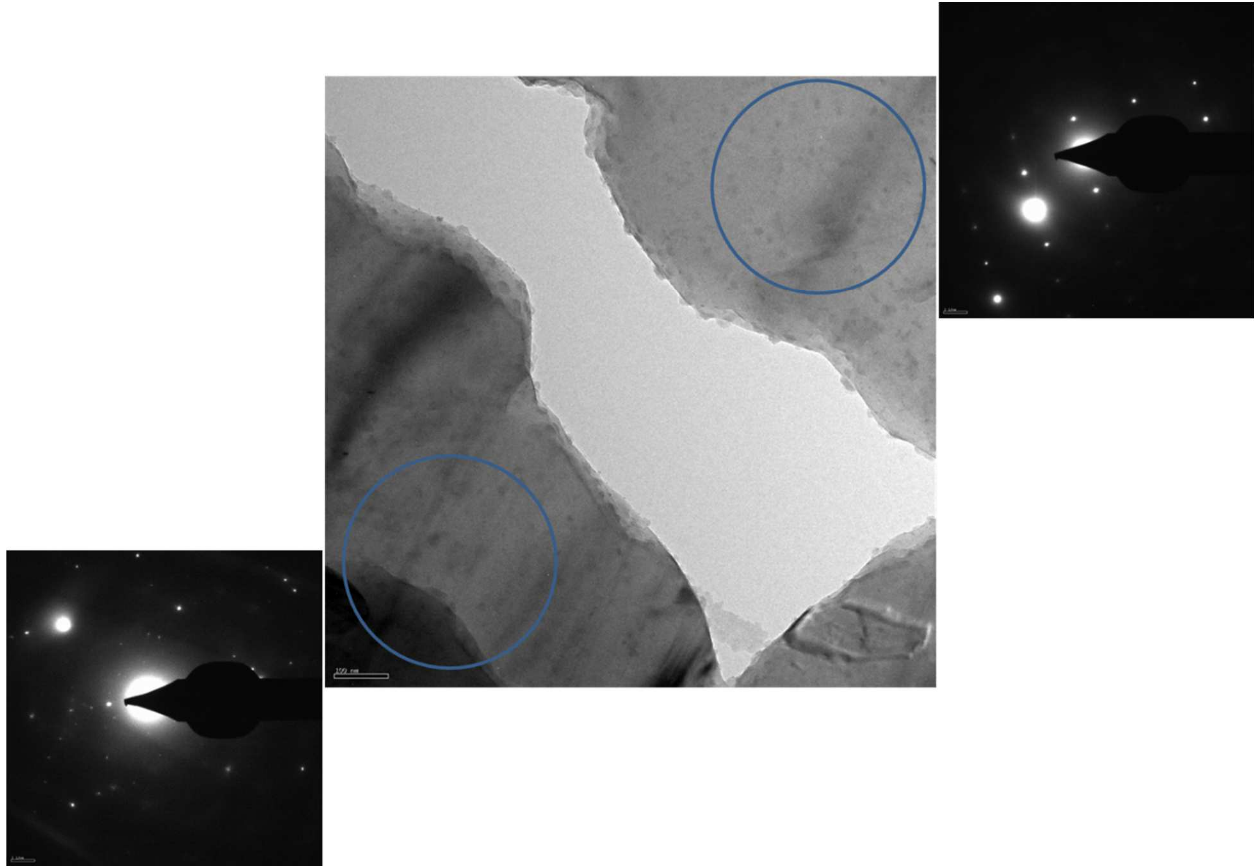

Figure 3.8 Plan-view TEM image and SAED patterns of a TAIC seed layer.

Large grain polycrystalline silicon seed layers on glass were successfully fabricated with the TAIC process. These were relatively low temperature (all processes below 450°C). While the structure literally seems to be the reverse of the traditional ALILE process, surface polishing is not necessary for this configuration since the excess crystalline silicon is all underneath the surface crystal. Another difference found for TAIC versus ALILE was that films could be intentionally peeled off due to the limited adhesion points present between the surface crystal and the glass substrate. The adhesion strength was found to be related to the density of subsurface crystals. Future work will include crystallization on various substrates as well as

fabricating solar cells epitaxially grown on TAIC seed layers with HWCVD. This chapter was based in large part on work previously published [3.10].

CHAPTER 4: HYDROGENATED SELECTIVE EMITTER

Most silicon solar cells in industry use heavily doped homogeneous emitters even though it has long been known that emitters have much lower surface recombination velocity (SRV) values with lighter surface doping. Low SRV leads to increases in Jsc, Voc, and FF. However, industrial screen printing paste has lower contact resistance when the underlying silicon is heavily doped. Selective emitters combine these two design features by having lower doping between grid lines and high doping below grid lines. There are several methods for achieving selectively doped emitters [4.1]-[4.4]. Extra process and control steps for several industrial selective emitters are shown in Fig. 4.1. Each of these selective emitters has at least two extra process steps and one extra process control necessary.

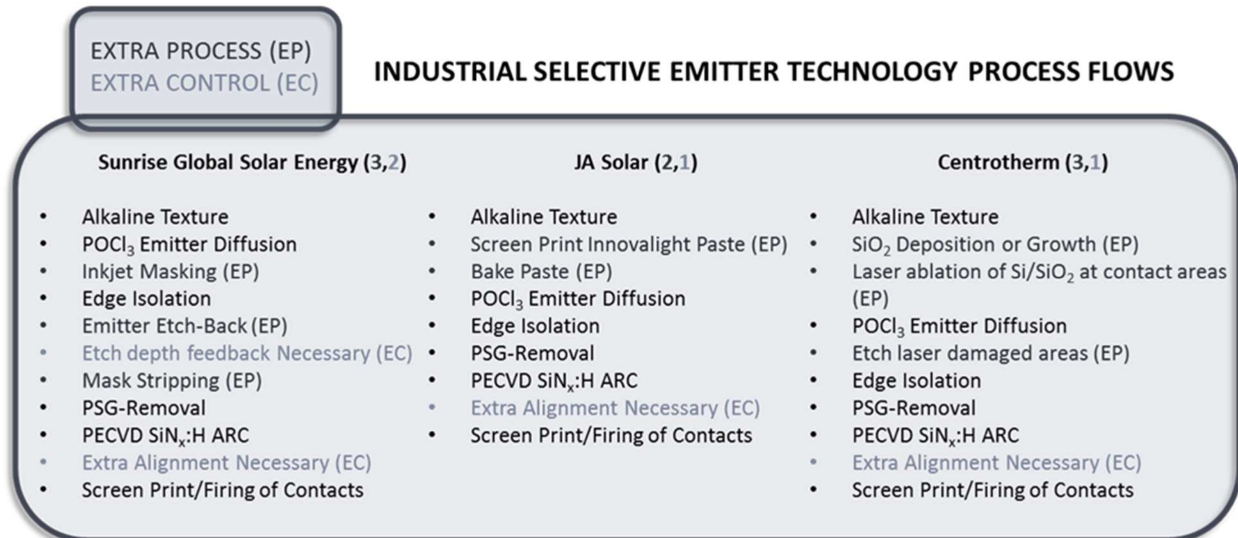

Figure 4.1 Process flows for solar cells and industrially relevant selective emitters.

One key trade-off with using selective emitters, however, is increased sheet resistance. Optimal emitter surface doping between the grid lines is much lower than what is currently used with modern selective emitters. This is because these SE techniques increase sheet resistance substantially. Increases in sheet resistance necessitate decreased grid spacing to minimize power

loss. For instance, JA Solar's selective emitter cells have 15% more gridlines than their homogeneous emitter cells. Assuming a spot-price for silver of $33/ounce, 100 µm grid line widths, and the 2012 usage of 0.25 g Ag/cell [1.3], a GW scale manufacturer using selective emitters would pay at least a $20,000,000/year penalty for extra shading loss and silver paste costs. This is probably why selective emitter technologies have seen little market penetration.

An ideal selective emitter would have low surface doping while retaining low sheet resistance by using a single self-aligning step. One way to possibly achieve this is through hydrogenation of boron-diffused emitters. The method of hydrogenating a boron emitter may answer the fundamental question of whether SRV's dependence on surface doping concentration is due to the physical presence of boron atoms or its electrical activity.

SRV has been found experimentally to increase with increasing doping for both phosphorus and boron diffused emitters [4.5]. Figure 4.2 shows a graph of this relationship for

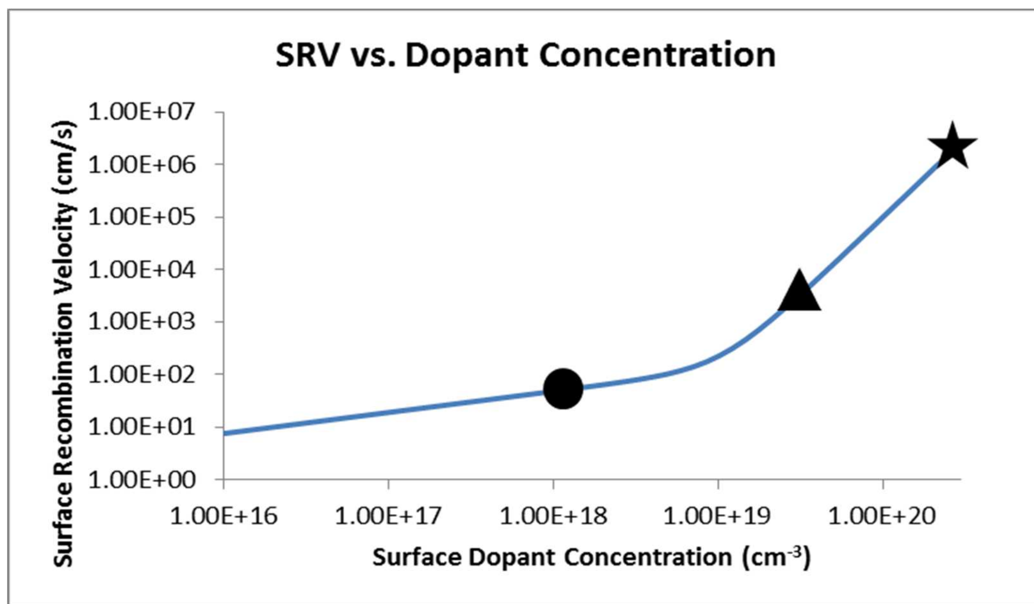

Figure 4.2 Surface recombination velocity vs. surface dopant concentration [4.6]. The star shows the SRV of a highly doped, homogeneous emitter. The triangle shows the SRV of a typical selective emitter. The circle shows the possible SRV of a hydrogenated emitter with 99% inactivation of surface dopants.

phosphorus doped silicon surfaces passivated with silicon nitride [4.6]. The shapes, from left to right, represent possible SRV values for the hydrogenated selective emitter (HSE), a standard selective emitter, and a highly doped homogeneous emitter. These values are incorporated into the emitter modeling software EDNA as a user-defined parameter. EDNA was used to investigate performance changes of homogeneous emitters under various atomic hydrogen treatments [4.7].

4.1 Hydrogen Inactivation of Acceptor Impurities in Silicon

Atomic hydrogen was originally thought to simply bind to a silicon atom to fill the hole. However, more detailed molecular cluster modeling revealed that the hydrogen atom actually binds in an interstitial site along the (111) direction behind the boron atom (Fig. 4.3) [4.8]. This positioning removes the acceptor impurity level from the band-gap, thus neutralizing the electrical activity normally provided by a substitutional boron atom.

Diffusion of hydrogen in boron doped silicon is trap-limited, considering the boron

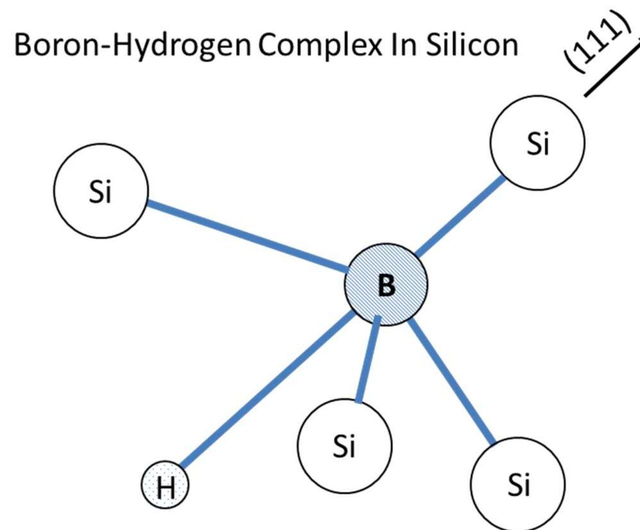

Figure 4.3 Anti-bonding location of the boron-hydrogen complex in crystalline silicon.

impurities as traps for hydrogen. The diffusion coefficient given by Eq. 4.1 has been fitted experimentally by Herrero, *et al.* [4.9],

$$D = D_0 \exp\left[-\frac{E_M}{kT}\right] \quad (4.1)$$

where D is the trap-free diffusion coefficient, $D_0 = 2.4\times10^{-7}$ cm^{2}s^{-1}, and $E_M = 0.43$eV is the activation energy. In the presence of traps, hydrogen diffusion is slowed following eq. 4.2,

$$D_{eff} = \frac{D}{\left[1 + r[B]\exp\left[\frac{E_B}{kT}\right]\right]} \quad (4.2)$$

where D_{eff} is the trap-limited diffusion coefficient, D is the trap-free diffusion coefficient, $r = 1.35\times10^{-27}$ is a factor related to the hydrogen flux density at the surface, [B] is the concentration of boron impurities, and $E_B = 0.6$ eV is the activation energy of hydrogen diffusion in trap-rich silicon. Following these equations, diffusivities of hydrogen can change depending on the concentration of boron impurities present given all other equivalent conditions. According to Herrero, *et al.*, temperature and initial boron concentration are the only two factors limiting D_{eff}.

Figure 4.4 shows that the trap-limited case is only effective for hydrogenation temperatures of less than 250°C independent of dopant concentration. While characterizing the hydrogenation chamber built into MPZ 5, TAIC samples hydrogenated from 100°C with doping densities on the order of 4×10^{17} cm^{-3} to 9.5×10^{17} cm^{-3}. From Fig. 13, the substrate temperatures used and the doping density of the films hydrogenated yield little difference in the effective diffusion coefficients. Therefore, trap-limited diffusion effects most likely did not have a significant effect on aluminum inactivation for these samples. It is important to note that this model was fitted to experimental data determined by detecting decreased free hole concentration through infrared reflection and is not actually representative of the diffusion coefficient of

hydrogen in silicon or the concentration, necessarily. Molecular dynamics studies have indicated that B-H complexes can attract up to 10 other atomic H in energetically favorable positions which confirms experimental evidence of detecting unbounded hydrogen in concentrations six to eight times that of boron impurities [4.10].

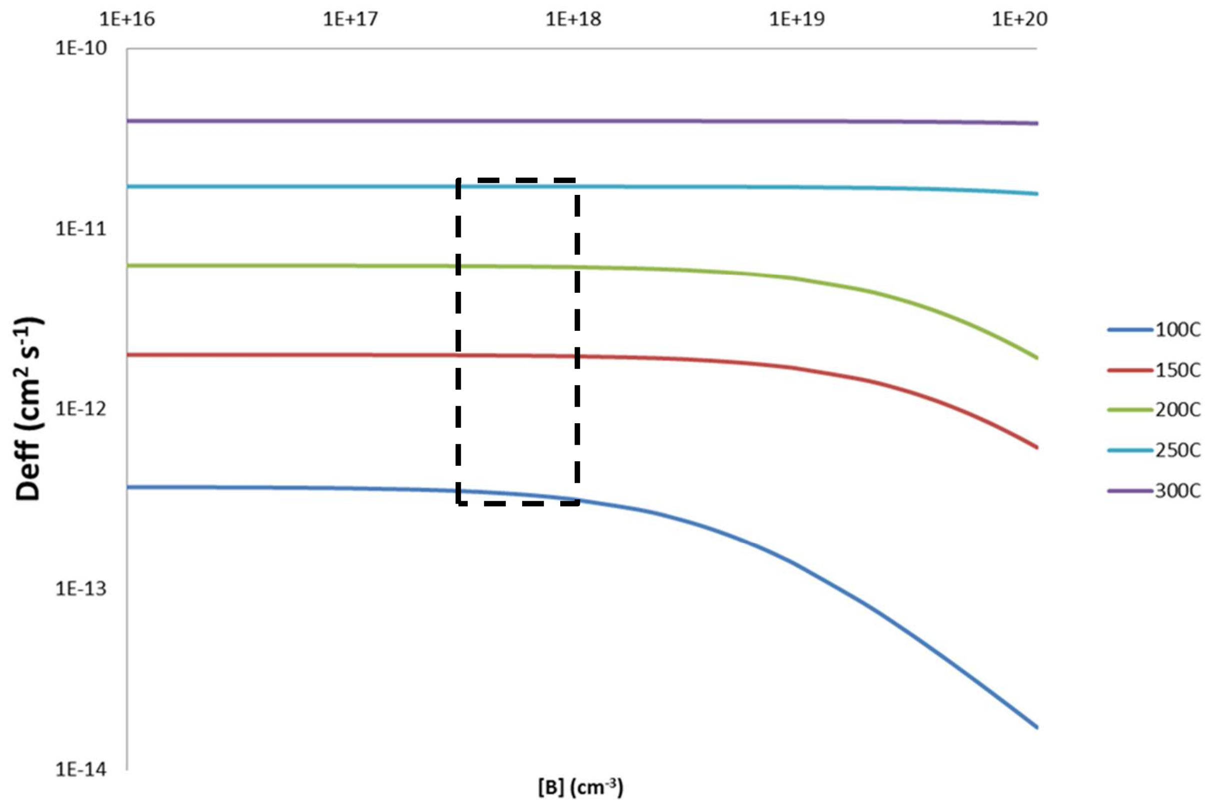

Figure 4.4 Trap-limited diffusion coefficients of hydrogen in boron-doped silicon. Curves for sample temperatures from 300°C (top) to 100°C (bottom) are shown. Dashed line shows values for TAIC sample hydrogenation processing ranges.

There are several key physical features which determine the applicability of hydrogenation to selective emitter formation. 1) Atomic hydrogen should only affect the doping near the surface and not appreciably increase sheet resistance. 2) Atomic hydrogen must affect only the areas between grid lines and must be blocked by silver. 3) Atomic hydrogen must penetrate antireflection and passivation coatings. 4) The performance enhancement must last for 25 years under operating conditions.

4.2 Boron-Hydrogen complex profile in silicon

The boron-hydrogen complex profile has been determined experimentally for highly boron doped monocrystalline silicon substrates [4.9]. In that study, researchers used remote hydrogen plasma to expose the bare silicon to atomic hydrogen. Using infrared reflection measurements, they were able to measure the difference in free-carrier absorption and calculate the profile of the boron-hydrogen complexes for various hydrogenation times. The 30 minute hydrogenation profile was very interesting and is shown in Fig. 4.5. It was apparent that, if this profile was applied to the areas between grid lines of a solar cell, an ideal selective emitter could

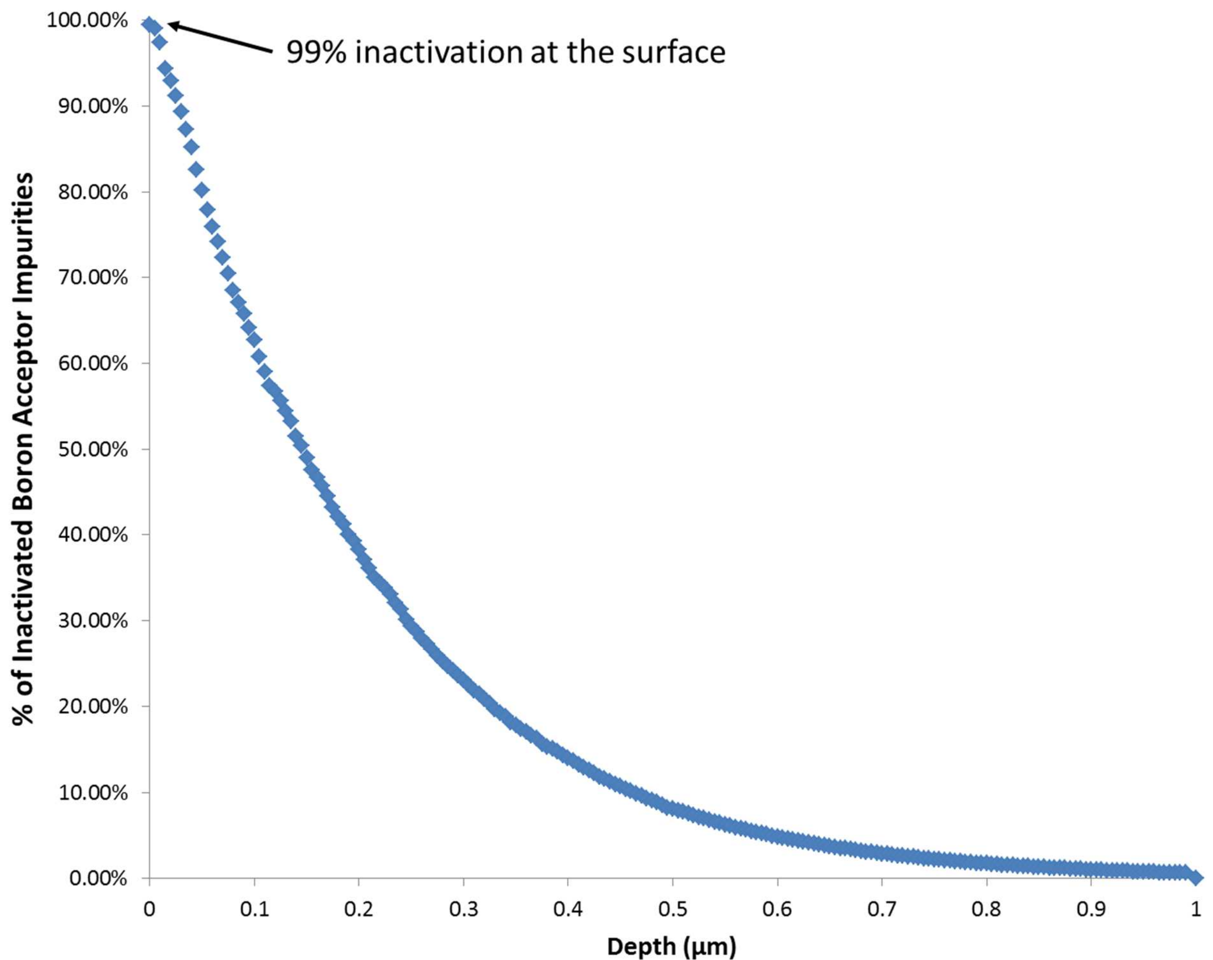

Figure 4.5 Percentage of electrically inactivated boron acceptor impurities after 30 minute hydrogenation on 1 x 10^{20} cm^{-3} boron-doped silicon. Electrical activity returns to 100% after 1 µm [4.9].

be formed. Figure 4.6 shows this data applied to a 500 nm Gaussian diffusion profile to estimate the modified profile after hydrogenation. The sheet resistance of the profile changes from 33 Ω/□ to 97 Ω/□. An estimated five minute hydrogenation would only increase the sheet resistance to 38 Ω/□. This could be a very significant achievement as surface recombination velocities might be reduced greatly with only a marginal increase in sheet resistance, and therefore no additional silver grid lines would be required. From experimental data [4.9] it seems likely to achieve an emitter profile which satisfies light active doping at the surface returning to heavier doping, and then the normal reduction toward the p-n junction.

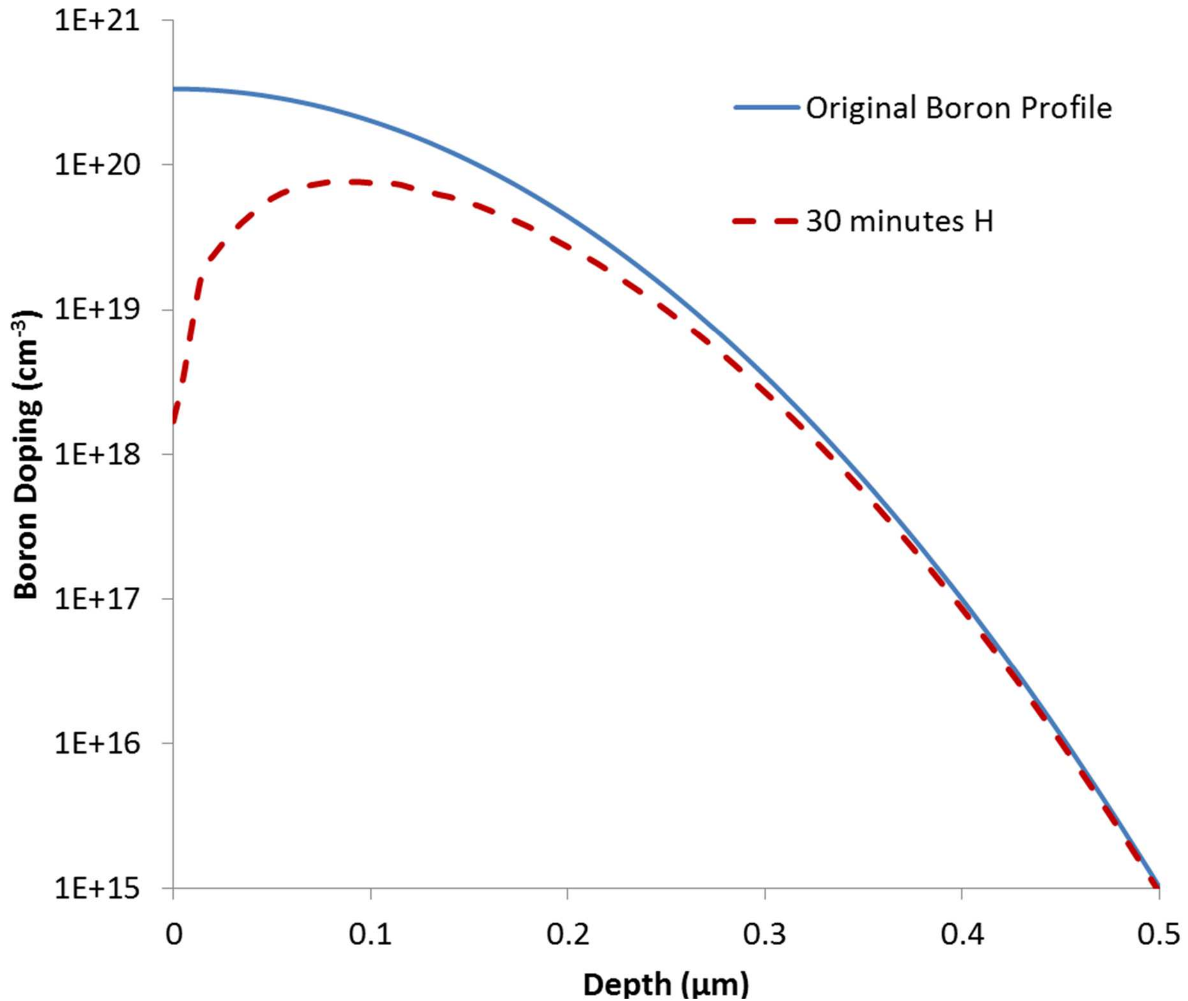

Figure 4.6 Modified boron profile extracted from experimental data [4.9]. The benefits of this profile as applied to a selective emitter solar cell were simulated in EDNA.

This is in contrast to traditional selective emitters where the surface doping is the highest at the surface, requiring higher surface concentration than this approach in order to maintain reasonable sheet resistance values (< 100 Ω/□).

4.3 Hydrogenation Apparatus and Efficacy Experiments

There are several ways to generate atomic hydrogen. Plasma of hydrogen gas or other hydrogen containing gases such as ammonia, pressurized and atmospheric boiling water, and catalytic filament methods have all been used to hydrogenate semiconductor materials and/or inactivate acceptor impurities [4.9], [4.11], [4.12]. Atomic hydrogen can inactivate the electrical activity of dangling bonds, point defects, acceptor impurities, and donor impurities in silicon [4.8]. Under certain circumstances, atomic hydrogen has also been found to etch silicon [4.13].

Figure 4.7 shows an annealing chamber on the cluster tool used for amorphous silicon depositions was modified to double as a catalytic filament hydrogenation chamber. Hydrogen gas enters the chamber from the ¼" VCR connection in the bottom 8" CF flange. A tungsten filament enters through the same side of the chamber via a 2.75" CF flange. The tungsten filament hovers a few centimeters above the gas inlet. Gas pressure is controlled remotely through the MPZ 2 chamber's turbomolecular pump and throttle valve. The tungsten filament is resistively heated by passing current through it. Filament temperature increases with current and a 0.05" diameter tungsten wire will be heated to 1900°C with 13.75 Amps. The substrate heating is controlled with a halogen lamp assembly, thermocouple, and temperature controller.

After building the system, sputtered amorphous silicon was used to verify that the hydrogenation chamber functioned as expected. That is, that the heated tungsten filament

catalytically generates atomic hydrogen from a hydrogen gas.

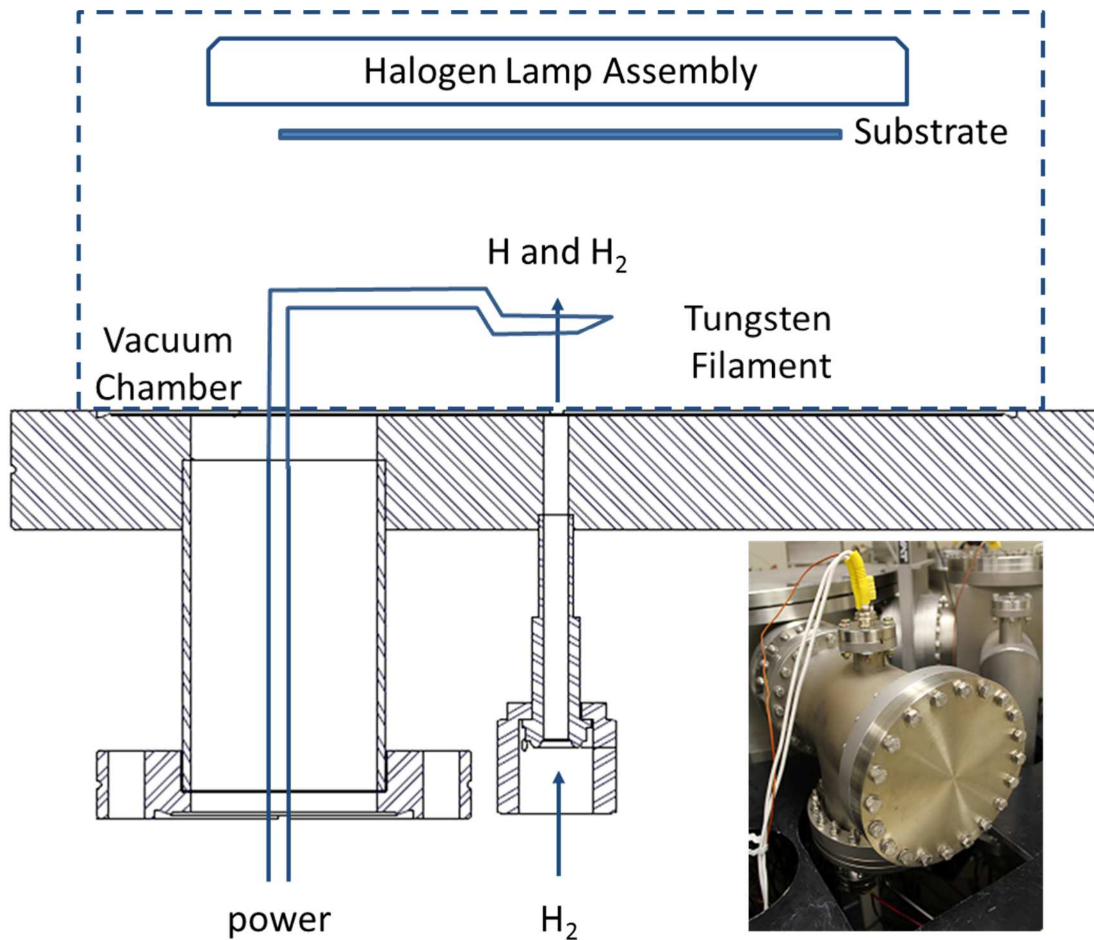

Figure 4.7 Atomic hydrogen annealing system schematic diagram with photograph inset in the bottom right.

Sputtered amorphous silicon was chosen because it is inherently not hydrogenated, but has been shown to readily incorporate mostly SiH_2 bond configurations when grown in the presence of hydrogen [4.14]. Atomic hydrogen approaching the surface of a sputtered amorphous silicon sample can etch and/or be incorporated into the film. Fourier transform infrared spectroscopy (FTIR) was used to determine the hydrogen bonding present. Si-H bonding presents as a peak at 2000 cm^{-1} while clustered Si-H around micro/nano voids and Si-H_2 absorb with a peak typically between 2080-2100 cm^{-1} [4.15]. Various filament temperatures and pressures were tested until hydrogen incorporation into the sputtered films was observed.

The filament temperature was kept constant at 1900 °C and uniformity, substrate temperature, and pressure were varied to optimize the hydrogen inactivation of aluminum dopant. TAIC thin films with minimal layer exchange were first used as a more sensitive detector of atomic hydrogen than sputtered amorphous silicon. Eight TAIC samples were prepared with 300 nm a-Si:H and 50 nm aluminum annealed at 300 °C on glass samples. The aluminum was removed before hydrogenation was attempted.

4.4 Effect of Substrate Temperature

Two samples were hydrogenated for each substrate temperature: 100 °C, 150 °C, 200 °C, and 250 °C. Figure 4.8 shows original resistivity and post-hydrogenation resistivity for each pair of samples. The average baseline resistivity for these samples, as determined by the Van-der Pauw method on 1 cm^2 samples with indium contacts in the corners was 0.055 Ω-cm.

Figure 4.8 shows that there is an optimal temperature for hydrogenation given the other parameters. The temperature dependent reversal of resistivity change has been determined experimentally for boron as 150 °C [4.9]. This is a trap limited diffusion process, but there is still a temperature dependence so that when the temperature increases, formation of boron-hydrogen complexes increases and can be described as a typical activation energy and temperature dependent relationship. Therefore, the optimum inactivation percentage of a film, or aluminum-hydrogen complex formation, is a trade-off between rapid diffusion and reactivation of the acceptor impurity level in silicon from substitutional aluminum. This observation necessitated a study of hydrogen-aluminum complex deactivation.

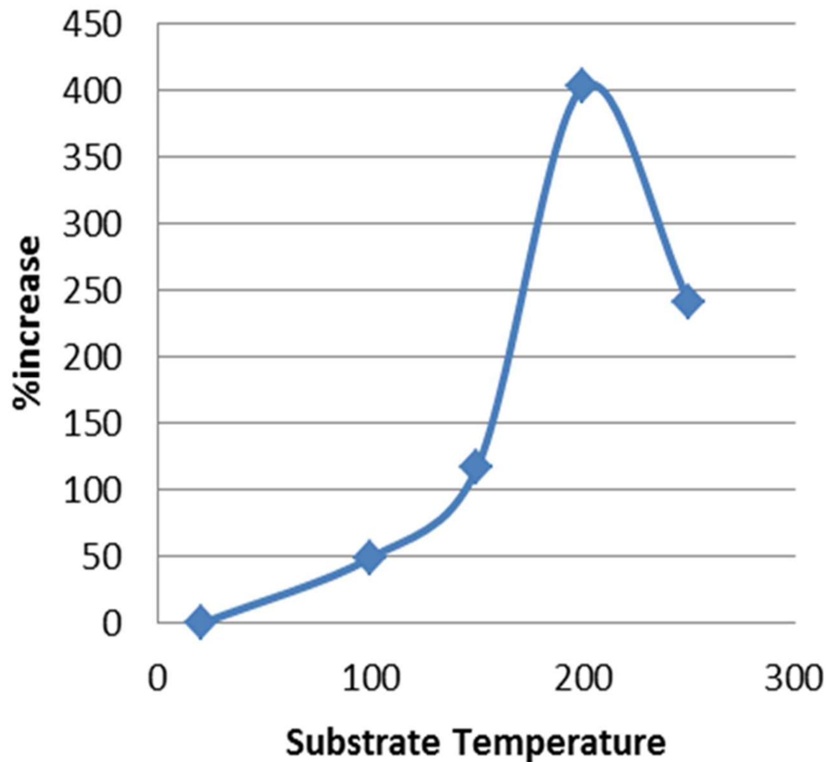

Figure 4.8 % Increase in resistivity for TAIC films on glass after 30 minute hydrogenations at various temperatures.

4.5 Thermal Restoration of Original Resistivity

The same samples were heated with the optical annealing apparatus sequentially for 30 minutes at 125 ^{o}C, 175 ^{o}C, 225 ^{o}C, 275 ^{o}C, and 325 ^{o}C until the original resistivities were restored. The values shown in Figure 4.9 represent the averages of the sample pairs. The preliminary data indicate that lower hydrogenation temperatures result in more stable inactivation of aluminum. The implication for the adoption of using hydrogen as a selective emitter is that there may be a trade-off between processing time and the stability of boron-hydrogen complexes. The highest temperature process, including reliability testing, that solar cells experience is the 150°C ethylene vinyl acetate (EVA) curing process, although this can be done at lower temperatures and non-EVA alternatives exist.

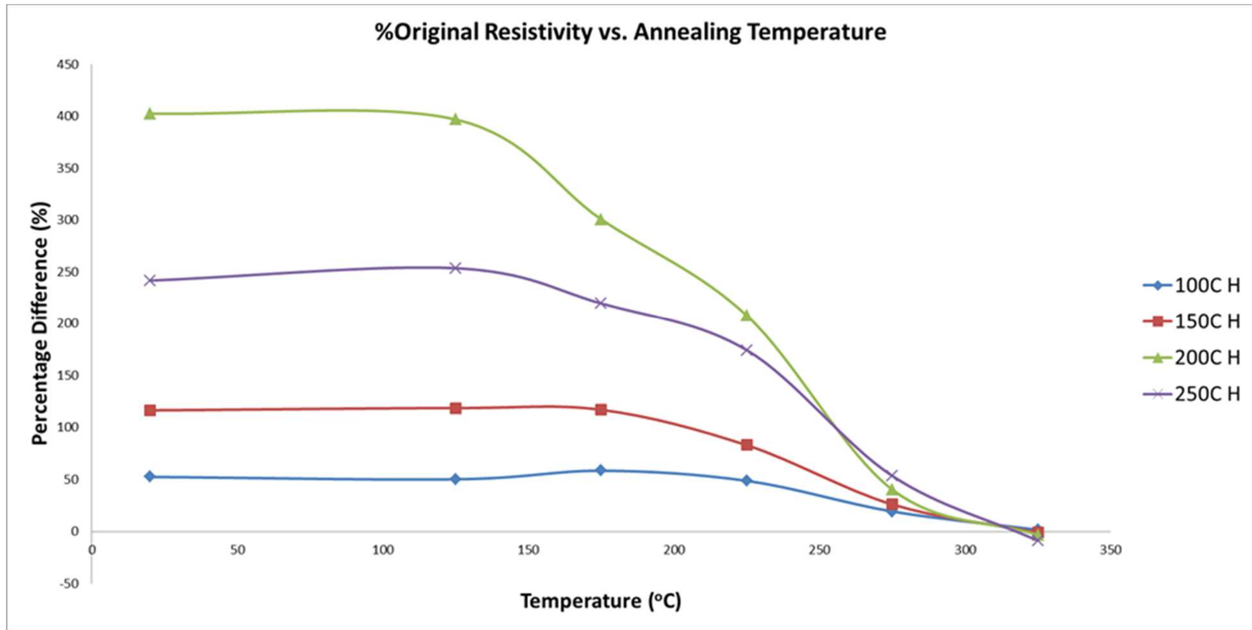

Figure 4.9 Resistivity change as a percentage of original resistivity through sequential 30 minute annealing cycles.

The hall mobility of these samples before hydrogenation were about 1 cm^2/V-s and were not measurable after hydrogenation. Mobility in fine-grained polycrystalline silicon does not follow the same model of single crystalline silicon where mobility always increases with decreasing doping density over the range important to solar cells. Contrarily, mobility in polycrystalline silicon experiences a "dip" at a certain resistivities. This phenomenon has been studied extensively through theoretical modeling and experiments [4.16], [4.17], [4.18] and is dependent on grain size and doping density. With high doping, traps at grain boundaries are saturated by charge carriers and mobility can reach values approaching those of crystalline silicon. This mobility minimum has been reported to occur in the $10^{17} – 10^{18}$ cm^{-3} range, which is the range of TAIC polycrystalline films and TAIC seed layers used in this work.

4.5 Hydrogenation with varying H_2 Pressure

Ten additional 1 cm^2 TAIC samples were prepared (300 nm a-Si:H, 50 nm aluminum, and 30 minute anneal at 230°C). These were hydrogenated at different pressures for 30 minutes

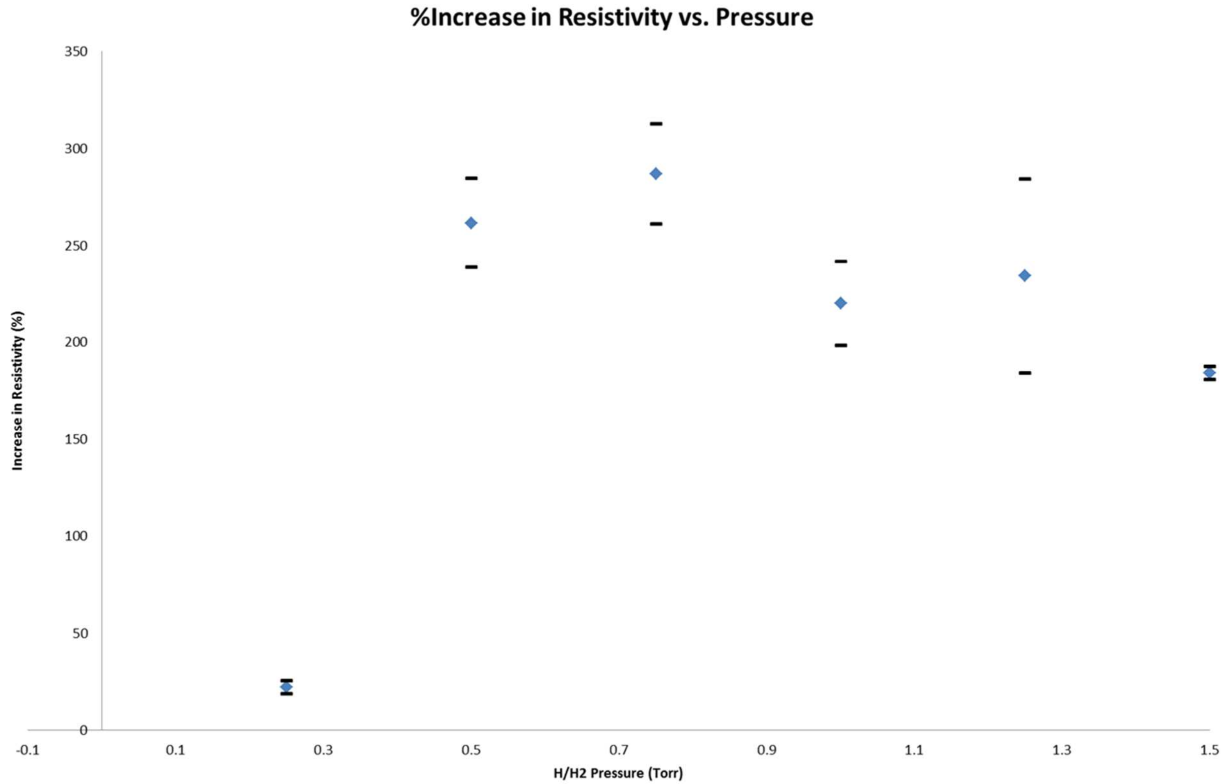

Figure 4.10 Atomic hydrogen inactivation shown as a percentage increase in resistivity versus pressure of H_2 gas.

with a substrate temperature of 200°C. The different pressures were 0.25, 0.5, 0.75, 1.0, 1.25, and 1.5 Torr. Figure 4.10 shows the results. The optimal hydrogenation boundary seems to be from 0.5 to 1.25 Torr with the lowest and highest pressures exhibiting inefficient acceptor inactivation. Low pressures may be ineffective due to a lack of atomic H generation. At higher pressures, atomic hydrogen generated at the surface of the filament can recombine into H_2 before reaching the sample surface. Both of these regimes were found to perform poorly for rehydrogenating amorphous silicon [4.19].

It is important to note that the change in resistivity is related to the starting resistivity. Atomic hydrogen inactivation of boron has been found to be effectively modeled by a trap limited diffusion process. If doping density increases, then the penetration depth of hydrogen-

boron complex formation will decrease given the same hydrogenation conditions. It was almost always the case that a lower starting resistivity would result in a lower ending resistivity when comparing between samples. According to Fig. 4.4, however, this should not be the case given the doping density ranges and substrate temperatures tried (black outlined box). Another likely explanation for this observation is that the non-layer exchange TAIC samples on glass were differentially crystallized and doping depths were different. Higher resistivity samples may have simply had less crystallization fractions which were more easily inactivated than other samples.

Additionally, viewing results based on change in resistivity can be intuitively misleading due to the relationship. For example, two samples each with 99.47% and 99.24% inactivated dopants had measured resistivity increases by 6670% and 4608%, respectively. The sample with lower inactivation percentage also had a higher initial doping concentration, so the effectiveness of the hydrogenation was even closer than the percentage increase in resistivity suggests.

4.6 Uniformity Study

The uniformity of the hydrogenation chamber was then tested. The sample set for the 1 Torr group in Fig. 4.10 were all ten TAIC samples while the other pressures were tested with sample pairs placed in the center of the annealing zone. Figure 4.11 shows the placement of these samples in the substrate holder and the results are in Table 4.1. The inactivation percentages were calculated from the ASTM standard empirical formula for boron concentration in silicon as a function of resistivity [4.20].

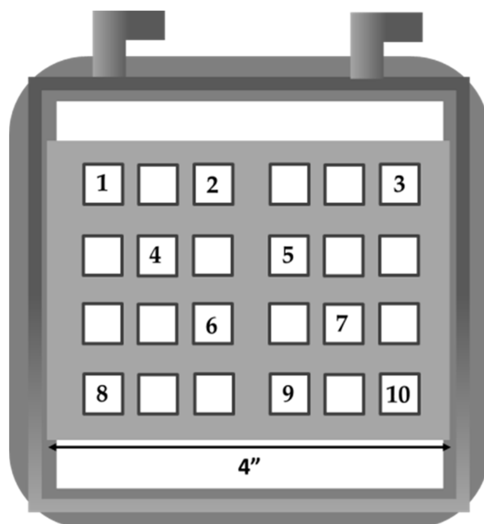

Figure 4.11 Sample placement for uniformity study on TAIC non-layer exchange films.

Table 4.1 Data from uniformity study of the hydrogen annealing chamber. Original and post-hydrogenation resistivity values are given and % inactivation is calculated assuming boron as the dopant.

Sample #	Original Resistivity (Ω-cm)	Hydrogenated Resistivity (Ω-cm)	Inactivation (%)	Crystallization Fraction (%)
1	0.052	0.144	78.52	57.21
2	0.057	0.190	83.21	63.11
3	0.058	0.189	82.62	62.98
4	0.074	0.259	83.40	64.93
5	0.055	0.167	81.00	66.96
6	0.056	0.187	83.30	65.93
7	0.058	0.194	83.23	64.92
8	0.054	0.176	82.84	69.58
9	0.055	0.177	82.48	68.54
10	0.052	0.152	80.12	68.01

The hydrogenation chamber was moved from its original location. It was placed at the load-lock position of the ITZ and was turned upside down to avoid cutting the frame of the system. A new filament design was used, and an experiment using TAIC seed layers was performed to ensure uniformity. Four samples were cut from the center of a 1.5"x1" TAIC silicon on glass sample. Hydrogenation was performed for 30 minutes with a substrate temperature of 150°C, a pressure of 1 Torr, and a filament temperature of 1900°C. Sample

locations are shown in Fig. 4.12 and results are given in Table 4.2. TAIC seed layers are much higher quality than TAIC samples where layer exchange is minimized.

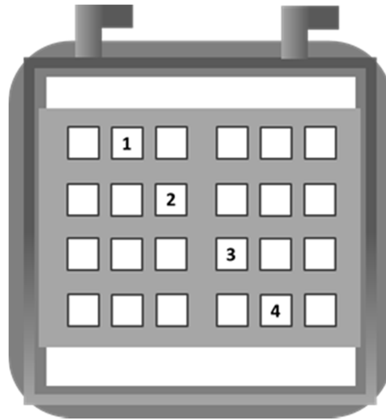

Figure 4.12 Sample placement for uniformity study after MPZ 5 relocation with large-grain TAIC seed layers.

Contrary to reported mobility increases in hydrogen-compensated silicon samples [4.20], the mobility of TAIC seed layers decreases 3-5x after hydrogenation. This is possibly due to defect formation due to the introduction of too much hydrogen, a mechanism that is taken advantage of in the "Smart-Cut" process [4.21]. The percentage inactivation on the ~130 nm thick films was 99.45 ± 0.09%. While only increasing uniformity slightly, the new filament design is four inches longer and is about one inch closer to the sample surfaces. While the mechanism of dopant inactivation in poorer quality material may be different, it seems that the new filament is much more efficient than the old design.

Table 4.2 Data for uniformity study after the chamber moved from MPZ5.

Sample #	Original Resistivity (Ω-cm)	Hydrogenated Resistivity (Ω-cm)	Original Mobility (cm^2/V-s)	Hydrogenated Mobility (cm^2/V-s)	Inactivation (%)
1	0.044	3.00	45.35	10.98	99.53
2	0.049	2.96	36.53	10.95	99.45
3	0.043	2.01	39.75	12.33	99.33
4	0.044	2.74	46.77	12.43	99.49

4.7 Theoretical Simulations of the Hydrogenated Selective Emitter

Although hydrogenation was found to lower the mobility of TAIC films, the process was found to increase mobility while lowering the doping density in single crystal silicon [4.22]. EDNA was used to simulate the performance of both homogeneous and hydrogenated solar cell emitters. Losses through Auger and SRH recombination were analyzed and resulted in decreases in Jsc and Voc, or increases with decreasing surface recombination velocity. Emitter collection efficiency is defined as the carrier collection percentage of total carriers generated under short circuit conditions. EDNA assumes no loss mechanisms from the base of the solar cell, therefore Voc is an implied voltage. Jsc values reported are only for carriers collected from the emitter.

The hydrogen selective emitter (HSE) process works by inactivating the electrical activity of boron in p-type emitters. Increasing surface doping also increases surface recombination velocity, thus limiting solar cell efficiency. However, decreasing surface doping has traditionally had a drastic impact by increasing sheet resistance. The HSE eliminates this trade-off by inactivating boron dopants up to 99.9% near the surface. Depending on the hydrogenation conditions, this inactivation trails off such that high conductivity emitters are possible while having very low surface doping. The goal was to achieve emitters which were compatible with high power conversion efficiencies while achieving emitter sheet resistance lower than normal in order to reduce the silver costs of the front surface grid lines. Simulation outputs and experimental data were combined to guide emitter design and HSE process parameters.

EDNA, a simulation software package developed by researchers at PV Lighthouse (www.pvlighthouse.com.au), was used to simulate non-standard emitter characteristics. This modeling software has advantages over the widely used PC-1D since it employs the latest Fermi-

Dirac based models for Auger recombination in addition to allowing for more advanced emitter doping profiles. A description of the software has been published [1.8] and has been used by research and commercial entities. The general approach to modeling used here was to start with either theoretical or experimental emitters, simulate the emitter characteristics, modify the emitter with either theoretical or experimental hydrogen inactivation profiles to arrive at a hydrogen super emitter (HSE) active dopant profile, and again simulate the HSE emitter characteristics. Key metrics are surface Shockley-Read-Hall recombination, Auger recombination, emitter reverse saturation current density (J0e), implied voltage, and implied efficiency. The implied voltage and efficiency both assume that other components of the cell are not limiting the theoretical device, that the fill factor is 80%, and that the maximum short circuit current of the entire solar cell is 40 mA/cm^2. The surface recombination velocity (SRV) of each emitter was varied between 0 cm/s and 3x 10^6 cm/s. 3 x 10^6 cm/s was chosen because at the solid solubility limit for boron in silicon, a concentration of around 3 x 10^{20} cm^{-3}, 3 x 10^6 cm/s is the value for SRV corresponding to that level of surface doping.

Figure 4.13 shows both experimental and estimated boron-hydrogen pair concentration versus depth in crystalline silicon. The surface dopant concentration can be inactivated by about 99.5% and this was verified by spreading resistance profiling (SRP). 99.5% dopant inactivation at the surface changed the surface dopant level from 3 x 10^{20} cm^{-3} to 1.5 x 10^{18} cm^{-3}. The corresponding drop in theoretically achievable SRV was from 3 x 10^6 cm/s down to 117.4 cm/s. For the baseline case, a 36.61 Ω/□ emitter with a Gaussian profile was modeled with a surface boron doping of 3 x 10^{20} cm^{-3} and a junction depth of 0.5 μm on a background phosphorus doping of 1 x 10^{15} cm^{-3}. With an SRV of 3 x 10^6 cm^{-3}, a cell with this type of emitter would have a maximum efficiency of 18.73%.

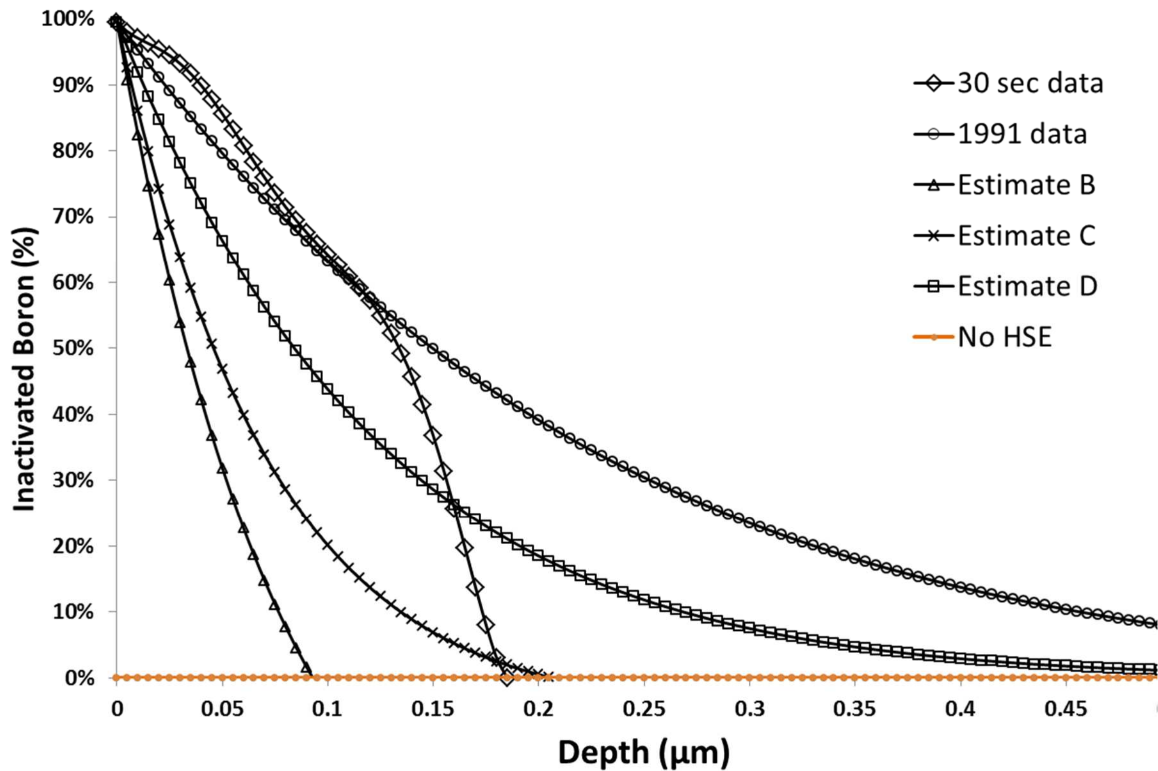

Figure 4.13 Boron-hydrogen complex concentration versus depth. 100% means that each boron atom has been electrically inactivated. "30 sec data" and "1991 data" have been determined experimentally. B, C, and D are estimated [B-H]/[B] curves. No HSE has 0% inactivation.

Figure 4.14 shows the original doping profile as well as the modified profiles based on experimental and estimated hydrogenation data. Depending on the level and depth of inactivation, the sheet resistance of the original emitter increased from 36.61 Ω/□ to 106.27 Ω/□.

Table 4.3 lists the emitter characteristics of the original low sheet resistance emitter and the HSE emitters based on inactivation of boron dopants to the levels shown in Fig. 4.13. The emitter with the greatest improvement also had the highest sheet resistance. As seen from the table, this is due both to decreased SRH recombination at the surface as well as limited Auger recombination in the emitter. Any recombination in the emitter negatively impacts J_{0e}, limiting Voc, and thus limiting efficiency. Although the HSE emitters performed better than the original emitter, the sheet resistance of the best performing emitter ("1991") was also high enough to

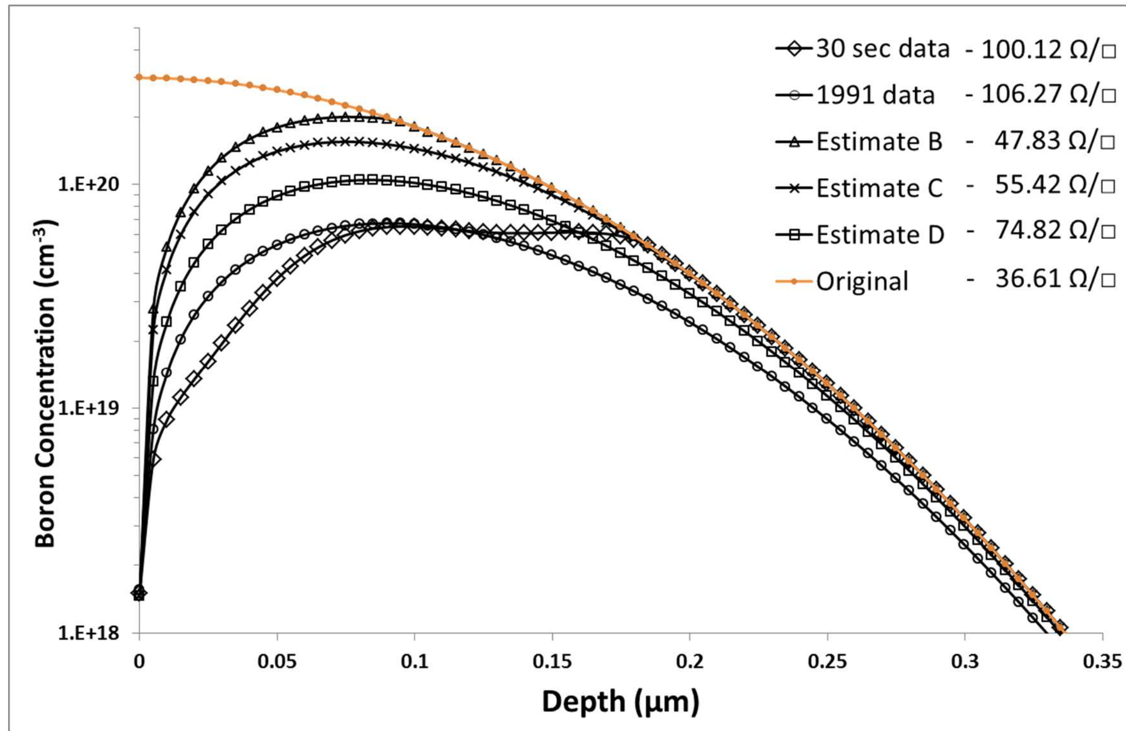

Figure 4.14 [B-H] profiles from Fig. 1 applied to a 500 nm deep Gaussian boron profile. The sheet resistance of the original emitter was 36.61 Ω/□. The corresponding sheet resistances for the experimental and theoretical profiles are also given.

increase the amount of silver that would be required at the front of a solar cell. This potentially limited efficiency in three ways: decreased fill factor if the grid lines were not spaced closer together, increased coverage of the front surface, thereby decreasing efficiency. Additionally, parasitic recombination at the metal-silicon interface may also have acted to decrease efficiency depending on the metallization quality. Other modeling outside of EDNA will be necessary to determine the optimal case for efficiency considering grid optimization.

Table 4.3 Simulated emitter characteristics for various experimental and estimated HSE emitters.

Profile	R_{sheet}	SRV	SRH_{surf}	$Auger_{emitter}$	J_{0e}	iVoc	Eff. %	Improvement
Original	36.61	3e6	2.01	0.07	242.8	617.5	18.73	Δ Efficiency
B	47.83	3e2	0.08	0.14	49.3	666.0	21.19	↑ 13.17%
C	55.42	3e2	0.06	0.12	47.9	666.8	21.24	↑ 13.42%
D	74.82	3e2	0.05	0.07	41.5	670.8	21.40	↑ 14.28%
30 sec	100.12	3e2	0.04	0.05	34.5	675.7	21.57	↑ 15.20%
1991	106.27	3e2	0.03	0.04	32.8	677.0	21.62	↑ 15.45%

It is also interesting to explore the effect of changing surface recombination velocity on the level of SRH recombination for emitters of varying surface dopant levels. Early on in n-type cell development, it was concluded, perhaps prematurely, that oxide passivation on p-type emitters was unstable. These cells had very lightly doped emitters and, when coupled with a poor passivation layer, had severely degraded efficiency due to both loss in short circuit current and open circuit voltage. When modeling emitters, it becomes readily apparent that lighter doped emitters are more sensitive to surface SRH recombination. With increasing SRV, SRH recombination increases more for a lightly doped emitter than for a heavily doped emitter.

This trend can be seen when modeling the HSE emitters in EDNA. Figure 4.15 shows that at high SRV values, the HSE emitters performed worse than the heavily doped, original emitter. Since the modeled HSE emitters had surface doping of 1.5e18 cm^{-3}, their limiting SRV value was actually below 300 cm/s. Very little recombination occurred at these SRV values. Compared to the limiting SRV of the original emitter of 3×10^6 cm/s, each of the HSE emitters studied had the potential of increasing the short circuit current density by about 1.95 mA/cm^2 (also see data in Table 4.3). The HSE profile most closely resembling the original profile was "B". This profile was more resistant to SRH recombination at higher SRV values, but also showed the highest SRH at 300 cm/s.

Comparing the Auger recombination versus SRV revealed an interesting characteristic. Auger recombination increases with increasing dopant density. Despite having fewer electrically active dopants, the B and C HSE emitters had higher Auger recombination at 300 cm/s than the original emitter does at 3×10^6 cm/s. This is because of a slight trade-off between SRH recombination and Auger recombination. Whenever SRH is reduced due to the low surface

recombination velocity (i.e. with excellent surface passivation), there are more carriers able to recombine through Auger recombination.

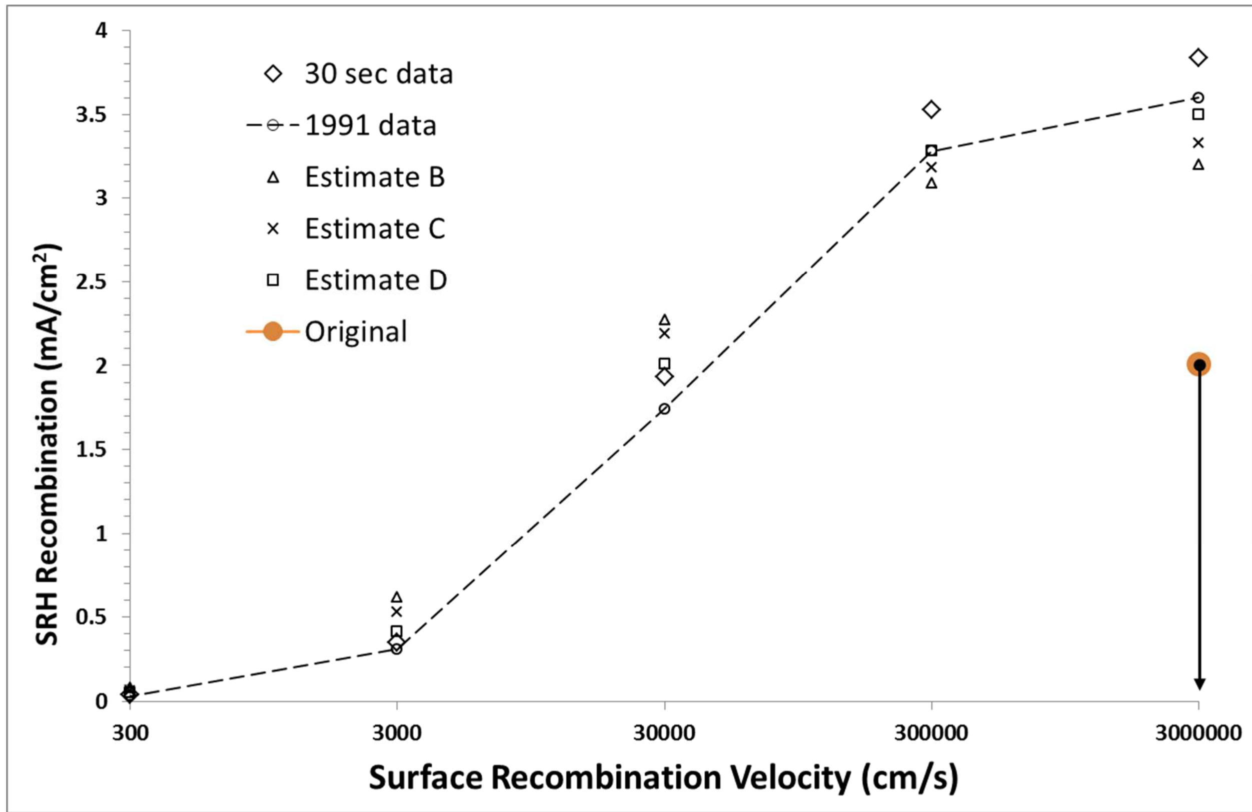

Figure 4.15 Surface SRH recombination versus SRV for original and various HSE emitters as modeled in EDNA.

Figure 4.16 shows the Auger recombination in the emitter versus surface recombination velocity for each of these emitters. At the surface recombination velocities of interest, the Auger recombination of emitters "30 sec" and "1991" was lower than the original emitter at 3×10^6 cm/s.

Overall, the best performing emitters from the simulations tended to be those with the highest sheet resistance. However, emitter "B" with only marginally higher sheet resistance than the original emitter, still showed a maximum theoretical increase of 13.17% efficiency over the baseline cell. Additional efficiency would come from reducing silver shading, not to mention the

cost benefit of using less silver. Reducing the number of gridlines on a typical cell from 80 to 62, corresponding to maintaining the same power loss between a 70 Ω/□ emitter compared to a 45 Ω/□, saves about 2.6 cm^2 assuming 100 µm wide gridlines. So comparing emitter B to D, for instance, emitter D would need 35% more gridlines than emitter B to have the same power loss due to the emitter contribution to series resistance. Lowering the number of grid lines can also increase series resistance if the metallization paste has poor conductivity. In conclusion, theoretical treatment of both experimental and simulated HSE emitters showed very good potential for improving low sheet resistance emitter performance with efficiencies well above 21% achievable from these few baseline cases.

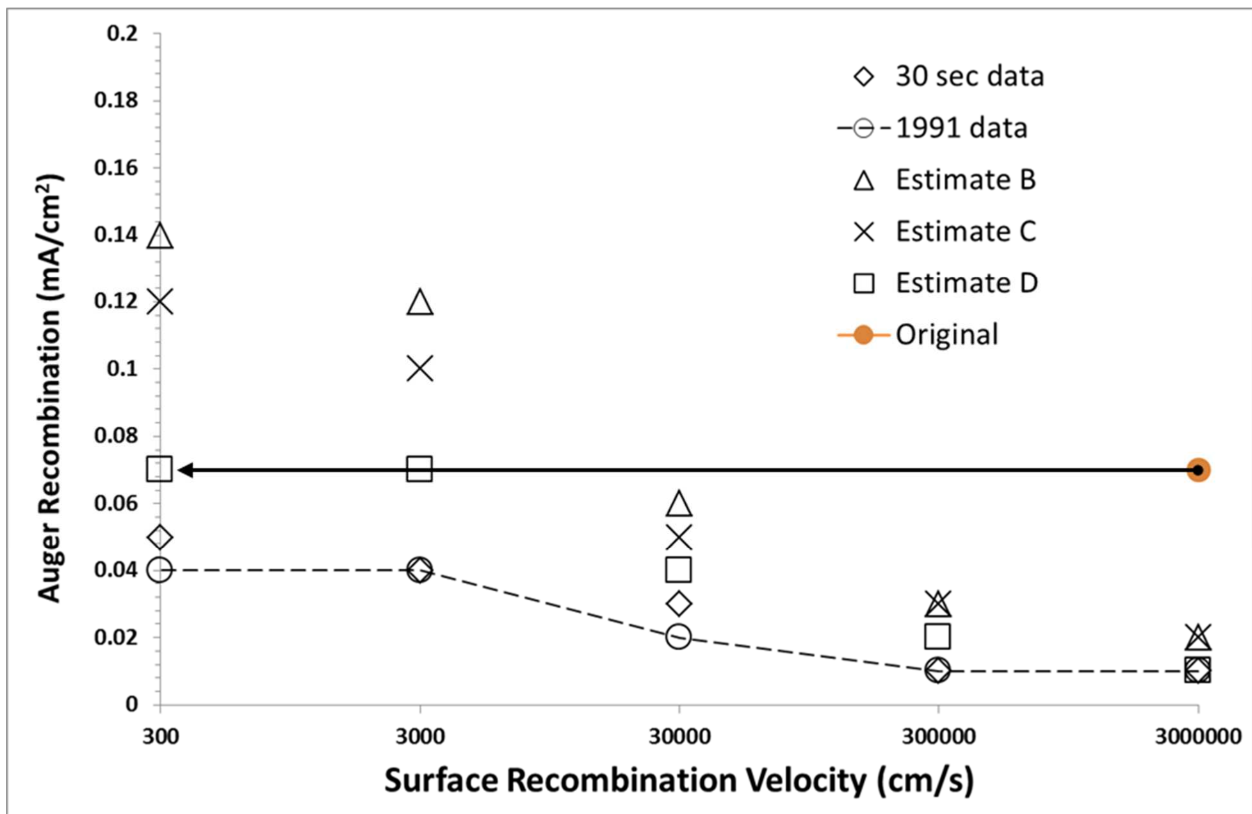

Figure 4.16 Auger recombination in the emitter versus surface recombination velocity for original and HSE emitters.

Modeling of the kinetics of B-H complex formation has been attempted with limited success [4.22]. However, experimental evidence for inactivated profiles in highly doped silicon such as the dopant concentrations found in emitters of n-type solar cells has been reported [4.9].

The potential benefits to the solar cell are clear, however a fundamental question remains to be answered: Is surface recombination velocity high for highly doped surfaces because of the electrical activity of those surfaces or because of the physical presence of the substitutional donors or acceptors? This question is addressed with experimental evidence in Chapter 5.

CHAPTER 5: EXPERIMENTAL PROOF OF CONCEPT FOR THE HYDROGEN SELECTIVE EMITTER

Simulations clearly indicated that a decrease in efficiency should be expected with the emitter profiles simulated from hydrogen inactivation of boron acceptor impurities with poor quality surface passivation. Indeed, initial tests of newly created n-type cells showed a decrease in performance consistent with EDNA simulations. However, cells that have appreciable native oxide have sufficient surface passivation in order for the hydrogenation process to increase cell efficiency.

5.1 Fabrication of Diffused Junction Solar Cells

Two sets of cells were fabricated starting with 0.1 to 0.9 Ω-cm phosphorus doped silicon. These wafers were 475-500 μm thick, single-side polished. PECVD oxide was deposited on the rear surfaces and sides of these wafers to limit boron diffusion to the front surface (emitter). Wafer A was diffused at 1150 ^{o}C with a soak time of 15 minutes. Wafer B was diffused at 1150 ^{o}C with a soak time of 7 minutes. After the pre-deposition diffusion, the wafers were oxidized at 750 ^{o}C and HF dipped for 2 minutes to remove boron rich layers. Next, >500 nm aluminum was deposited on the front and back surfaces of the wafers. Front contacts were photolithographically defined using the SNL Mask Level 3A (described earlier in Chapter 2). The final structure from base contact to emitter contact was aluminum, n-type silicon, p-type diffused silicon, and aluminum.

In order to model the device physics of these particular cells in EDNA, spreading resistance profilometry was carried out on seven samples from the same wafers as the cells taken from wafers A and B. These samples were exposed to atomic hydrogen with a substrate temperature of 150 ^{o}C, a filament temperature of 1900 ^{o}C, H_2 flow rate of 15 sccm, gas pressure of 1 Torr, and processing times of 30 seconds, 1 minute, 3 minutes, 5 minutes, 8 minutes, and 30

minutes (one from wafer A and one from wafer B). The other samples were all from wafer B. The original doping profile of wafer A was determined from the 30 minute hydrogenated sample by heating the sample up to 350 ^{o}C for one hour to reactivate the electrical activity of the boron dopants. The original doping profile of wafer B was determined from the 30 second hydrogenated sample in the same way.

Having this data allows analysis of the emitter with the EDNA simulation program since measured dopant profiles are a direct input of the program. In this way, the performance of the emitters can be analyzed for projected recombination losses and matched with the experimental quantum efficiency data to estimate surface recombination velocities after the hydrogenation process. Although there is an empirical model for surface recombination velocity versus surface dopant level for phosphorus diffused surfaces, a similar model has yet to be derived for boron doped surface, although similar trends have been observed experimentally [4.5], [4.6]. There are also internal models to choose from for modeling Auger recombination within the emitter. The model chosen for this work was developed by Kerr and Cuevas [5.1].

Both SRH recombination related to the surface recombination velocity input parameter and Auger recombination limit the short circuit current such that carriers generated within the emitter do not become a collected current, or the short circuit current from the emitter. Deeper diffusions, as modeled in EDNA, result in higher generated current in the emitter simply because of the increased depth. This does point out a design characteristic of industrial solar cells, however. Shallow, highly doped, diffusions have been preferred in the past despite the knowledge that lighter doped emitters suffer less from both SRH and Auger recombination. Carriers generated within the bulk just below the junction have nearly 100% collection efficiency if the material quality is even moderate. By using shallow junctions, overall quantum efficiency

improves even though the emitter quality is very poor. Having access to new emitter design processes like the hydrogen selective emitter, may open new possibilities for industrial emitter design without the need to sacrifice emitter conductivity.

Figure 5.1 shows the boron dopant profile of wafer A as determined by SRP measurements after exposure to atomic hydrogen for 30 minutes. These cells originally had a peak surface doping of 9.7×10^{19} cm^{-3} and a junction depth of 800 nm. The phosphorus background doping was measured to be 1×10^{16} cm^{-3}. After hydrogenation for 30 minutes, the peak dopant density was 1.9×10^{18} cm^{-3} with a junction depth of 740 nm. This is an inactivation

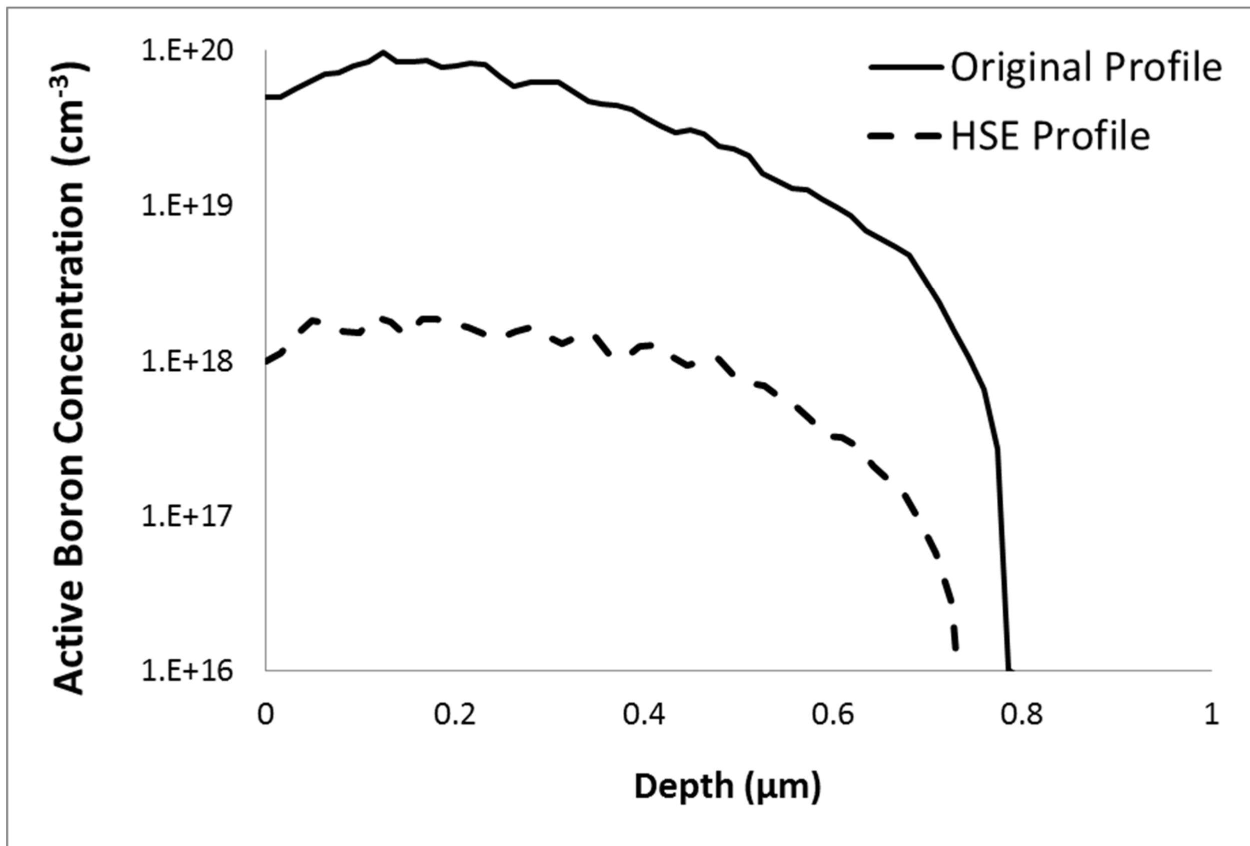

Figure 5.1 Original boron dopant profile in n-type silicon and after the hydrogenated selective emitter (HSE) process was performed.

of 98 % of peak electrically active dopants near the surface, and enough inactivation into the emitter to decrease the electrical junction depth by 60 nm.

Another important component of solar cell design is the emitter sheet resistance. As sheet resistance increases, power loss due to the silicon between grid contacts can be quite substantial, depending on the grid design. The grid used for these cells was the concentrator design used for the TAIC emitter solar cells. It has very close grid spacing with a connected contact pad on the perimeter of its 1 cm^2 active device area. This design minimizes losses due to sheet resistance and thus increasing sheet resistance for these cells did not result in measureable efficiency losses from decreased fill factors.

PC-1D was used to fit the quantum efficiency data assuming the reflection was of crystalline silicon, an assumption verified by third-party reflection measurements on HSE processed silicon (shown in Fig. 5.2).

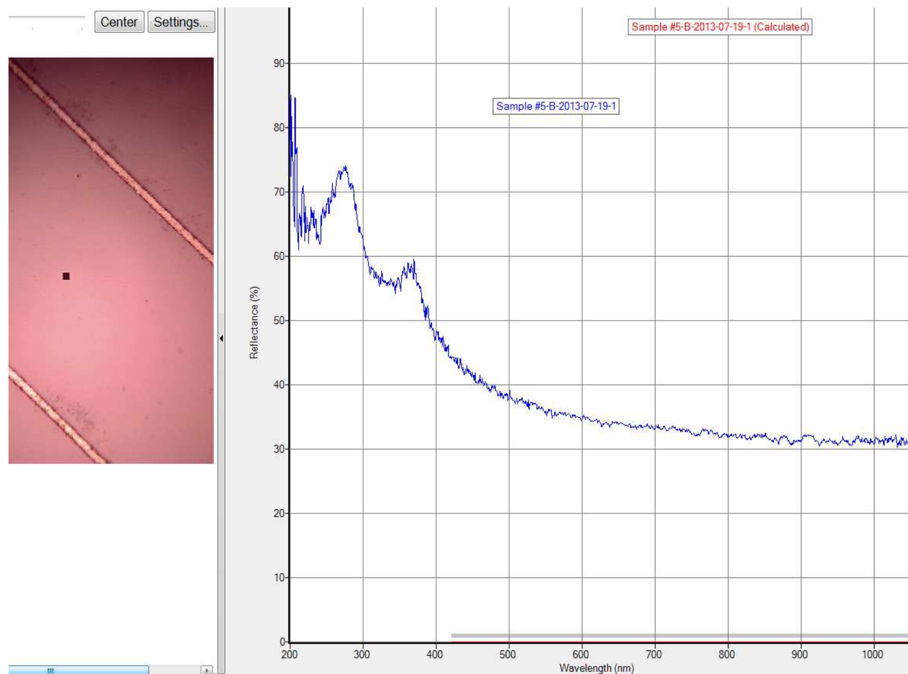

Figure 5.2 Reflection of the surface of the diffused solar cells indicates the cell has a planar silicon surface.

This procedure gives estimates for surface recombination velocities, bulk material lifetime, dopant densities, and junction depth. Figure 5.3 shows both the experimentally measured quantum efficiency curves before and after the hydrogenation process as well as EQE curves fit to this data in PC-1D. Very precise matches are difficult to achieve in PC-1D because

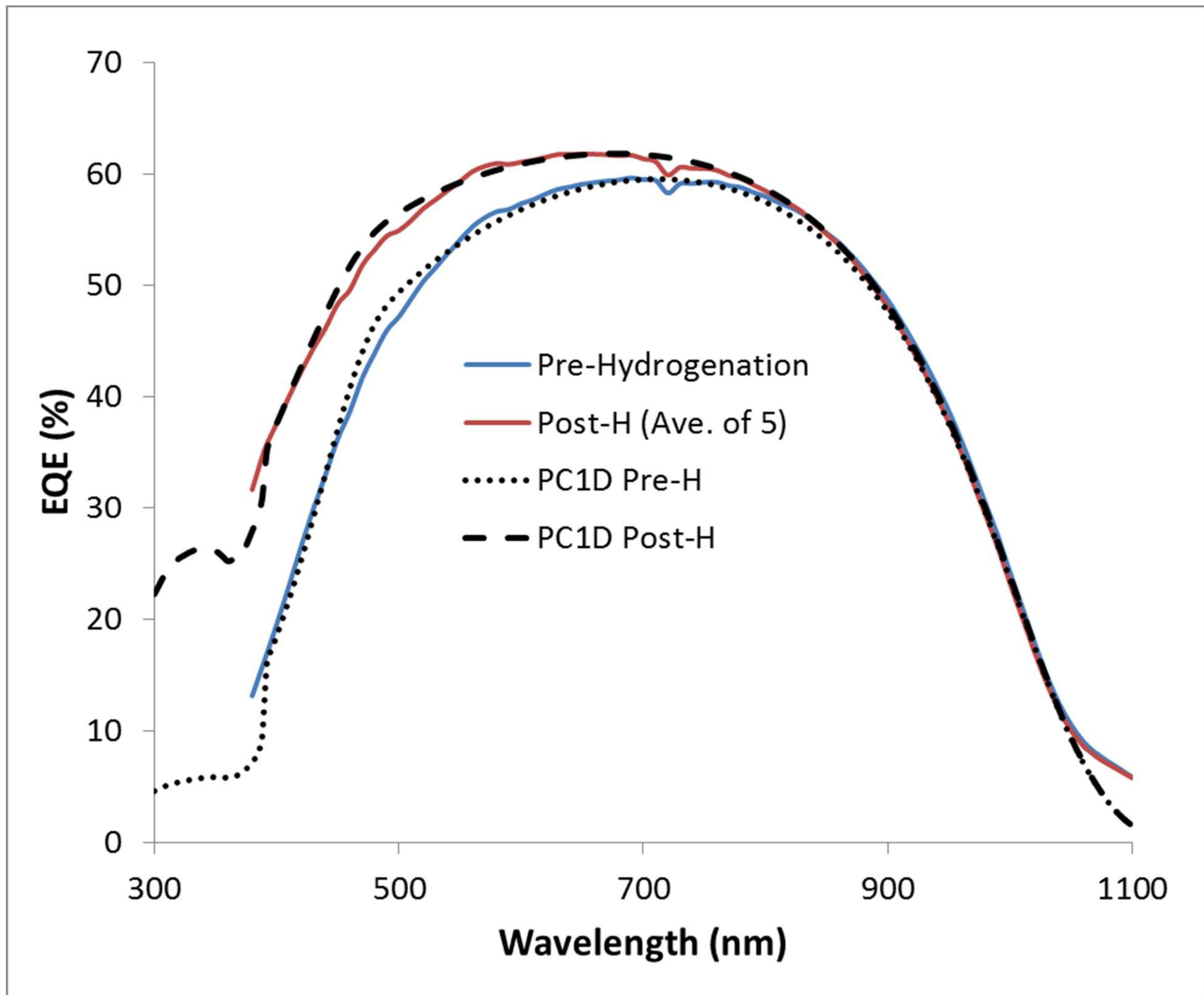

Figure 5.3 External Quantum Efficiency curves for solar cells from wafer A before and after hydrogenation.

the shapes measured by SRP are not achievable with the built-in dopant profile models in PC-1D. The junction depths and peak dopant values were matched with the SRP data. The best fit was set with a bulk minority carrier lifetime of 3 μs and a rear surface recombination velocity of $1x10^6$ cm/s. For the pre-hydrogenation curve, a front SRV of $2x10^6$ cm/s was found to provide

the best fit. For the post-hydrogenation curve, a front surface recombination of $2x10^5$ cm/s was found to provide the best fit. This represents an order of magnitude decrease in surface recombination velocity after the HSE treatment.

Based on the PC-1D fits, simulations of the two dopant profiles were performed in EDNA. The SRV parameter of 2×10^6 cm/s was used for the original dopant profile, and 2×10^5 cm/s was used for the HSE modified profile. According to the EDNA models, the sheet resistance of the original diffusion was 36.54 Ω/□. The total current generated in the emitter under AM1.5g illumination was calculated to be 10.22 mA/cm^2. Of the current generated, only 5.16 mA/cm^2 is collected. 4.94 mA/cm^2 recombine at the surface of the emitter, and another 0.13 mA/cm^2 is lost to Auger recombination within the emitter.

Because of the decreased junction depth, the total generated current in the HSE processed emitter was 9.83 mA/cm^2. Because of the lower SRV value, the collection current was 7.56 mA/cm^2. 2.27 mA/cm^2 was lost due to SRH recombination at the surface and there was no Auger recombination. This makes sense because Auger recombination is negligible for lightly doped emitters. Because the junction depth is less than for the original emitter, the generated current is also less in the emitter. The light is instead absorbed in the base of the cell, which has a higher collection efficiency due to a number of factors. The total possible current that could be collected from this shorter junction is the difference between the generated current in the original junction depth and the generated current in the shallower HSE junction: 10.22 mA/cm^2 – 9.83 mA/cm^2 = 0.39 mA/cm^2.

This difference must be accounted for when considering the increased short circuit current observed after the HSE process. However, if the bulk lifetime of the sample is not ideal, which is the case for this cell, with an estimated minority carrier lifetime of just 3 μs, then the

collection of this 0.39 mA/cm^2 will not be 100%. Another discrepancy that must be accounted for when comparing EDNA output to quantum efficiency measurements is that EDNA does not account for reflection. That is to say, EDNA assumes that 100% of photons are absorbed into the cell with no reflection or shading from emitter metallization. This can be corrected within EDNA by multiplying Reflection(λ) by the photon flux, such that the total number of photons entering the simulated device is equivalent to the number entering the real solar cells under test during the quantum efficiency measurement. The reflection of the solar cells used to test the hydrogenation process for wafers A and B were planar with an additional 4% absolute blocked by the grid contacts on the front surface of the solar cells. With these new changes implemented in EDNA, the output for generated and collected current should be directly comparable to that measured and shown in Fig. 5.3. The new output from EDNA for the original emitter shows 4.20 mA/cm^2 generated, 1.99 mA/cm^2 collected, 2.16 mA/cm^2 lost from SRH recombination at the surface, and 0.05 mA/cm^2 lost from Auger recombination. The new output from EDNA for the HSE modified emitter shows 4.06 mA/cm^2 generated, 3.07 mA/cm^2 collected, 0.99 mA/cm^2 lost from SRH recombination at the surface, and 0.00 mA/cm^2 lost from Auger recombination in the emitter. The difference in generated current due to junction narrowing was 0.14 mA/cm^2. Thus, the total possible difference in Jsc according to EDNA would be 1.22 mA/cm^2.

The Jsc was calculated from QE curves for each of the five cells before and after hydrogenation. The average absolute difference in Jsc was found to be 1.25 ± 0.2 mA/cm^2. This is very close to the 1.22 mA/cm^2 predicted by EDNA. Thus, the front surface recombination velocity found by fitting PC-1D quantum efficiency curves to the experimental data is likely close to the actual values. The front surface SRV may be limited by the inherent quality of the native oxide, despite native oxide and other thin oxides (< 2 nm) acting as successful passivation

layers in conjunction with silicon nitride anti-reflection coatings. However, the passivation on these cells did not reach the lowest values possible with lightly doped surfaces, despite the inactivation process.

Figure 5.4 shows the profiles for different hydrogenation times for samples from wafer B. The "No HSE" curve is the original dopant profile determined by heating up the 30 second HSE sample to 350°C for one hour and then again measuring the profile by SRP. After just 30

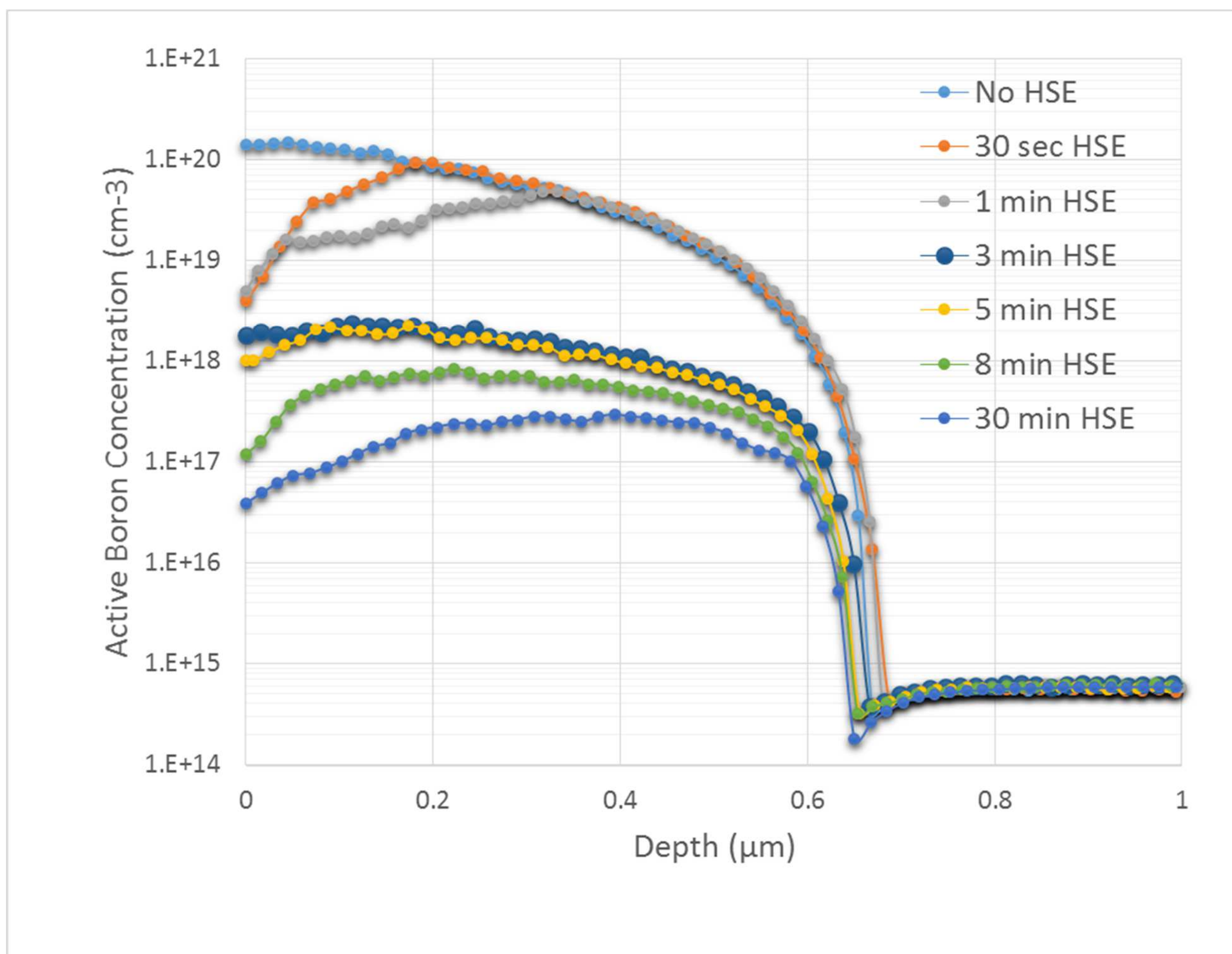

Figure 5.4 Original profile (No HSE) as well as changed doping profiles for various hydrogenation times.

seconds, the surface dopant density went from 1.39 x 10^{20} cm^{-3} to 4 x 10^{18} cm^{-3}. The measureable penetration rate of the inactivation of boron was 360 nm/minute. It is interesting to

note that after 30 minutes, the surface dopant inactivation reaches 99.98%. After just five minutes, the junction depth decreases from 685 nm to 650 nm.

EDNA simulations were performed based on these dopant profiles. Each measured profile was input and SRV values were calculated based on the surface dopant density using the model internal to EDNA. Table 5.1 contains the major performance characteristics of these different emitters. Each of these samples, hydrogenated from 30 seconds to 30 minutes, was from Wafer B. As the hydrogenation time increases, the current generated in the emitter decreases (Jgen) because of the narrowing junction. The 30 second hydrogenated emitter has theoretically higher Auger recombination than the emitter with no hydrogenation at all. However, SRH recombination is drastically reduced from 2.48 mA/cm^2 to 0.04 mA/cm^2.

Table 5.1 Modeled emitter characteristics of the profiles from varying HSE time. Jgen, Jcoll, SRH, and Auger all have units of mA/cm^2.

HSE Time (min)	Jgen	Jcoll	SRH	Auger	iVoc (mV)	J0e (fA/cm^2)	Efficiency (%)
0	9.78	7.04	2.48	0.26	621.6	254.2	18.5286528
0.5	9.78	9.46	0.04	0.28	670.8	51	21.2938752
1	9.78	9.62	0.03	0.13	682.4	33.1	21.7494528
3	9.61	9.6	0	0	726.8	5.9	23.2517856
5	9.55	9.54	0	0	725.2	6.3	23.2005984
8	9.49	9.49	0	0	714.3	9.5	22.8576
30	9.43	9.43	0	0	702.7	14.8	22.4864

As hydrogenation time continues, Auger recombination decreases as well until, after 3 minutes of hydrogenation, no appreciable Auger recombination is observed. After 3 minutes, the implied Voc reaches a maximum value of 726.8 mV. iVoc decreases after this because of decreasing dopant concentration. Solar cell efficiency based on the iVoc and the current losses were calculated by assuming a fill factor of 80% and total possible current density of 40mA/cm^2. For point of reference, the world record silicon solar cell had the following characteristics: Voc = 706 mV, Jsc = 42.7 mA/cm^2, FF = 82.8%, and an efficiency of 25% [1.1].

Four cells from Wafer B were hydrogenated for 5 minutes to achieve the dopant profile shown in Fig. 5.4. The original dopant profile and the 5 minute HSE profile were both analyzed in EDNA, accounting for the reflectance of the cells as described previously such that the output of EDNA could be directly compared to external quantum efficiency data. Then, by varying the SRV input for the hydrogenated profile in EDNA, a better estimate of the SRV value can be found than by fitting the quantum efficiency curves in PC-1D. According to the internal model for calculating SRV, the minimum SRV possible for the original emitter would be 2.59 x 10^5 cm/s. This would be with a high quality passivation layer. According to PC-1D, however, the surface recombination velocity of the original profile with unhydrogenated native oxide was around 1 x 10^6 cm/s. The SRV value was changed until the output from EDNA, ($\Delta Jsc\ from\ EDNA$), satisfied the following eq. 5.1:

$$\Delta Jsc\ from\ EDNA = 0.9(Pre\ H\ Jgen - Post\ H\ Jgen) + (Post\ H\ Jcoll - Pre\ H\ Jcoll) \quad (5.1)$$

($Pre\ H\ Jgen - Post\ H\ Jgen$) was the difference in generated current density simulated by EDNA for the original (Pre H) profile and the modified (Post H) profile. This quantity would be zero if the emitter depth had not changed due to hydrogenation. ($Post\ H\ Jcoll - Pre\ H\ Jcoll$) was the difference in collected carrier density before and after hydrogenation profiles were updated as simulated by EDNA. All current density values in Table 5.2 are given in mA/cm^2 and SRV is in cm/s. Table 5.2 lists these values as determined by the EQE curves of Fig. 5.5. The lowest SRV predicted by EDNA was 2500 cm/s. While this is not as low as what is predicted by the SRV calculator internal to EDNA, it is still quite possible that the native oxide used as a passivation layer for these cells was not ideal, as a high temperature thermal oxide or high quality Al_2O_3 passivation layer might be. Regardless, this is a 400x decrease in SRV compared to the pre-H condition, and 100 times better than if the cells had started with an

excellent surface passivation but with doping so high as to limit the lower bound of SRV to around 2.59 x 10^5 cm/s. This analysis, as well as the near-perfect EQE values after hydrogenation, indicated that a fundamental question to solar cell device physics has been further elucidated by the HSE process: That the electrical activity, and not the physical presence of dopants, is more responsible for increasing surface recombination velocity with increasing dopant density.

Table 5.2 Modeled SRV values based on experimental QE data and EDNA simulations.

Sample	Δ Jsc from EQE	Pre-H Jgen	Pre-H Jcoll	Post-H Jgen	Post-H Jcoll	Δ Jsc from EDNA	SRV (EDNA)
5	1.579	3.95	2.29	3.84	3.77	1.579	4000
9	1.312	3.95	2.29	3.84	3.503	1.312	18500
11	1.608	3.95	2.29	3.84	3.8	1.609	2500
15	1.506	3.95	2.29	3.84	3.697	1.506	8000

Figure 5.5 shows the average pre-H EQE curve, the post-H EQE curves for each of these four samples, and the reflectivity of c-Si. The internal quantum efficiency, calculated by adding the EQE and the reflectance curves, is nearly 100%. Interestingly, samples 9 and 15 did not achieve as high EQE values, despite having higher original EQE values. One explanation for this is that some contamination was present on these cells that interfered with the formation of a high quality native oxide. This contamination, in the absence of well passivating native oxide could have provided some level of surface passivation, leading to higher initial EQE values. Upon hydrogenation, this hypothetical contamination may have inhibited the full benefit of the HSE process. However, these samples still showed very strong improvement in emitter performance.

The quality of native oxide is important to consider, and it was not clear what the minimum SRV could have been had some other proven passivation layer been used. At the time of this work a method of accurately assessing the quality of passivation layers was not available.

There is evidence that native oxide coupled with silicon nitride can act as an excellent passivation layer, with SRV values down to 8 cm/s achieved on lightly doped silicon [5.2]. The cells in this work were exposed to ambient air for the development of native oxide. Certainly the composition of this air would be a factor in the quality of the oxide and was not a controlled aspect of these experiments. Native oxides formed from different methods, such as chemical boiling, or simple exposure to water, have been found to contain pin-holes or even islands of oxide with no, or limited oxide growth between the islands [5.3]. If this is the case with native oxides formed in air ambient at low temperatures, then it is quite likely that the lower limit of SRV due to passivation quality is not zero. Regardless, there have been plenty of material combinations which do provide very low surface recombination velocities.

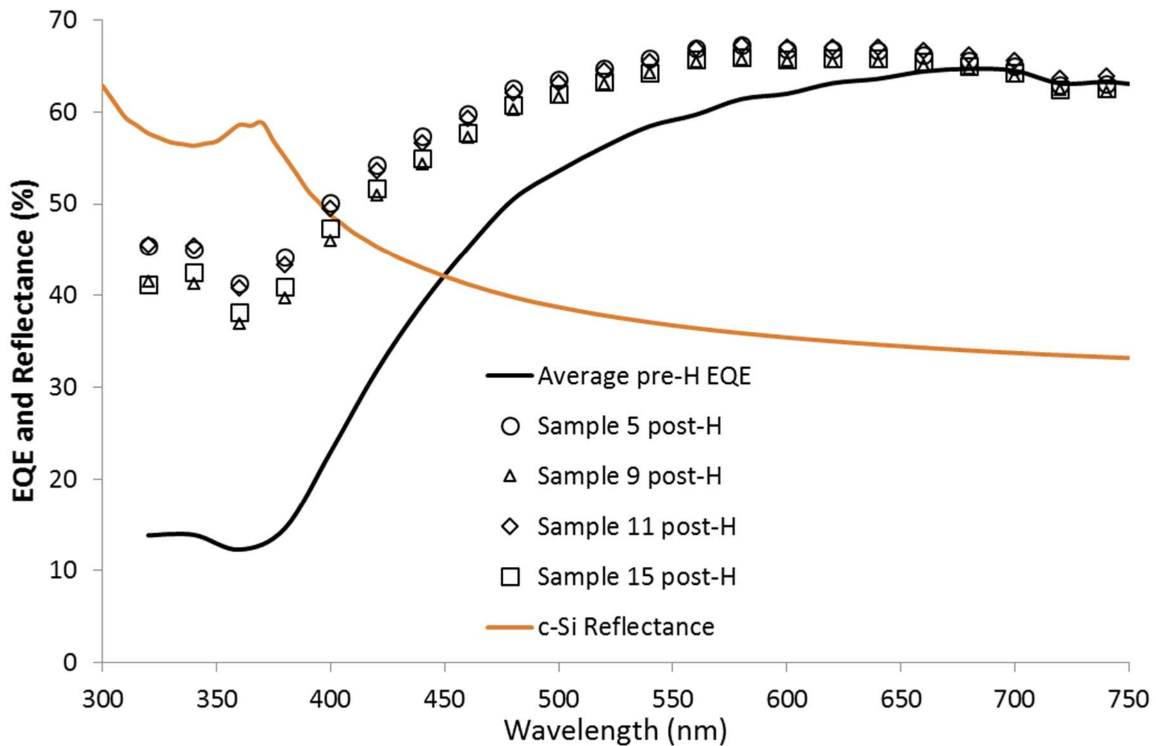

Figure 5.5 External Quantum Efficiency curves for four solar cells before and after the HSE process. Also shown is the curve for the reflectance of planar crystalline silicon to demonstrate the very high quality of these emitters after hydrogenation.

CHAPTER 6: CONCLUSIONS AND FUTURE WORK

Top-down aluminum induced crystallization (TAIC) was explored as a low-temperature method for emitter formation on n-type silicon solar cells. Although the initial solar cells formed with this technique were lower in efficiency than modeling would suggest for a comparable homojunction solar cell of the same characteristics, there are likely methods by which this drawback could be mitigated in future work for both surfaces of n-type and p-type silicon solar cells. One idea proposed was to use amorphous silicon carbide as an intrinsic layer between the crystallized layer and the silicon wafer. Preliminary results presented in chapter 2 demonstrated that minimal, if any crystallization of a-SiC:H occurred by aluminum at temperatures that were shown to fully crystallize a-Si:H. A similar scheme has been proposed with a tunneling insulating oxide layer capped with n-type polycrystalline silicon for the rear surface of high-efficiency n-type silicon solar cells [6.1]

In order for these emitters to be used on industrial solar cells with screen printed contacts, dopant gases such as diborane and phosphine would need to be used to introduce additional dopants in the amorphous silicon to decrease sheet resistance. These additional dopant gases may complicate processing if it is found that separate chambers are needed for deposition of intrinsic/insulating and doped amorphous silicon. Another issue with increasing dopant density occurs with not only increased Auger recombination, but also increased SRH recombination. With further development, this problem may be solved for the emitter by implementing the hydrogen selective emitter (HSE), which was invented during the course of this work. The HSE process is currently undergoing transition from lab-scale solar cells to full-size cells with industrially compatible processing. Once complete, the HSE process should be compatible with

TAIC emitter solar cells, providing better surface properties while introducing atomic hydrogen that is able to heal defects present at the interface of these types of solar cells.

References

[1.1] M.A. Green, "The path to 25% silicon solar cell efficiency: History of silicon cell evolution," *Progress in Photovoltaics: Research and Applications*, vol. 17, pp. 183-189, 2009.

[1.2] "Top-tier photovoltaic polysilicon and wafer producers to be profitable in 2013," *Solarbuzz Solar Market Research and Analysis*, <http://www.solarbuzz.com/news/recent-findings/top-tier-photovoltaic-polysilicon-and-wafer-producers-be-profitable-2013>

[1.3] International Technology Roadmap for Photovoltaic, SEMI, 4th Edition, 2013.

[1.4] R. Kopecek and J. Libal, "Switch from p to n," *PV-Magazine*, <http://www.pv-magazine.com/archive/articles/beitrag/switch-from-p-to-n-_100007072/86/?tx_ttnews%5BbackCat%

[1.5] D.M. Powell, M.T. Winkler, H.J. Choi, C.B. Simmons, D. Berney Needleman, and T. Buonassisi, "Crystalline silicon photovoltaics: A cost analysis framework for determining technology pathways to reach baseload electricity costs," *Energy and Environmental Science*, vol. 5, pp. 5874-5883, 2012.

[1.6] P.A. Basore, "Numerical modeling of textured silicon solar cells using PC-1D," *IEEE Transactions on Electron Devices*, vol. 37, no. 2, pp. 337-343, 1990.

[1.7] S. Fonash, "AMPS-1D: Analysis of microelectronic and photonic structures," Available Online: <http://www.ampsmodeling.org/>, 2010.

[1.8] K.R. McIntosh and P.P. Altermatt, "A freeware 1D emitter model for silicon solar cells," *35th IEEE PVSC*, pp. 2188-2193, 2010.

[2.1] H.A. Naseem, M.S. Haque, and W.D. Brown, "Method of doping silicon, metal doped silicon, method of making solar cells, and solar cells," U.S. Patent 6339013 B1, 2002.

[2.2] Semiconductor Devices, Banerjee

[2.3] B.Y. Tsaur, W. Turner, and J.C.C. Fan, "Efficient Si solar cells by low-temperature solid-phase epitaxy," *Applied Physics Letters,* vol. 39, no. 9, pp. 749-751, 1981.

[2.4] S. Ishihara, M. Kitagawa, and T. Hirao, "Low-temperature crystallization of hydrogenated amorphous silicon films in contact with evaporated aluminum electrodes," *Journal of Applied Physics*, vol. 62, no. 3, pp. 837-840, 1987.

[2.5] O. Nast, S. Brehme, D.H. Neuhaus, and S.R. Wenham, "Polycrystalline silicon thin films on glass by aluminum-induced crystallization," *IEEE Transactions on Electron Devices*, vol. 46, no. 10, pp. 2062-2068, 1999.

[2.6] O. Nast, "Grain size and structure engineering during Al-induced crystallization for Si thin-film solar cells," 28th PVSC, pp.284-287, 2000.

[2.7] D.H. Neuhaus, R. Bardos, L. Feitknecht, T. Puzzer, M.J. Keevers, and A.G. Aberle, “Minority carrier properties of single- and polycrystalline silicon films formed by aluminium-induced crystallization,” *28th IEEE PVSC*, pp. 65-68, 2000.

[2.8] S.Y. Lien, J.H. Wang, and D.S. Wuu, “Growth of polycrystalline silicon solar cell on epitaxial thickening of AIC seed layer by hot-wire CVD,” < http://www.mdu.edu.tw/~prc/download/DATA/iedms/02Growth%20of%20polycrystalline%20silicon%20solar%20cell%20on%20epitaxial%20thickening%20of%20AIC%20seed%20layer%20by.pdf>, 2002.

[2.9] S. Gall, M. Muske, I. Sieber, J. Schneider, O. Nast, and W. Fuhs, “Polycrystalline silicon on glass by aluminum-induced crystallization,” *29th IEEE PVSC*, pp. 1202-1205, 2002.

[2.10] P.I. Widenborg and A.G. Aberle, “Surface morphology of poly-Si films made by aluminium-induced crystallization on glass substrates,” *Journal of Crystal Growth*, vol. 242, pp. 270-282, 2002.

[2.11] J. Schneider, J. Klein, M. Muske, A. Schopke, S. Gall, and W. Fuhs, “Aluminium-induced crystallization of amorphous silicon: Influence of oxidation conditions,” *3rd World Conference on Photovoltaic Energy Conversion*, pp. 106-109, 2003.

[2.12] C.M. Hsu and M.C. Yu, “Deterioration of aluminum induced crystallization of sputtered silicon by film stress,” *Journal of Materials Science Letters*, vol. 22, pp. 1079-1081, 2003.

[2.13] E. Pihan, A. Slaoui, A. Focsa, and P. Roca I Cabarrocas, “Polycrystalline silicon films on ceramic substrates by aluminium-induced crystallization process,” *3rd World conference on Photovoltaic Energy Conversion*, pp. 1182-1885, 2003.

[2.14] Y. Ishikawa, A. Nakamura, Y. Uraoka, and T. Fuyuki, “Polycrystalline silicon thin film for solar cells utilizing aluminum induced crystallization method,” *Japanese Journal of Applied Physics*, vol. 43, no. 3, pp. 877-881, 2004.

[2.15] A. Straub, D. Inns, M.L. Terry, Y. Huang, P.I. Widenborg, and A.G. Aberle, “Optimisation of low-temeprature silicon epitaxy on seeded glass substrates by ion-assisted deposition,” *Journal of Crystal Growth*, vol. 280, pp. 385-400, 2005.

[2.16] J. Schneider, J. Klein, A. Sarikov, M. Muske, S. Gall, and W. Fuhs, “Suppression of nucleation during the aluminum-induced layer exchange process,” *MRS Proceedings,* vol. 862, 2005.

[2.17] Y. Civale, L.K. Nanver, P. Hadley, E.J.G. Goudena, H.W. van Zeijl, and H. Schellevis, “Low-temperature solid-phase epitaxy of defect-free aluminum p+-doped silicon for nanoscale device application,” *MRS Proceedings,* vol. 940, 2006.

[2.18] A.G. Aberle, “Progress with polycrystalline silicon thin-film solar cells on glass at UNSW,” *Journal of Crystal Growth*, vol. 287, pp. 386-390, 2006.

[2.19] I. Gordon, L. Carnel, D. van Gestel, G. Beaucarne, and J. Poortmans, “8% Efficient thin-film polycrystalline-silicon solar cells based on aluminum-induced crystallization and thermal CVD,” *Progress in Photovoltaics: Research and Applications*, vol. 15, pp. 575-586, 2007.

[2.20] D. van Gestel, M.J. Romero, I. Gordon, L. Carnel, J.D'Haen, G. Beaucarne, M. Al-Jassim, and J. Poortmans," *Applied Physics Letters*, vol. 90, pp. 092103-1-092103-4, 2007.

[2.21] E. Pihan, A. Slaoui, and C. Maurice, "Growth kinetics and crystallographic properties of polysilicon thin films formed by aluminium-induced crystallization," *Journal of Crystal Growth*, vol. 305, pp. 89-98, 2007.

[2.22] P.I. Widenborg and A.G. Aberle, "Polycrystalline silicon thin-film solar cells on AIT-textured glass superstrates, *Advances in Optoelectronics*, vol. 2007, pp. 1-7, 2007.

[2.23] G. Beaucarne, "Silicon thin-film solar cells," *Advances in Optoelectronics,* vol. 2007, pp. 1-12, 2007.

[2.24] C. Jaeger, T. Antesberger, and M. Stutzmann, "Hydrogen passivation of ultra-thin low-temperature polycrystalline silicon films for electronic applications," *Journal of Non-Crystalline Solids,* vol. 354, pp. 2314-2318, 2008.

[2.25] W. Luangtip, S. Rotbuathong, P. Chindaudom, M. Horphatum, V. Patthanasetthakul, P. Eiamchai, and T. Srikirin, "Investigation of aluminium diffusion into amorphous silicon thin film at high temperature by in-situ spectroscopic ellipsometry," *Advanced Materials Research*, vols. 55-57, pp. 449-452, 2008.

[2.26] I. Gordon, D. van Gestel, Y. Qiu, S. Venkatachalam, G. Beaucarne, and J. Poortmans, "Processing and characterization of efficient thin-film polycrystalline silicon solar cells," *MRS Proceedings*, vol. 1101, 2008.

[2.27] R. Song, Y. Liu, and Z. Cao, "Effect of aluminum supply on aluminum-induced crystallization of amorphous silicon at low temperature," *Physica Status Solidi,* vol. 6, no. 3, pp. 663-669, 2009.

[2.28] D. van Gestel, I. Gordon, H. Bender, D. Saurrel, J. Vanacken, G. Beaucarne, and J. Poortmans, "Intragrain defects in polycrystalline silicon layers grown by aluminum-induced crystallization and epitaxy for thin-film solar cells," *Journal of Applied Physics*, vol. 105, pp. 114507-1-114507-12, 2009.

[2.29] S. Gall, "Polycrystalline silicon thin-films formed by the aluminum-induced layer exchange (ALILE) process," *Advances in materials research*, vol. 14, pp. 193-218, 2009.

[2.30] Z. Tang, H. Shen, H. Huang, L. Lu, Y. Yin, H. Cai, and J. Shen, "Preparation of high quality polycrystalline silicon thin films by aluminum-induced crystallization," *Thin Solid Films*, vol. 517, pp. 5611-5615, 2009.

[2.31] W. Chenglong, F. Duowang, W. Chengbin, G. Zhongrong, M.A. Hailin, and M. Shufan, "Poly-si films with low aluminum dopant containing by aluminum-induced crystallization," *Science China: Physics, Mechanics & Astronomy*, vol. 53, no. 1, pp. 111-115, 2010.

[2.32] D. van Gestel, M. Chahal, P.C. van der Wilt, I. Gordon, J.S. Im, and J. Poortmans, "Thin-film polycrystalline silicon solar cells with low intragrain defect density made via laser crystallization and epitaxial growth," *38th IEEE PVSC*, pp. 279-282, 2010.

[2.33] C. Jaeger, T. Matsui, M. Takeuchi, M. Karasawa, M. Kondo, and M. Stutzmann, "Thin film solar cells prepared on low thermal budget polycrystalline silicon seed layers," *Japanese Journal of Applied Physics*, vol. 49, pp. 112301-1-112301-4, 2010.

[2.34] C. Jaeger, M. Bator, S. Matich, and M. Stutzmann, "Two-step crystallization during the reverse aluminum-induced layer exchange process," *Journal of Applied Physics*, vol. 108, pp. 113513-1-113513-8, 2010.

[2.35] B. Birajdar, T. Antesberger, M. Stutzmann, and E. Spiecker, "Epitaxial upward transport of Al at the beginning of the Al-induced layer exchange process," *Physica Status Solidi*, vol. 5, no. 5-6, pp. 172-174, 2011.

[2.36] B. Birajdar, T. Antesberger, B. Butz, M. Stutzmann, and E. Spiecker, "Direct in situ transmission electron microscopy observation of Al push up during early stages of al-induced layer exchange," *Scripta Materialia*, vol. 66, pp. 550-553, 2012.

[2.37] M.A. Albarghouti, "Large grain poly-Si thin films by metal-induced crystallization of a-Si:H," Dissertation, University of Arkansas-Fayetteville, 2004.

[2.38] M. Hossain, "The effects of hydrogen on aluminum induced crystallization of sputtered amorphous silicon," Dissertation, University of Arkansas-Fayetteville, 2004.

[2.39] C. Jaeger, "Polycrystalline silicon thin films for electronic applications," Dissertation, Technische Universitat Munchen, Walter Schottky Institut, 2012.

[2.40] H. Jeong and S. Boo, "Structural and electrical properties of polysilicon films prepared by AIC process for a polycrystalline silicon solar cell seed layer," *International Journal of Photoenergy*, vol. 2012, 2012.

[2.41] N. Hernandez-Como and A. Morales-Acevedo, "Simulation of hetero-junction silicon solar cells with AMPS-1D," *Solar Energy Materials & Solar Cells*, vol. 94, pp. 62-67, 2010.

[2.42] M.W.M. van Cleef, J.K. Rath, F.A. Rubinelli, C.H.M. van der Werf, R.E.I. Schropp, and W.F. van der Weg, "Performance of heterojunction p^+ microcrystalline silicon n crystalline silicon solar cells," *Journal of Applied Physics*, vol. 82, no. 12, 6089-6095, 1997.

[2.43] N.G. Tarr, "A polysilicon emitter solar cell," *IEEE Electron Device Letters* **EDL-6**, no. 12, 1985, pp. 655-658.

[2.44] G. Papadopoulos, L.P. Boivin, and N.G. Tarr, "Development and characterization of polysilicon emitter solar cells," *Canadian Journal of Physics* **69**, 1991, pp. 479-482.

[2.45] A. Zouari, A. Trabelsi, and A. Ben Arab, "Simple analytical solution and efficiency improvement of polysilicon emitter solar cells," *Solar Energy Materials and Solar Cells* **92**, 2008, pp. 313-322.

[2.46] H.A. El-Jammal, "Fabrication of solar cells using low temperature aluminum assisted crystallization of amorphous silicon," M.S. Thesis, University of Arkansas, 1999.

[2.47] M. Hossain, H. Abu-safe, H. Naseem, and W. Brown, “Fabricating polycrystalline silicon solar cells using aluminum induced crystallization technique,” *International PVSEC-14* **1**, 2004, pp. 219-220.

[2.48] S.D. Shumate, M.K. Hafeezuddin, D.A. Hutchings, and H.A. Naseem, “Microstructural influence of hydrogenated amorphous silicon on polycrystalline emitter solar cells prepared by top-down aluminum induced crystallization,” *IEEE 37th PVSC*, 2011.

[2.49] C.M. Anderson, “Enhanced crystallization of amorphous silicon thin films using embedded silicon nanocrystals,” *University of Minnesota*, Dissertation, 2008.

[2.50] C. Smit, R.A.C.M.M. van Swaaij, H. Donker, A.M.H.N. Petit, W.M.M. Kessels, “Determining the material structure of microcrystalline silicon from Raman spectra,” *Journal of Applied Physics*, vol. 94, pp. 3582-3588, 2003.

[2.51] K. Zellama, L. Chahed, P. Sladek, M.S. Theye, J.H. von Bardbeleben, P. Roca i Cabarrocas, “Hydrogen effusion-induced structural changes and defects in a-Si:H films: Dependence upon the film microstructure,” *Physical Review B*, vol. 53, no. 7, 1996, pp. 3804-3812.

[2.52] M. Hossain, H.H. Abu-safe, H. Naseem, and W.D. Brown, “The effects of hydrogen on aluminum-induced crystallization of sputtered hydrogenated amorphous silicon,” *Journal of Electronic Materials*, vol. 35, no. 1, 2006, pp. 113-117.

[2.53] I. Martin, M. Vetter, A. Orpella, J. Puigdollers, A. Cuevas, and R. Alcubilla, “Surface passivation of p-type crystalline Si by plasma enhanced chemical vapor deposited amorphous SiCx:H films,” *Applied Physics Letters*, vol. 79, no. 14, pp. 2199-2201, 2001.

[2.54] M. Hossain, M. Yun, V. Korampally, and S. Gangopadhyay, “Low temperature crystallization of amorphous silicon carbide thin films for p-n junction devices fabrication,” *Journal of Materials Science: Materials in Electronics*, vol. 19, pp. 801-804, 2008.

[2.55] M. Hossain, J. Roberto Sanchez Perez, J. Marcel Rodriguez Rivera, K. Gangopadhyay, and S. Gangopadhyay, “Novel process for low temperature crystallization of a-SiC:H for optoelectronic applications,” *Journal of Materials Science: Materials in Electronics*, vol. 20, pp. S412-S415, 2009.

[2.56] M.G. Deceglie and H.A. Atwater, “Effect of defect-rich epitaxy on crystalline silicon amorphous silicon heterojunction solar cells and the use of low-mobility layers to improve performance,” *37th IEEE Photovoltaics Specialists Conference*, pp. 001417-001420, 2011.

[3.1] D.L. young, J.V. Li, C.W. Teplin, P. Stradins, and H.M. Branz, “Junction transport in epitaxial film silicon heterojunction solar cells,” *37th IEEE Photovoltaic Specialists Conference (PVSC)*, 2011.

[3.2] P.A. Basore, “CSG-2: Expanding the production of a new polycrystalline silicon PV technology,” Available Online: < http://www.csgsolar.com/downloads/CSG-2%20Basore.pdf>, 2006.

[3.3] I. Gordon, L. Carnel, D. Van Gestel, G. Beaucarne, and J. Poortmans, "8% Efficient Thin-Film Polycrystalline-Silicon Solar Cells Based on Aluminum-Induced Crystallization and Thermal CVD," *Progress in Photovoltaics: Research and Applications*, 15, 2007, pp. 575-586.

[3.4] D. Van Gestel, M.J. Romero, I. Gordon, L. Carnel, J. D'Haen, G. Beaucarne, M. Al-Jassim, and J. Poortmans, "Electrical Activity of Intragrain Defects in Polycrystalline Silicon Layers Obtained by Aluminum-Induced Crystallization and Epitaxy," *Applied Physics Letters*, 90, 2007, pp. 092103-1-3.

[3.5] C. Jaeger, T. Matsui, M. Takeuchi, M. Karasawa, M. Kondo, and M. Stutzmann, "Thin Film Solar Cells Prepared on Low Thermal Budget Polycrystalline Silicon Seed Layers," *Japanese Journal of Applied Physics*, 49, 2010, pp. 112301-1-4.

[3.6] K. Alberi, I.T. Martin, M. Shub, C.W. Teplin, M.J. Romero, R.C. Reedy, E. Iwaniczko, A. Duda, P. Stradins, H.M. Branz, and D.L. Young, "Material quality requirements for efficient epitaxial film silicon solar cells," *Applied Physics Letters*, 96, 2010, pp. 073502-1-3.

[3.7] D.C. Bobela, C.W. Teplin, D.L. Young, I.T. Martin, H.M. Branz, and P. Stradins, "Epitaxial Crystal Silicon Absorber Layers and Solar Cells Grown at 1.8 Microns per Minute," *Thirty-Seventh IEEE PVSC*, 2011.

[3.8] D.L. Young, K. Alberi, C. Teplin, I. Martin, P. Stradins, M. Shub, C. Beall, E. Iwaniczko, H. Guthrey, M.J. Romero, T.K. Chuang, E. Mozdy, and H.M. Branz, "Toward film-silicon solar cells on display glass," *Thirty-Fifth IEEE Photovoltaics Specialists Conference (PVSC)*, pp. 626-630, 2010.

[3.9] G. Beaucarne and A. Slaoui, "Thin film polycrystalline silicon solar cells," Thin Film Solar Cells, Eds. J. Poortmans and V. Arkhipov, *John Wiley & Sons, Ltd*, pp. 97-131, 2006.

[3.10] S.D. Shumate, H.K. Mohammed, D.A. Hutchings, and H.A. Naseem, "Large-grain polysilicon seed layers on glass for epitaxial silicon solar cells," *Thirty-Eighth IEEE Photovoltaics Specialists Conference*, 2012.

[4.1] T.C. Roder, S.J. Eisele, P. Grabitz, C. Wagner, G. Kulushich, J.R. Kohler, and J.H. Werner, "Add-On Laser Tailored Selective Emitter Solar cells," *Progress in Photovoltaics: Research and Applications*, 18, 2010, pp. 505-510.

[4.2] D.S. Ruby, P. Yang, M. Roy, and S. Narayanan, "Recent Progress on the Self-Aligned, Selective-Emitter Silicon Solar Cell," *Twenty-Sixth IEEE PVSC*, 1997.

[4.3] D. Rudoph, K. Peter, A. Meijer, O. Doll, and I. Kohler, "Etch Back Selective Emitter Process with Single $POCL_3$ Diffusion," *Twenty-Sixth European Photovoltaic Solar Energy Conference and Exhibition*, 2011.

[4.4] R. Low, A. Gupta, H.J. Gossmann, J. Mullin, V. Yelundur, B. Damiani, V.Chandrasekaran, D. Meier, B. McPherson, and A. Rohatgi, "High Efficiency Selective Emitter Enabled Through Patterned Ion Implantation," *Thirty-Seventh IEEE PVSC*, 2011.

[4.5] P. Altermatt, H. Plagwitz, R. Bock, J. Schmidt, R. Brendel, M.J. Kerr, and A. Cuevas, "The Surface Recombination Velocity at Boron-Doped Emitters: Comparison Between Various Passivation Techniques," *Twenty-First European Photovoltaic Solar Energy Conference*, 2006.

[4.6] P.P. Altermatt, J.O. Schumacher, A. Cuevas, M.J. Kerr, and S.W. Glunz, "Numerical modeling of highly doped Si:P emitters based on Fermi-Dirac statistics and self-consistent material parameters," *Journal of Applied Physics*, vol. 92, pp. 3187-3197, 2002.

[4.7] S.D. Shumate, D.A. Hutchings, H.Mohammed, G. Beilke, B.S. Newton, M.G. Young, H. Abu-Safe, S-Q. Yu, and H.A. Naseem, "Self-aligned hydrogenated selective emitter for n-type solar cells," *IEEE 38th PVSC*, 2012.

[4.8] L.V.C. Assali and J.R. Leite, "Microscopic mechanism of hydrogen passivation of acceptor shallow levels in silicon," *Physical Review Letters*, vol. 55, no. 9, pp. 980-982, 1985.

[4.9] C.P. Herrero, M. Stutzmann, and A. Breitschwerdt, "Boron-hydrogen complexes in crystalline silicon," *Physical Review B*, vol. 43, no. 2, pp. 1555-1575, 1991.

[4.10] L. Korpas, J.W. Corbett, and S.K. Estreicher, "Multiple trapping of hydrogen at boron and phosphorus in silicon," *Physical Review B*, vol. 46, no. 19, pp. 12365-12370, 1992.

[4.11] Y. Ohmura, Y. Otomo, Y. Tago, N. Terakado, and T. Satoh, "Enhanced hydrogenation and acceptor passivation in Si by pressurized water boiling," *Applied Physics Letters*, vol. 67, pp. 64-66, 1995.

[4.12] O. Sugiura, T. Shiraiwa, and M. Matsumura, "A novel post-hydrogenation process for chemical-vapor-deposited a-Si thin-film transistors," *Japanese Journal of Applied Physics*, vol. 32, pp. L981-L983, 1993.

[4.13] H.N. Wanka and M.B. Schubert, "High silicon etch rates by hot filament generated atomic hydrogen," *Journal of Physics D: Applied Physics*, vol. 30, pp. L28-L31, 1997.

[4.14] M. Hossain, H.H. Abu-Safe, H. Naseem, and W.D. Brown, "Characterization of hydrogenated amorphous silicon thin films prepared by magnetron sputtering," *Journal of Non-Crystalline Solids*, vol. 352, no. 1, pp. 18-23, 2006.

[4.15] A.A. Langford, M.L. Fleet, and B.P. Nelson, "Infrared absorption strength and hydrogen content of hydrogenated amorphous silicon," *Physical Review B*, vol. 45, no. 23, pp. 13367-13377, 1992.

[4.16] C.H. Ling, "On the mobility dip in polycrystalline silicon," *Journal of Physics D: Applied Physics*, vol. 16, pp. L181-184, 1983.

[4.17] J.Y.W. Seto, "The electrical properties of polycrystalline silicon films," *Journal of Applied Physics*, vol. 46, no. 12, pp. 5247-5254, 1975.

[4.18] C.H. Seager, "Grain boundaries in polycrystalline silicon," *Annual Review of Materials Science*, vol. 15, pp. 271-302, 1985.

[4.19] O. Sugiura, T. Shiraiwa, and M. Matsumura, “A novel post-hydrogenation process for chemical-vapor-deposited a-Si thin-film transistors,” *Japanese Journal of Applied Physics*, vol. 32, part 2, no. 7B, pp. L981-L983, 1993.

[4.20] “Standard practice for conversion between resistivity and dopant density for boron-doped, phosphorus-doped, and arsenic-doped silicon,” *American Society for Testing and Materials*, Available Online: <cmos.mirc.gatech.edu/internal/documents/.../ASTM-F723.pdf>, 1999.

[4.21] N.H. Nickel, G.B. Anderson, N.M. Johnson, and J. Walker, “Nucleation mechanism of hydrogen-induced platelets in single crystal and polycrystalline silicon,” *Physica B*, vol. 273-274, pp. 212-215, 1999.

[4.22] M. Stutzmann, “Hydrogen passivation of boron acceptors in silicon: Raman studies,” *Physical Review B*, vol. 35, no. 11, pp. 5921-5924, 1987.

[5.1] M.J. Kerr and A. Cuevas, “General parameterization of Auger recombination in crystalline silicon,” *Journal of Applied Physics*, vol. 91, no. 4, pp. 2473-2480, 2002.

[5.2] Z.R. Chowdhury, K. Cho, and N.P. Kherani, “High-quality surface passivation of silicon using native oxide and silicon nitride layers,” *Applied Physics Letters*, vol. 101, pp. 021601-1-4, 2012.

[5.3] T. Aoyama, T. Yamazaki, and T. Ito, “Nonuniformities of native oxides on Si(001) surfaces formed during wet chemical cleaning,” *Applied Physics Letters*, vol. 61, pp. 102-104, 1992.

[6.1] F. Feldmann, M. bivour, C. Reichel, M. Hermle, and S.W. Glunz, “Passivated rear contacts for high-efficiency n-type Si solar cells providing high interface passivation quality and excellent transport characteristics,” *Solar Energy Materials and Solar Cells*, pp. 270-274, 2014.

Appendix A: Description of Research for Popular Publication

"Climate change has begun devastating the earth in ways only scientists could have imagined," said Seth Shumate with a grim demeanor reminiscent of an ER doctor at the end of a busy shift. Seth has been working on solar cell research and development for the past 5 years in an effort to "provide the cheapest, greenest energy possible that is so cheap that even the staunchest conservatives might come around to offset their love of driving SUVs to the edge of a cliff that will plunge humanity back into the bronze age."

His latest invention, the hydrogen selective emitter (HSE), has the potential to make the cheapest, most reliable solar panels even more cost effective. A solar panel is an array of solar cells which converts sunlight into the electricity that we use to run our everyday lives. His innovation has the potential to reduce silver on the front of solar cells while increasing their efficiency.

"We introduce atomic hydrogen to the top layer of the solar cell. The atomic hydrogen, which is generated by catalytically dissociating H_2 gas, pairs with boron acceptor impurities near the surface of the solar cell, reducing surface recombination velocities and increasing the efficiency potential of the photovoltaic devices in much the same way as a traditional selective emitter, but without increasing the sheet resistance of the photovoltaic device as is the case with the incumbent technology," he said as he noticed my eyes glaze over like they were being run through a Krispy Kreme production line. "Simply put, we eliminate an age-old tradeoff so that we can use less silver while increasing the power coming out of the solar cell," he added.

The technology has been funded by the NSF through a Small Business Innovation Research grant and a Department of Energy SunShot grant to help commercialize the technology through their startup company Picasolar, Inc.

When asked about the outlook of the solar industry, Seth commented in a sing-song voice, "I think the future of the solar industry will shine bright like a diamond. The industry has grown 20x in the past 6 years, kind of like my stress level." "When you have power purchase agreements going in Texas for solar projects at rates cheaper than any other form of electricity, including coal and natural gas, then I'd say we're at a point where we have the technological capability of filling in the grave we've dug for ourselves through the use of fossil fuels…. Only time will tell," he said.

So what's next on the horizon for this technology? "Right now we're working on transitioning the HSE from the lab scale to the fab scale. That means full-sized 6" solar cells that can be processed at up to 3000 pieces per hour. We figure if we can do that, the n-type market segment of the solar industry will be ready to implement our technology. We've come a long way towards this goal, and we've got our work cut out for us", he said. "One of

the cool things I'm getting to do now is to make a chamber that can process full-sized solar cells. Here's a picture of the CAD file that the US based manufacturer has sent us," he said as he slid over a printout of an impressive looking hunk of metal, knocking over some sample boxes and grinning. I left the interview with a renewed sense of hope in humanity and hopeful about my grandchildren's prospects, but I'm still going to teach them to shoot!

-- Lester Smith, science reporter for the Northwest Arkansas End of Times

Appendix B: Executive Summary of Newly Created Intellectual Property

[1] S.D. Shumate, D.A. Hutchings, M.K. Hafeezuddin, M.G. Young, and S. Little, "Solar Cells and Methods of Fabrication Thereof," U.S. Patent Application 14178216, Submitted February 11th, 2014.

[2] D.A. Hutchings, S.D. Shumate, and H.A. Naseem, "Ultra-Large Grain Polycrystalline Semiconductors Through Top-Down Aluminum Induced Crystallization (TAIC)," U.S. Patent Application 13905966, Submitted May 30th, 2013.

[3] S.D. Shumate and D.A. Hutchings, "Solar Cells and Methods of Fabrication Thereof," U.S. Patent Application 13754863, Submitted January 30th, 2013.

[4] D.A. Hutchings, S.D. Shumate, H.A. Naseem, and K. Sharif, "Development of Top-Down Aluminum Induced Crystallization for High Efficiency Photovoltaics," U.S. Patent Application 61449050, Submitted March 3, 2011.

[5] D.A. Hutchings, S.D. Shumate, H.A. Naseem, and K. Sharif, "Method of Metal Induced Crystallization of Amorphous Silicon and Method of Doping," U.S. Patent Application 61352681, Submitted June 8th, 2010.

Appendix C: Potential Patent and Commercialization Aspects of Newly Created IP

i) Patent applications 1) and 3) from Appendix B are currently written around IP that is being pursued commercially by Picasolar, Inc. Patent applications 2), 4), and 5) from Appendix B have potential commercialization aspects, but are not actively being pursued.

ii) Patent applications 1) and 3) relate to the HSE technology and various implementations that may be possible and, as such, help enable the commercialization of this technology. Patent applications 2), 4), and 5) have the most commercial impact in wafer-based, rear surface passivated solar cells or thin-silicon films for display technologies.

iii) No prior disclosure to these documents would void them has occurred, and the major ideas that were considered necessary or ancillary to commercializing either the TAIC or HSE technologies that appear in this document were included in these patent applications and other documentation prior to publishing any data in conference proceedings, grant applications, or communications with other entities.

Appendix D: Broader Impact

The broader impact of the pursuit of photovoltaics as both a research and commercialization endeavor has provided great benefit to all of humanity. Cheap, minimally polluting technologies such as photovoltaics are the safest way for our civilization to produce electricity. The intent of the research directions pursued during the course of this Ph.D. were typically with a focus toward research that had the potential to impact the improvement of solar cells and/or provide alternative means in which to do so. Educational outreach has been a priority and many undergraduate and graduate students have benefitted educationally because of work that has been carried out over the course of the past 5 years related to this research. Jobs within the state of Arkansas have been created, and federal funding has been awarded to support this research and the people involved in it. Substantial portions of this funding has gone to support local lab facilities including AAPRC and HiDEC at the University of Arkansas.

Appendix E: Microsoft Project Printout

	Task Name	Duration	Start	Finish	Pred
1	Learn Cluster tool	34 days	19 Aug '09	05 Oct '09	
2	Repair Cluster Tool	87 days	06 Oct '09	03 Feb '10	1
3	Literature Review	99 days	19 Aug '09	04 Jan '10	
4	Reproduce large-grain polycrystalline silicon work	127 days	05 Jan '10	30 Jun '10	3
5	TAIC emitter solar cell literature review	7 days	01 Jul '10	09 Jul '10	4
6	**TAIC emitter solar cell fabrication**	**617 days**	**01 Oct '10**	**11 Feb '13**	**5**
7	Rapid Thermal Annealing Optimization	8 days	01 Oct '10	12 Oct '10	
8	SEM and TEM Analysis of TAIC Emitters	28 days	10 Nov '10	17 Dec '10	
9	**IEEE PVSC Experiments**	**15 days**	**26 Jan '11**	**15 Feb '11**	
10	Film Deposition	3 days	26 Jan '11	28 Jan '11	
11	FTIR Measurements	1 day	31 Jan '11	31 Jan '11	10
12	Cell Fabrication	5 days	01 Feb '11	07 Feb '11	11
13	Cell Measurements	1 day	08 Feb '11	08 Feb '11	12
14	Paper writeup	5 days	09 Feb '11	15 Feb '11	13
15	A-SiC:H deposition and TAIC experiments	5 days	08 Jun '11	14 Jun '11	
16	Raman spectroscopy measurements	12 days	15 Jan '13	30 Jan '13	
17	Quantum efficiency measurements	2 days	08 Feb '13	11 Feb '13	
18	**Hydrogen chamber design and build**	**36 days**	**17 Oct '11**	**05 Dec '11**	
19	Hydrogenation of TAIC emitter solar cells	16 days	17 Oct '11	07 Nov '11	
20	Hydrogen inactivation optimization experiments	10 days	22 Nov '11	05 Dec '11	
21	TAIC thin-film silicon on glass development	305 days	30 Nov '11	29 Jan '13	
22	HSE Theoretical modeling	28 days	14 Dec '11	20 Jan '12	
23	**HSE Experimental Proof of Concept**	**200 days**	**06 Aug '12**	**10 May '13**	
24	Solar cell fabrication and oxidation	134 days	06 Aug '12	07 Feb '13	
25	Solar Cell hydrogenation	43 days	16 Jan '13	15 Mar '13	
26	Solar Cell J-V and QE Measurements	40 days	21 Jan '13	15 Mar '13	
27	HSE profile changes versus time experiment	7 days	02 May '13	10 May '13	

Appendix F: Identification of All Software Used in Research and Dissertation

Computer #1:
Model Number: Dell Vostro 230
Serial Number: GF13QL1
Location: Room 2201, ENRC
Owner: Silicon Solar Solutions, LLC.
Software #1:
Name: Microsoft Office 2010
Purchased by: Silicon Solar Solutions, LLC
Software #2:
Name: EDNA
Purchased by: Freeware
Software #3:
Name: AMPS1D
Purchased by: Freeware
Software #4:
Name: PC-1D
Purchased by: Freeware

Computer #2:
Model Number: Dell XPS
Serial Number: 46JCPX1
Location: Home Computer
Owner: Seth Shumate
Software #1:
Name: Microsoft Office 2013
Purchased by: Seth Shumate

Appendix G: All Publications Published, Submitted and Planned

1) S. D. Shumate, M. K. Hafeezuddin, H. A. Naseem, D. A. Hutchings, "Microstructural Influence of Hydrogenated Amorphous Silicon on Polycrystalline Emitter Solar Cells Prepared by Top-down Aluminum Induced Crystallization," Proc. of the 2011 IEEE PVSC, Seattle, Washington, June 19-24, 2011.

2) S.D. Shumate, *et al.,* "Self-aligned hydrogenated selective emitter for n-type solar cells," IEEE 38th PVSC, 2012.

3) S.D. Shumate, *et al.*, "Large-Grain Polysilicon Seed Layers on Glass for Epitaxial Silicon Solar Cells," IEEE 38th PVSC, 2012.

4) S.D. Shumate, *et al.,* "Progress on the Hydrogen Selective Emitter for N-type Solar Cells," IEEE 39th PVSC, 2013.

5) S.D. Shumate, *et al.,* "Top-down Aluminum Induced Crystallization for N-type Solar Cell Emitters," IEEE 39th PVSC, 2013.